Title

Modeling and Control of State of Charge of Modular and Second Life Battery Systems

Permalink

https://escholarship.org/uc/item/26m1n53n

Author

Jiang, Yunfeng

Publication Date

2019

Peer reviewed|Thesis/dissertation

UNIVERSITY OF CALIFORNIA SAN DIEGO

Modeling and Control of State of Charge of Modular and Second Life Battery Systems

A dissertation submitted in partial satisfaction of the
requirements for the degree of Doctor of Philosophy

in

Engineering Sciences (Mechanical Engineering)

by

Yunfeng Jiang

Committee in charge:

Professor Raymond A. de Callafon, Chair
Professor Renkun Chen
Professor Mauricio de Oliveira
Professor Jan P. Kleissl
Professor Truong Q. Nguyen

2019

The Dissertation of Yunfeng Jiang is approved and is acceptable in quality and form for publication on microfilm and electronically:

Chair

University of California San Diego

2019

DEDICATION

To my family and friends.
Keep calm, move on.

EPIGRAPH

Every great dream begins with a dreamer. Always remember, you have within you the strength, the patience, and the passion to reach for the stars to change the world.

—Harriet Tubman

TABLE OF CONTENTS

LIST OF FIGURES

LIST OF TABLES

ACKNOWLEDGEMENTS

I would like to express my deepest appreciation and most sincere gratitude to my advisor Professor Raymond A. de Callafon for his continuous support, encouragement, suggestions, patience and opportunities provided throughout the past few years. Without his offering an olive branch, I would have been completely lost in the darkness when I was looking for new advisor. Without his insightful and knowledgeable, as well as his patience and support on me, I couldn't have such opportunity to continue research study and complete the thesis.

I also would like to express my sincere appreciation to my doctoral dissertation committee members Professor Jan P. Kleissl, Professor Mauricio de Oliveira, Professor Truong Q. Nguyen and Professor Renkun Chen.

Also, I have special thanks to Mr. Louis J. Shrinkle, who provided great support and mentoring on designing the hardware solutions of electric vehicle project.

I was fortunate enough to have internship opportunities, which definitely widen my horizon and extend my business determination. I would like to appreciate the help and chance working with Mr. Juan Belon from Belon Technologies, Mr. Qifeng Chen and Mrs. Kaiwen Zhang from Contemporary Amperex Technology Ltd. CATL for their patiently mentoring and sincerely support during my internships.

It is also my great fortune to work with labmates at UC San Diego, Dr. Xin Zhao, Dr. Bing Xia, Mr. Amir Valibeygi, Dr. Abdulelah Habib, Mr. Sai Akhil R Konakalla and Mr. Yangsheng Hu, who enlighten me with their talent, insight and dedication on both work and campus life.

Last, but certainly not the least, I would like to express my sincere appreciation to my family, who unconditionally provide both financial and spiritual support. Without their trust and patience, I can not have opportunity to experience my study, work and life.

Keep calm, and move on!

In this dissertation, Chapter 2, in full, is a reprint of the material as it appears in the following publications. The dissertation/thesis author was the primary investigator and author of these papers.

Yunfeng Jiang, Bing Xia, Xin Zhao, Truong Nguyen, Chris Mi, Raymond A. de Callafon, "Data-based fractional differential models for non-linear dynamic modeling of a Lithium-ion battery", *Energy*, vol. 135, pp. 171-181, 2017.

Yunfeng Jiang, Bing Xia, Xin Zhao, Truong Nguyen, Chris Mi, Raymond A. de Callafon, "Identification of fractional differential models for lithium-ion polymer battery dynamics", *in the 20th World Congress of the International Federation of Automatic Control (IFAC)*, Toulouse, France, July 9-14, 2017.

Chapter 3, in part, has been submitted for publication of the material as it may appear in following published journal. The dissertation/thesis author was the primary investigator and author of this paper.

Yunfeng Jiang, Xin Zhao, Amir Valibeygi and Raymond A. de Callafon, "Dynamic prediction of power storage and delivery by data-based fractional differential models of a lithium iron phosphate battery", *Energies*, vol.9 (8), pp. 590, 2016.

Chapter 4, in part is currently submitted under review or published in the following papers. The dissertation/thesis author was the primary investigator and author of these material.

Yunfeng Jiang, Louis, J. Shrinkle, Raymond A. de Callafon, "Autonomous demand-side current scheduling of parallel buck regulated battery modules", *Energy* (submitted).

Yunfeng Jiang, Abdulelah H. Habib, Xin Zhao, Louis J. Shrinkle, Raymond A. de Callafon, "Centralized recursive optimal scheduling of parallel buck regulated battery modules", *in the 56th IEEE Conference on Decision and Control (CDC)*, Melbourne, Australia, December 12-15, 2017.

VITA

2013	B.S. in Applied Physics, Dalian University of Technology
2014	M.S. in Material Science and Engineering, University of California, San Diego
2019	Ph.D. in Engineering Sciences (Mechanical Engineering), University of California, San Diego

PUBLICATIONS

- **Yunfeng Jiang**, Louis, J. Shrinkle, Raymond A. de Callafon, “Autonomous demand-side current scheduling of parallel buck regulated battery modules”, *Energy* (submitted).

- Yangsheng Hu, **Yunfeng Jiang**, Raymond A. de Callafon, “Two stage covariance based realization algorithm for closed-loop Multivariable system identification”, *Automatica* (submitted).

- Dylan Lu, Haoliang Qian, Kangwei Wang, Hao Shen, Feifei Wei, **Yunfeng Jiang**, Eric E. Fullerton, Paul K. K. Yu, Zhaowei Liu, “Nanostructring multilayer hyperbolic metamaterials for ultrafast and bright green InGaN quantum wells”, *Advanced Materials*, vol. 30 (15), pp. 1706411, 2018.

- **Yunfeng Jiang**, Abdulelah H. Habib, Xin Zhao, Louis J. Shrinkle, Raymond A. de Callafon, “Centralized recursive optimal scheduling of parallel buck regulated battery modules”, *in the 56th IEEE Conference on Decision and Control (CDC)*, Melbourne, Australia, December 12-15, 2017.

- **Yunfeng Jiang**, Bing Xia, Xin Zhao, Truong Nguyen, Chris Mi, Raymond A. de Callafon, “Data-based fractional differential models for non-linear dynamic modeling of a Lithium-ion battery”, *Energy*, vol. 135, pp. 171-181, 2017.

- **Yunfeng Jiang**, Bing Xia, Xin Zhao, Truong Nguyen, Chris Mi, Raymond A. de Callafon, “Identification of fractional differential models for lithium-ion polymer battery dynamics”, *in the 20th World Congress of the International Federation of Automatic Control (IFAC)*, Toulouse, France, July 9-14, 2017.

- **Yunfeng Jiang**, Xin Zhao, Amir Valibeygi and Raymond A. de Callafon, “Dynamic prediction of power storage and delivery by data-based fractional differential models of a lithium iron phosphate battery”, *Energies*, vol.9 (8), pp. 590, 2016.

- Wenlin Li, Fengyang Zhang, **Yunfeng Jiang**, Chong Li, Heshan Song, “Flexible and experimentally feasible shortcut to quantum Zeno dynamic passage”, *Physics Letters A*, vol. 380 (43), pp. 3595-3600, 2016.

- Wenlin Li, **Yunfeng Jiang**, Chong Li, Heshan Song, “Parity-time-symmetry enhanced optomechanically-induced-transparency”, *Scientific Reports*, vol. 6, pp. 31095, 2016.
- **Yunfeng Jiang**, Rensheng Shen, Xiangping Li, Jinsu Zhang, Hua Zhong, Yue Tian, Jiashi Sun, Lihong Cheng, Haiyang Zhong, Baojiu Chen, “Concentration effects on the upconversion luminescence in Ho/Yb co-doped $NaGdTiO_4$ phosphor”, *Ceramics International*, vol. 38 (6), pp. 5045-5051, 2012.

ABSTRACT OF THE DISSERTATION

Modeling and Control of State of Charge of Modular and Second Life Battery Systems

by

Yunfeng Jiang

Doctor of Philosophy in Engineering Sciences (Mechanical Engineering)

University of California San Diego, 2019

Professor Raymond A. de Callafon, Chair

Lithium-ion battery energy storage systems are currently being used to power an ever-increasing set of electrical applications in mobile computing and automotive industry. Lithium-ion batteries are also used to tackle the problem of energy storage to help reduce the inherent variability of renewable energy. Energy storage or charge capability is an important factor in these applications and typically expressed in the units Watt hour (Wk) or Ampere hour (Ah) respectively.

If a battery is used to plan for long term energy storage, a single large capacity battery becomes cost prohibitive and a maintenance challenge. The standard solution is a breakdown of a large battery in smaller parallel placed modules and brings an important challenge: modules

must operate and behave electrically the same to avoid a battery system unbalance in which uncontrollable stray currents between modules may occur. Typically, this challenge is solved by assuming all modules have the same capacity, electrical parameters and maintain the same state of charge. This is clearly an unrealistic assumption in case of battery module heterogeneity in which modules behave dynamically different, degrade separately over time or modules with different capacity and state of charge are mixed.

In this dissertation, the problem of combining parallel placed battery modules with possible different capacity, varying internal electric parameters and dissimilar state of charge is investigated. A solution is proposed that involves monitoring and estimation of state of charge and electrical parameters, along with scheduling of modular battery current using buck regulated battery modules. In particular, the thesis contains the following contributions in more detail.

Firstly, state-of-the-art modeling and control approaches for (modular) battery energy storage system are proposed and validated experimentally. For the state-of-the art modeling approach, a fractional differential model method is proposed to model the dynamics of a lithium-ion battery system over a large operating range. The modeling approach is a combination of conventional equivalent circuit model and electrochemical impedance spectroscopy experimental data. Furthermore, continuous-time system identification methods are employed to monitor and estimate model parameters of the proposed fractional differential model of the battery.

Secondly, to better utilize a battery energy storage system, the fractional differential battery modeling approach is proposed to characterize power delivery dynamics, given charge and discharge demand as an input. This approach is applicable not only in normal operating range, but also in extreme cases, such as battery over-charging and over-discharging as validated by experimental results included in the thesis

Finally, current scheduling strategies are proposed to solve the problem of battery module heterogeneity and further improve the performance, lifespan and safety of a complete battery energy storage system with parallel connected battery modules. The scheduling algorithms are formulated in both open-loop and closed-loop implementation. The open-loop algorithm

is formulated by solving a typical linear programming problem with detailed knowledge of the battery system. The closed-loop method is computed autonomously by recursive control algorithm without detailed battery knowledge, even when the characteristic parameters change as the battery pack ages. The experimental results indicate the feasibility and flexibility of the proposed current scheduling method in a battery pack system with parallel placed buck regulated battery modules.

Chapter 1

Introduction

1.1 Battery Energy Storage System (BESS)

International communities and governments have considerably increased investments in renewable energy technologies to reduce environmental pollution, improve energy security and economic benefits, and overcome the global energy crisis [4, 5]. Rechargeable batteries have currently been developed to power an ever-increasing diverse range of electrical applications in automobile starters, portable consumer devices, light vehicles, uninterruptible power supplies, and battery storage power stations [6]. State-of-the-art lithium-ion batteries (LIBs) are considered as one of the most popular types of rechargeable batteries, exhibiting significant improvements in energy density, offering weight, size and design flexibility, appearing a very slow loss-of-charge when not in use and exhibiting negligible memory effect [7]. Beyond all these dominant features, low investment and maintenance costs drive LIB technologies available to grow as the predominant technology for next promising generation battery energy storage system (BESS) in renewable energy industry and automotive industry [8].

In the current renewable energy industry, due to the volatility and irregularity of renewable energy production, BESS have proven the capability to regularize power flow [9, 10] and make renewable energy sources economically viable solutions for grid support [11]. A specific example of typical BESS applied in renewable energy industry is shown in Figure 1.1, where the diagram includes energy generation via power station, solar power and wind power, energy storage through BESS and energy consumption by home and factory. The battery pack of a BESS is built up from multiple LIB cells where series connections are used to provide the BESS terminal voltage and parallel connections are applied to increase storage capacity and maximize the BESS power output. For example, a LIB-based BESS can be also based on a second-life battery system recycled from electric vehicles (EVs) to provide grid supporting functions, such as demand charge management, renewable energy integration and regulation energy management [12, 13].

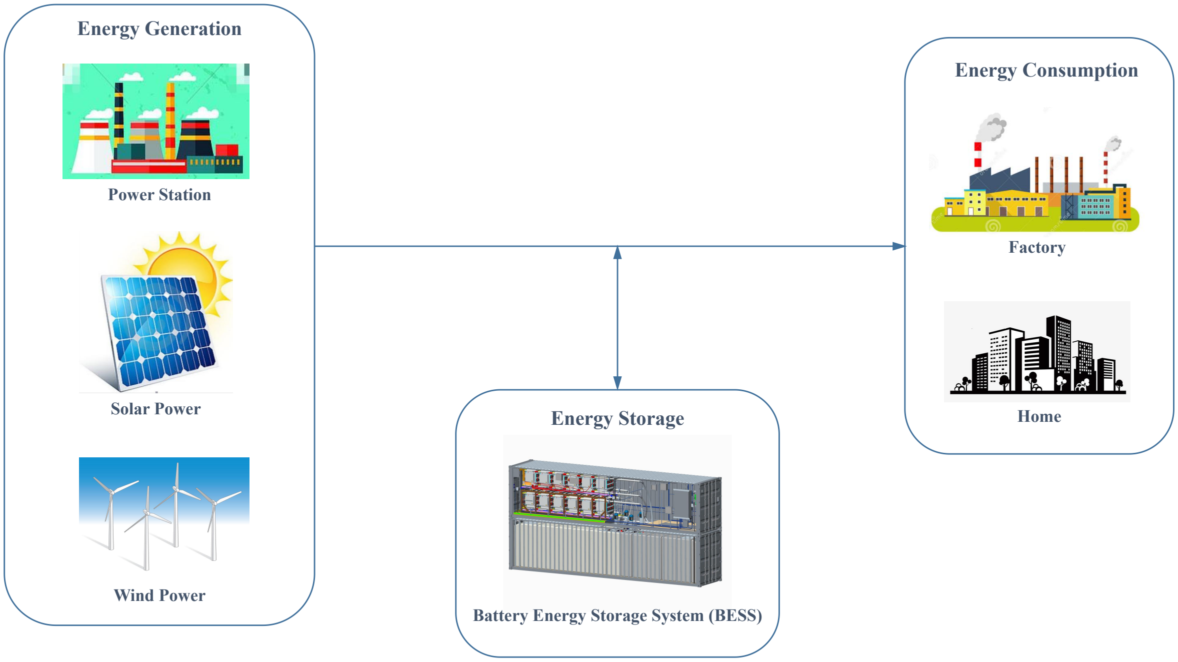

Figure 1.1. Overall architecture of a specific example of BESS in renewable energy industry, including energy generation via power station, solar power and wind power, energy storage through BESS and energy consumption by home and factory.

In the automotive industry, LIB BESS are considered as the primary energy source to become a common replacement for existing lead-acid and nickel-metal hydride batteries (NiMH) that have been widely applied in EVs, hybrid electric vehicles (HEVs), and plug-in hybrid electric vehicle (PHEVs) to significantly reduce environmental damage in the transportation sectors [14]. Unfortunately, this replacement is still a challenging task, since overheating or overcharging does cause undesirable and irreversible damage to the battery. The irreversible damages manifest itself as a degraded cell storage capacity and reduces the useful lifetime of the battery [15].

1.2 Motivating Problems

In order to protect the BESS, a battery management system (BMS) is used to continuously track battery cell and battery pack by monitoring the state of the battery, protecting the BESS from operating outside a safe operating area and maintaining safe, reliable and optimal operation [16, 17]. A specific example of BMS applied in EV is shown in Figure 1.2, where voltage (V), current (I) and temperature (T) are measured to allow for state of charge (SOC) and state of health (SOH) estimation, further perform battery balancing and compute power limits.

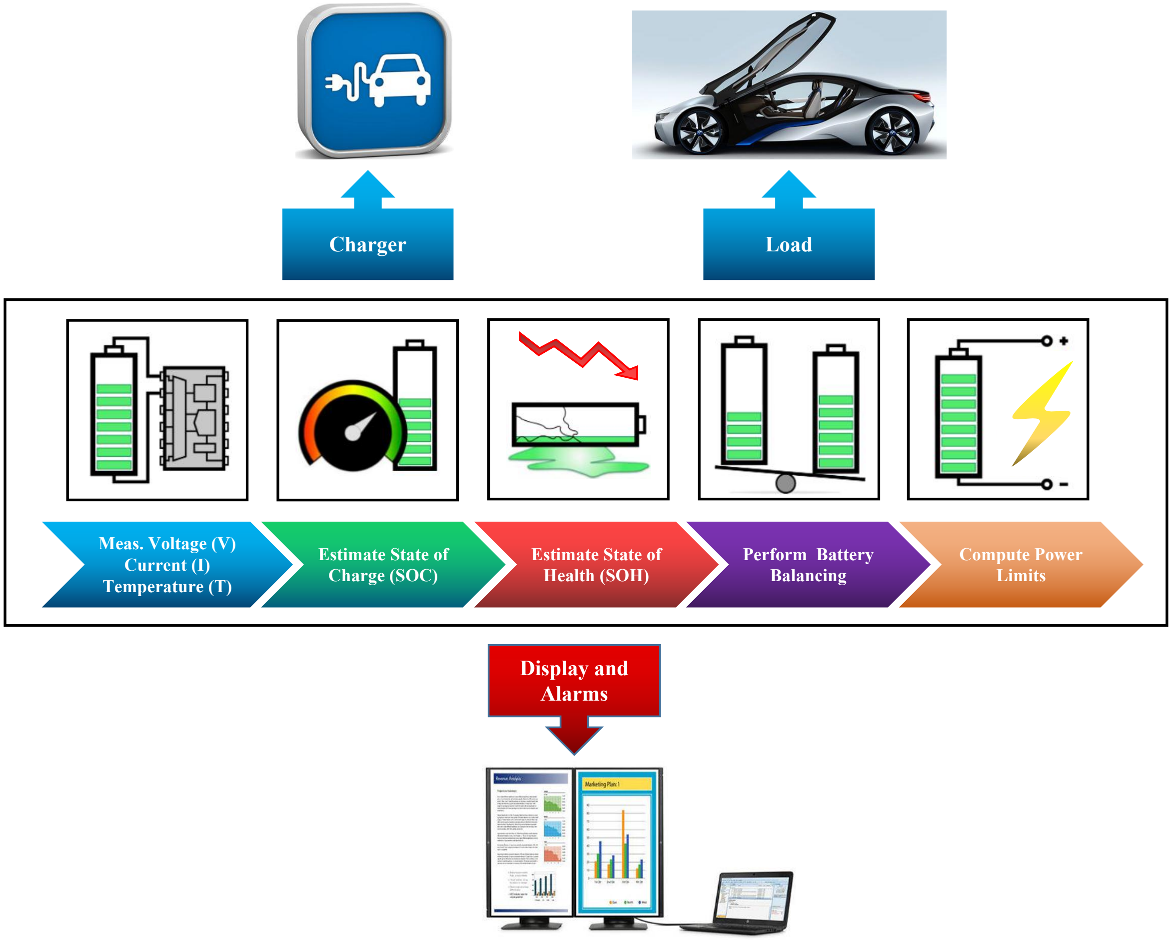

Figure 1.2. Overall architecture of a specific example of BMS in EV application.

Among all above mentioned functionalities of the BMS, the primary task of all BMS features is to use software to execute algorithms that accurately capture the battery dynamics, and continuously estimate non-measurable states, such as: SOC, SOH and state of power (SOP) of the battery. The most typical measurement that characterizes the dynamics of a BESS is the electrochemical impedance spectroscopy (EIS) technique. The EIS uses data obtained by excitation with a small voltage and experimentally measures the impedance of the system as a function of frequency. The frequency response of the measured system obtained by EIS measured data is revealed to express energy storage, battery internal states, and dissipation properties in a Nyquist plot. As an illustration in Figure 1.3, there are two main sections in the typical Nyquist plot of a LIB over full operating frequency range: (1) a low frequency range (1 mHz-1 Hz) where a straight line characterized by the 45° is usually believed to be caused by limitations in mass diffusion of lithium ions; (2) a middle frequency range (1 Hz- 10 kHz), where a semi-ellipse can be attributed to the charge transfer process, porosity of the electrodes, and double-layer effect to represent the kinetics of the electrochemical battery reactions [18]. The most simple 1-resistor-capacitor (1-RC) network equivalent circuit model (ECM) shows an ideal semi-circle in the EIS graph, which is not consistent with measured experimental data displayed in Figure 1.3. Although increasing the model order by adding more RC components may be used to improve the data fit, it suffers from a large number of model parameters to be estimated. Therefore, it is necessary to figure out a simple model with low computational requirements to accurately capture the non-linear behavior over the full operating range of typical Li-ion battery Nyquist plot, motivated by structure mismatch and complicated parameter estimation of integer ECMs.

Besides focusing on the dynamics of the electrochemical process of LIB, it is also very important to model the dynamics of battery energy storage capacity in terms of energy demand based on measurable input/output signals in real-time. In this dissertation, the modeling approach aims at characterizing the power storage and delivery capability of a BESS and also explicitly understanding the remaining energy available in the battery system from a relatively novel control perspective, which is significantly different from conventional modeling approaches.

As shown in Figure 1.1, a BESS is built from multiple parallel placed battery modules

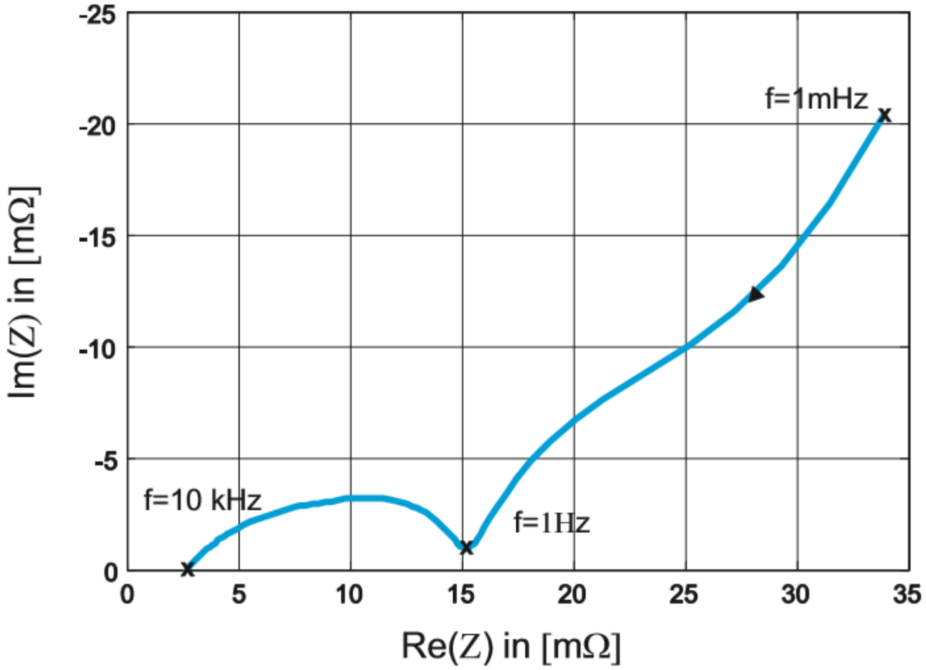

Figure 1.3. Typical Nyquist plot of a Li-ion battery cell [1].

to increase energy storage and delivery capacity. Such configuration has the advantage of significantly improving efficiency and flexibility of the battery system for EV applications and renewable energy grid support functions, since partly empty or failing battery modules in the battery pack can be swapped for fast updates in the overall SOC. As a matter of fact, variability in battery LIB parameters are inevitable in the production process and these variations in actual capacities, leakage currents, and operating conditions further enhance the heterogeneity and nonuniformity of parallel placed battery modules [19, 20]. This situation may severely cause discrepancies in internal impedance and OCV between modules and negatively affecting the performance and lifespan of a battery pack. The discrepancy between battery modules also limits the ability to extract or store the full electrical energy capacity in the battery pack [21, 22]. This motivates the development of a control and scheduling algorithm to mitigate heterogeneous effect in order to maximize the battery pack life cycle, and simultaneously monitor the state of battery for optimal performance of a high power BESS with parallel placed battery modules

[23, 24, 25].

1.3 Summary of Contributions

In the dissertation, the research aims to apply system identification methods, optimal control techniques, and optimization algorithms to significantly improve safety and performance of BESS in the electrified vehicles and electric grids. Some novel modeling approaches and control strategies are specifically proposed for battery modeling, power prediction, and current scheduling with experimental verification and validation, respectively. The summary of the main contributions is described as follows.

- **Battery State of Charge Modeling:** A battery model with non-integer order derivatives is proposed for modeling the non-linear dynamical behavior of a LIB over a large operating range, which is an amalgamation of EIS experimental data and standard 1-RC ECM. Several continuous-time (CT) system identification methods, including the standard least squares-based state-variable filter (LSSVF) and extended instrumental variable state-variable filter (IVSVF) are described and applied to estimate the model parameters and fractional derivative coefficients of the proposed model. These methods are demonstrated on experimental data from a real LIB application over broad operating range, where the storage resolution is limited and system dynamics is stiff.
- **Battery Power Prediction:** A fractional derivative modeling approach is proposed aiming to predict non-linear power storage and delivery dynamic behavior of a LIB, given the charge and discharge demand control input, which is significantly different from the conventional ECM and first principle electrochemical models. The commonly used LSSVF identification method is extended to the proposed fractional model combined in the voltage and current model, respectively, to monitor the charge/discharge demand signal and power storage and delivery output signal in real time. This method demonstrates power storage and delivery prediction capability of a lithium iron phosphate ($LiFePO_4$) battery, not only

in normal operating range, but also in some extreme situations, such as over-charging and over-discharging.

- **State of Charge Balancing:** This dissertation addresses battery heterogeneity of a parallel connection of battery modules by taking advantage of buck regulators integrated on each battery module. The current scheduling strategies are comprehensively formulated in both an open-loop and a closed-loop implementation to balance the current out of each battery module and provide a desire power flow from the battery pack. These novel scheduling strategies are validated through a battery pack of parallel connected battery modules with different battery module characteristic parameters. The experimental results illustrate the feasibility and effectiveness of the proposed current scheduling methods in a real battery application, which motivates future research on developing scheduling algorithms to optimize power flow out of a battery pack.

1.4 Organization

The remainder of the dissertation is organized as follows:

Chapter 2 introduces and validates fractional modeling method and improves the method with CT system identification approaches. These methods demonstrate feasibility and accuracy for LIB in real applications, where the storage resolution is limited and the system dynamics is stiff.

Chapter 3 proposes and validates a novel modeling approach for a single LIB system as BESS to predict power storage and delivery dynamics in both normal operating range and some extreme situations.

Chapter 4 presents and illustrates current scheduling strategies for a parallel-connected battery systems to coordinate and balance the current output of each individual battery system in real applications.

Chapter 5 includes the conclusion of this thesis and provides suggestions on future work.

Chapter 2

Modeling of Battery System

2.1 Introduction

One of the most important functions of a BMS in BESS application is to find a battery model for system monitoring and battery fault detection , where the battery algorithms can be used to accurately capture battery dynamics and monitor the state of battery [26]. A battery model can be described by a physics-based electrochemical model that uses a set of partial differential equations (PDEs) [2]. A typical physics-based electrochemical PDE model uses an insertion composite cathode, a solid polymer electrolyte, and a lithium anode to account for battery dynamics underlying electrochemistry principles, as shown in Figure 2.1. Such a physics-based model has the advantage of being able to describe specific battery information in terms of various physical processes occurring inside a battery from first principle. Unfortunately, it suffers from the disadvantage of model uncertainty for which parameter estimation techniques may be used. Moreover, the complexity of a physics-based model may suffer from parameter identifiability limitations, especially when only the external information of voltage (V), current (I) and temperature (T), is available [27].

To simplify parameter estimation and simulation calculations, model complexity reduction can be considered via porous electrode models that use a polynomial approximation model (PAM) or a single particle model (SPM) as shown in Figure 2.2. A parabolic profile is utilized to approximate the concentration within each spherical particle of both electrodes in a PAM.

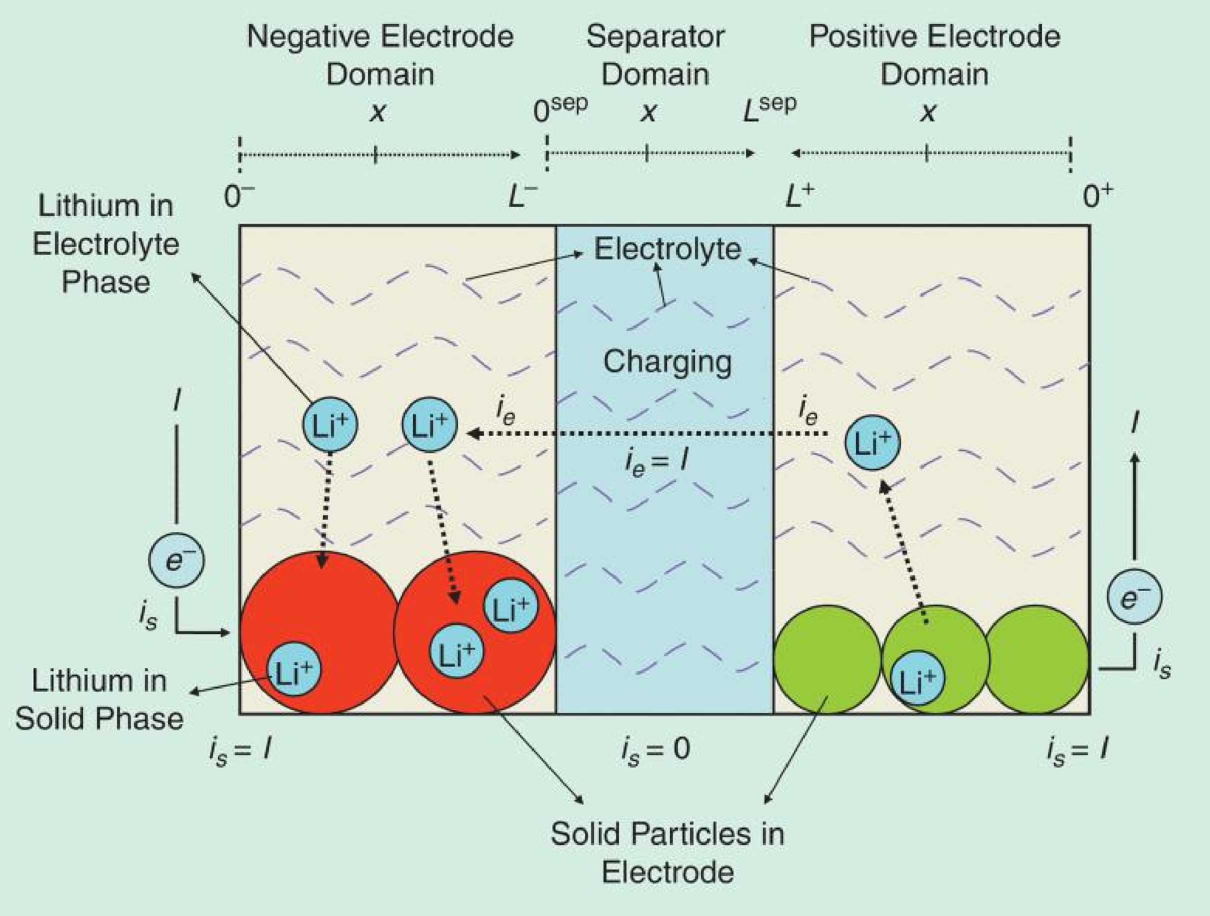

Figure 2.1. Simple schematic showing the electrochemical modeling approach for Li-ion battery cell [2].

Similarly, a single spherical particle, where area is equal to the active area of the solid phase in the porous electrode, is applied to represent each electrode in a SPM [28]. Although both simplified PAM and SPM are computationally much faster than standard physics-based models, they still have own limitations to estimate battery performance, because simplified models do not consider all physics processes [29].

Due to relatively simple structure, equivalent circuit model (ECM) is widely gaining popularity as another alternative model in designing a model for the BMS. An ECM has far less model parameters (to be estimated) and the underlying ordinary differential equation model simplifies firmware implementation. As shown in Figure 2.3, a resistor-capacitor (RC) network model, consisting of internal resistance, effective capacitance and equivalent potential, is widely

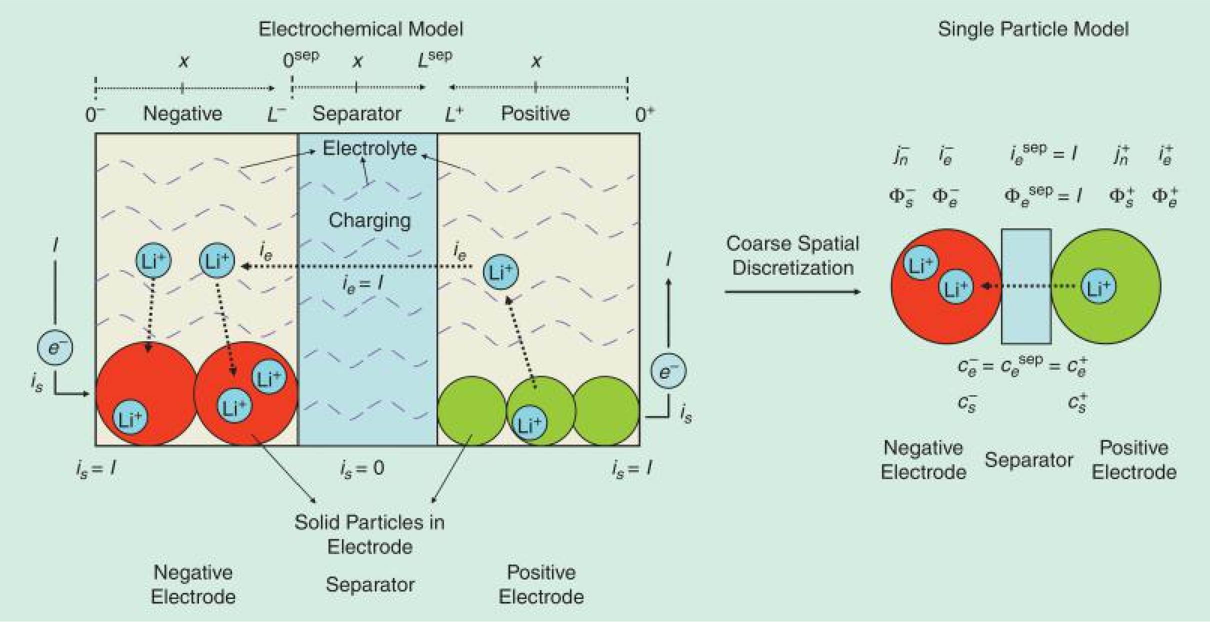

Figure 2.2. Schematic diagram of the single particle model for Li-ion battery cell [2].

applied in constructing ECM models to mimic the phenomenological effects of a battery [30]. There are some commonly applied RC network models, such as 1-RC model, 2-RC model. and 1-RC hysteresis model. Although RC network models have clear electrical interpretations, the internal model properties that include the finite integer order and linearity, are not able to capture the partial derivative nature of a Li-ion battery over the full operating range. The limitations of RC network models can be observed particularly well when comparing the structural mismatch of experimental measurements of characterizing electrochemical systems [31].

Therefore, it is necessary to figure out a simple model to accurately capture the non-linear behavior over the full operating range of typical LIB Nyquist plot illustrated in Figure 1.3, motivated by structure mismatch and complicated parameter estimation of integer ECMs.

An alternative and successful approach to find accurate, but still low complexity models of battery systems is to use a fractional differential model (FDM). A FDM has non-integer derivatives for states can be applied to fix reconcile discrepancies between structure complexity and estimation accuracy in common ECMs. FDMs are able to explain inherent fractional derivative properties due to diffusion dynamics, memory hysteresis, and mass transfer of LIBs, thus they

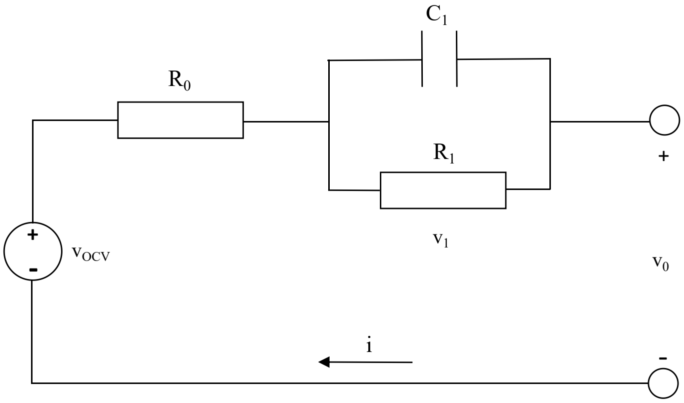

Figure 2.3. Schematic diagram of the equivalent circuit model (ECM).

have ability to exhibit better accuracy with fewer parameters, compared with conventional integer ECMs [32].

2.2 Fractional Differential Systems

Fractional differential systems have been widely applied in various application fields, such as physical chemistry, electricity, electronics, mechanics, automatic control, robotics and signal processing, because their dynamics behaviors can be described by differential equations involving fractional derivatives functions (fractional differential equations) [33]. For most dielectric/insulating materials in electrical application, the current and the voltage across the capacitor are non-linear related: the current is proportional to time non-integer derivative of the voltage across the capacitor [34]. Also, unlike the well-known conventional ”integer” methods, the non-integer derivative allows an explanation of mass transport, diffusion, and memory in dielectrics [35]. For a battery system, especially LIB system, the fractional differential system is applied in capturing the electrical dynamics including mass transport and charge transfer process in the electrolyte, mass diffusion and porosity in solid electrodes [36].

2.2.1 General Linear Fractional Differential System Equation

A general linear fractional differential system can be expressed by a fractional differential equation of the following form

$$y(t)+a_1\mathrm{D}^{\alpha_1}y(t)+...+a_n\mathrm{D}^{\alpha_n}y(t)=b_0D^{\beta_0}u(t)+b_1\mathrm{D}^{\beta_1}u(t)+...+b_m\mathrm{D}^{\beta_m}u(t) \tag{2.1}$$

where $(a_j,b_i)\in\mathbb{R}^2$, differentiation orders $\alpha_1<\alpha_2<...<\alpha_n$, $\beta_0<\beta_1<...<\beta_m$, and $\alpha_i,\beta_i\in\mathbb{R}^+$ (restricted to arbitrary positive real-number value). The fractional differentiation operator for real-number value of α when α takes a non-integer value can be defined as [37]

$$\mathrm{D}^{\alpha}=(\frac{\mathrm{d}}{\mathrm{d}t})^{\alpha},\quad \forall\alpha\in\mathbb{R}^+ \tag{2.2}$$

The classical form of fractional derivative in Riemann-Liouville (R-L) sense to a function $f(t)$ is commonly defined by [34]

$$\mathrm{D}^{\alpha}f(t)=(\frac{\mathrm{d}}{\mathrm{d}t})^{\lceil\alpha\rceil}\frac{1}{\Gamma(\lceil\alpha\rceil-\alpha)}\int_0^t\frac{f(\tau)}{(t-\tau)^{\alpha-\lfloor\alpha\rfloor}}\mathrm{d}\tau \tag{2.3}$$

where $\forall\alpha\in\mathbb{R}^+$, $t>0$, and gamma function $\Gamma(\gamma)$ for every $\gamma\in\mathbb{R}^+$ can be defined via a convergent improper integral:

$$\Gamma(\gamma)=\int_0^{\infty}z^{\gamma-1}\mathrm{e}^{-z}\mathrm{d}z \tag{2.4}$$

It should be noted that in the above equations the floor function $\lfloor\cdot\rfloor$ represents the largest integer smaller than or equal to α, and the ceiling function $\lceil\cdot\rceil$ defines the smallest integer larger than or equal to α. An alternative definition called Grünwald-Letnikov (G-L) allows the derivative a non-integer value instead of the integral is considered as the following definition [35]

$$\mathrm{D}^{\alpha}f(t)=\lim_{h\to 0}\frac{(-1)^{\alpha}}{h^{\alpha}}\sum_{j=0}^{[\frac{t-a}{h}]}(-1)^j\left(\begin{array}{c}\alpha\\ j\end{array}\right)f(t+jh) \tag{2.5}$$

where $[\cdot]$ donates the integer part. The Laplace transform of α-th derivative ($\alpha \in \mathbb{R}^+$) of an arbitrary signal $f(t)$

$$\mathscr{L}\{\mathrm{D}^{\alpha} f(t)\} = s^{\alpha} F(s), \text{ if } f(t) = 0 \ \forall t \leq 0 \tag{2.6}$$

can then be generally applied as a more concise algebraic tool to describe fractional differential systems [38]. Thus this allows to rewrite the fractional differential equation (2.1), with both input signal $u(t)$ and output signal $y(t)$ equal to 0 when $t = 0$ (zero initial conditions), into a transfer function form

$$\mathrm{G}(s) = \frac{b_0 s^{\beta_0} + b_1 s^{\beta_1} + \cdots + b_m s^{\beta_m}}{1 + a_1 s^{\alpha_1} + \cdots + a_n s^{\alpha_n}} \tag{2.7}$$

It should be noted that in the above equations the floor function $\lfloor\cdot\rfloor$ represents the largest integer smaller than or equal to α, and the ceiling function $\lceil\cdot\rceil$ defines the smallest integer larger than or equal to α. An alternative definition called Grünwald-Letnikov (G-L) allows the derivative a non-integer value instead of the integral is considered as the following definition [35]

$$\mathrm{D}^{\alpha} f(t) = \lim_{h \to 0} \frac{(-1)^{\alpha}}{h^{\alpha}} \sum_{j=0}^{[\frac{t-a}{h}]} (-1)^{j} \begin{pmatrix} \alpha \\ j \end{pmatrix} f(t + jh) \tag{2.8}$$

where $[\cdot]$ donates the integer part. The Laplace transform of α-th derivative ($\alpha \in \mathbb{R}^+$) of an arbitrary signal $f(t)$

$$\mathscr{L}\{\mathrm{D}^{\alpha} f(t)\} = s^{\alpha} F(s), \text{ if } f(t) = 0 \ \forall t \leq 0 \tag{2.9}$$

can then be generally applied as a more concise algebraic tool to describe fractional differential systems [38]. Thus this allows to rewrite the fractional differential equation (2.1), with both input signal $u(t)$ and output signal $y(t)$ equal to 0 when $t = 0$ (zero initial conditions), into a transfer function form

$$\mathrm{G}(s) = \frac{b_0 s^{\beta_0} + b_1 s^{\beta_1} + \cdots + b_m s^{\beta_m}}{1 + a_1 s^{\alpha_1} + \cdots + a_n s^{\alpha_n}} \tag{2.10}$$

The transfer function $\mathrm{G}(s)$ in (2.10) is applied in the continuous-time identification of the FDMs throughout this paper.

2.2.2 Numerical Analysis of Fractional Derivatives

The reversed Grünwald-Letnikov (reversed G-L) definition in the similar form with (2.8)

$$\mathrm{D}^{\alpha} f(t) = \lim_{h \to 0} \frac{1}{h^{\alpha}} \sum_{j=0}^{[\frac{t-a}{h}]} (-1)^{j} \begin{pmatrix} \alpha \\ j \end{pmatrix} f(t - jh) \tag{2.11}$$

is carried out to simulate the system response to an arbitrary input signal in time-domain analysis of a fractional derivative system. The closed-form numerical solution to the general fractional differential equation (2.1) in reversed G-L form can be computed by the recursive approach [39]

$$y_t = \frac{1}{\sum_{i=0}^{n} \frac{a_i}{h^{\alpha_i}}} \left(u_t - \sum_{i=0}^{n} \frac{a_i}{h^{\alpha_i}} \sum_{j=1}^{[\frac{t-a}{h}]} w_j^{(\alpha_j)} y_{t-jh} \right) \tag{2.12}$$

where h represents the step-size in computation. The $w_j(\alpha)$ in the above solution (2.12) can be evaluated recursively from

$$w_0^{\alpha} = 1, w_j^{\alpha} = (1 - \frac{\alpha + 1}{j}) w_{j-1}^{\alpha}, j = 1, 2, ... \tag{2.13}$$

The above recursive method can be applied to obtain numerical approximation of fractional derivative input and output signals. The signal $\hat{u}(t)$ is calculated by using (2.11) substituting $(-1)^{\alpha} \begin{pmatrix} \alpha \\ j \end{pmatrix}$ = w_j^{α} and the time response under the signal $u(t)$ can be consequently obtained. Since the recursive approach is based on the fixed-step computation, the step-size h needs to be selected with special care to improve the accuracy of the simulation. Therefore, it is necessary to take sometime to validate the computational results by decreasing step-size h in a gradual way until the simulation results have no variation.

2.3 Continuous-time Battery Model Identification

There are various parameter identification approaches that can be employed to determine the unknown parameters of a FDM for a battery system. A recently published parameter estimation method [1] has shown to provide good results, but requires a large number of time consuming integration and convolution calculations. In addition, this method requires noise-sensitive identification to estimate the fractional derivative value and estimation error is caused by numerical simulation [40]. Although alternate indirect identification method of discrete-time (DT) model parameters can be used to solve the above issues, information on fast dynamics may be lost due to sampling, whereas relatively too small sampling time will result to numerical problems that limits DT model identification [41]. Furthermore, estimation of model parameters may be sensitive to initial and noise conditions and limits the potential of real-time applications [42]. In order to overcome disadvantages of DT method, a direct CT system identification can been applied, because it can provide good insight of system properties and avoid information loss due to undesired high sensitivity issues [43]. The direct CT system identification has been analyzed and compared with indirect DT system identification methods in battery applications [44].

2.3.1 Advantages of Continuous-time Over Discrete-time Model Identification

DT model identification based on sampled input/output data set has been successfully applied in estimation of CT dynamics processes by digital computers and data acquisition systems (DAS). However, the difficulties or limitations of using DT model identification in LIB applications have been encountered when applying various sampling rate (or sampling interval). High sampling rate can lead to numerical problems due to discrete poles constrained in small area close to the unit circle boundary of the z-plane, whereas low sampling rate is not able to retain all the system information [45]. Since LIB system consists of both fast and slow dynamic modes of behavior, which reveals a typical stiff system, the selection of sampling rate (sampling interval) needs to be treated with excessive care [46]. On the one hand, the slow sampling (large sampling interval) will lead to the information loss due to the existence of the fast dynamics. On the other hand, the rapid sampling (small sampling interval) is able to accurately capture the fast system dynamic, however, this will result in the inaccuracy of parameter estimation because of ignorance of the slow dynamics in real system [47]. Moreover, the numerical precision of DT system is more inclined to be affected by the estimation parameters and the discrete pole location that is located near the stability boundary within limited storage resolution [48]. As the sampling rate increases, the disturbance sensitivity of capacitance and resistance values increases the quasilinear utility in the RC networks, which ultimately leads to inaccurate results of the system identification [49].

The direct CT system identification has been thoroughly studied in contrast with the indirect DT identification [50]. When applied to model identification and parameter estimation in using data collected when choosing the appropriate sampling rate, the CT identification methods have particular advantages over well-established DT methods for system modeling and control system design: (1) the CT identification methods are preferable to represent underlying dynamic system in better physical insight, exhibit the preservation of a priori knowledge, and show built-in capability to deal with the situation of non-uniformly sampled data; (2) the CT approach includes inherent filtering, which not only can significantly improve the statistical efficiency, but also makes more robust to measurement noises; (3) the CT identification method can efficiently avoid discretization that induces undesired high sensitivity issues, therefore it can result in better identification performance of the stiff system [51]. Therefore, considered all above advantages, the direct CT identification approach is utilized to the parameter identification throughout the paper.

2.3.2 Least Squares-based State-variable Filter Method

In order to consider CT parameter estimation of the FDM in (2.1) or transfer function $G(s)$ in (2.10), it is assumed that measurable output signal $y(t)$ is corrupted by an additive measurement white noise $e(t)$

$$y(t) = y_0(t) + e(t) \tag{2.14}$$

where $y_0(t)$ is hypothetical noise-free deterministic system output. It is worth noting that the input signal $u(t)$ and the output signal $y(t)$ are considered to be related with the fractional differential equation (2.1). Therefore, the equation error is then expressed as the following form [52]

$$\varepsilon(t) = y(t) - \varphi(t)^T \theta \tag{2.15}$$

where the regressor vector is defined as

$$\varphi(t) = \left[\mathrm{D}^{\beta_0} u(t) \; \ldots \; \mathrm{D}^{\beta_m} u(t) \;\; -\mathrm{D}^{\alpha_1} y(t) \; \ldots \; -\mathrm{D}^{\alpha_n} y(t)\right]^T \tag{2.16}$$

and the parameter is denoted by the vector

$$\theta = [b_0 \, b_1 \ldots b_m \, a_1 \, a_2 \ldots a_n]^T \tag{2.17}$$

A mathematical approach to determine parameter vector θ is minimizing L_2 norm of $\varepsilon(t)$

$$J = \int_0^T (\varepsilon(t))^2 \mathrm{d}t \tag{2.18}$$

In the present case, output signal $y(t)$ is highly linear to the parameter vector θ, thus J is minimized analytically in the following least squares (LS) estimate

$$\hat{\theta}_{\mathrm{LS}} = \left(\int_0^T \varphi(t)^T \varphi(t) \mathrm{d}t \right)^{-1} \int_0^T \varphi(t)^T y(t) \mathrm{d}t \tag{2.19}$$

In order to numerically compute the LS estimate in (2.19), the discretization of fractional derivative input and output signals is needed to transfer continuous functions and equations into discrete counterparts. Considering time digitized regression vector $\varphi(kT_s)$, time instant T_s and $k = 1, 2, \ldots, N$ based on N data points, the regressor matrix Φ can be then formulated as

$$\Phi = [\varphi(T_s)\ \varphi(2T_s)\ \ldots\ \varphi(NT_s)]^T \tag{2.20}$$

and the digitized system output $y(kT_s)$ can be formed as a column vector to describe output matrix $\mathbf{Y}$ in a similar way. The CT LS parameter estimation can be computed via

$$\hat{\theta}_{LS} = (\Phi^T\Phi)^{-1}\Phi^T\mathbf{Y} \tag{2.21}$$

Because CT stochastic processes are always related with the white noise and its derivatives, parameter estimation normally would encounter difficulties: small perturbations that contaminating on the coefficient or the initial condition of the differential equation would finally result in the perturbations of the solution [53]. Therefore, special care is needed in parameter estimation of the fully stochastic FDM CT model in order to reduce the noise/deviation on the input/output data in order to alleviate the practical difficulties. A traditional and effective approach to estimate coefficients of (fractional order) CT model is to use a minimum-order SVF filter to both sides of (2.15) [54]. From the signal analysis perspective, the SVF consisted of multiple band-pass filters can be applied to gain differentiation behavior in low frequency part, and to filter (smooth) noise/perturbation effect in high frequency part. A typical SVF filter is chosen with operator model $L(s)$ in the following form [55]

$$L(s) = \frac{1}{E(s)} = \left(\frac{\gamma}{s+\gamma}\right)^n \tag{2.22}$$

where n is the highest system order, and γ represents the cut-off frequency of the SVF. It should be noted that since the cut-off frequency γ is selected to emphasize the filter frequency band and define the bandwidth of the filter, the recommended γ value in general is chosen to be slightly larger than the frequency bandwidth of the identified system [45]. Hence, filtered input u_f and output y_f can be obtained at the output of the filters (2.22)

$$u_f(t) = L(s)u(t) \tag{2.23}$$

and

$$y_f(t) = L(s)y(t) \tag{2.24}$$

By using the filters defined in (2.22), the fractional equation (2.1) can be extended to the (fractional) derivatives form as to formulate the standard least squares-based SVF (LSSVF) method

$$y_f(t) + a_1\mathrm{D}^{\alpha_1}y_f(t) + ... + a_n\mathrm{D}^{\alpha_n}y_f(t) = b_0\mathrm{D}^{\beta_0}u_f(t) + b_1\mathrm{D}^{\beta_1}u_f(t) + ... + b_m\mathrm{D}^{\beta_m}u_f(t) \tag{2.25}$$

Instead of minimizing the L_2 norm of $\varepsilon(t)$ as in (2.15), the L_2 norm of $\varepsilon_f(t)$ is now minimized based on the filtered fractional equation in (2.25)

$$\varepsilon_f(t) = y_f(t) - \varphi_f(t)^T\theta \tag{2.26}$$

where the regressor vector is composed of the filtered input/output signals as the following form

$$\varphi_f(t) = \left[\mathrm{D}^{\beta_0}u_f(t) \ \ \dots \ \ \mathrm{D}^{\beta_m}u_f(t) \ \ -\mathrm{D}^{\alpha_1}y_f(t) \ \ \dots \ \ -\mathrm{D}^{\alpha_n}y_f(t)\right]^T \tag{2.27}$$

Again, the same discretization approach is applied to numerically compute the (fractional) derivatives of the input/output signals to estimate parameters. Combined a time digitized filtered regression vector $\varphi_f(kT_s)$ with the filtered system output $y_f(kT_s)$ column vector $\mathbf{Y}_f$, time instant

T_s and $k = 1, 2, \ldots, N$, the CT LSSVF estimate can be formulated as

$$\hat{\theta}_{LSSVF} = (\Phi_f^T \Phi_f)^{-1} \Phi_f^T \mathbf{Y}_f \tag{2.28}$$

where

$$\Phi_f = [\varphi_f(T_s)\ \varphi_f(2T_s)\ \ldots\ \varphi_f(NT_s)]^T \tag{2.29}$$

2.3.3 Instrumental Variable-based State-variable Filter Method

The basic LSSVF method has some attractive properties and include the analytical solution that is relatively easy to compute, low computational complexity, and quite good robustness with respect to noise. However, it is well know the resultant parameter estimates are asymptotically biased in the presence of non-white equation noise on the regression equation. The main reason comes from the fact that the filtered regression vector $\varphi_f(kT_s)$ is correlated with the filtered noise term $\varepsilon_f(kT_s)$ [50]. As a traditional variant of the LS method, the instrumental variable (IV) method can deliver unbiased estimates and also has the advantage of relying on linear regression techniques.

The primary principle of the IV method relies on the so-called instruments generally obtained from a parallel model y_f^{IV}. Hence, the most common IV identification method uses an auxiliary model in order to generate noise-free output estimate

$$\varphi_f^{IV}(t) = \left[\mathrm{D}^{\beta_0} u_f(t) \ \ \ldots \ \ \mathrm{D}^{\beta_m} u(t) \ \ -\mathrm{D}^{\alpha_1} y_f^{IV}(t) \ \ \ldots \ \ -\mathrm{D}^{\alpha_n} y_f^{IV}(t) \right]^T \tag{2.30}$$

The IV vector should satisfy the following as

$$\mathrm{E}\left[\varphi_f^{IV}(t) \varphi_f^T(t) \right] \text{ is non singular} \tag{2.31}$$

and

$$\mathrm{E}\left[\varphi_f^{IV}(t) \varepsilon_f(t) \right] = 0 \tag{2.32}$$

where E[·] stands for the mathematical expectation. The continuous-time instrumental variable-based filter (CT IVSVF) estimation can be given as

$$\hat{\theta}_{IVSVF} = (\Phi_f^{IV^T}\Phi_f)^{-1}\Phi_f^{IV^T}\mathbf{Y}_f \tag{2.33}$$

where

$$\Phi_f^{IV} = [\varphi_f^{IV}(T_s)\ \varphi_f^{IV}(2T_s)\ \dots\ \varphi_f^{IV}(NT_s)]^T \tag{2.34}$$

and the column vector $\mathbf{Y}_f$ is the same as (2.29). The implementation of CT IVSVF parameter estimation is summarized in the overall flow chart as shown in Fig. 2.4.

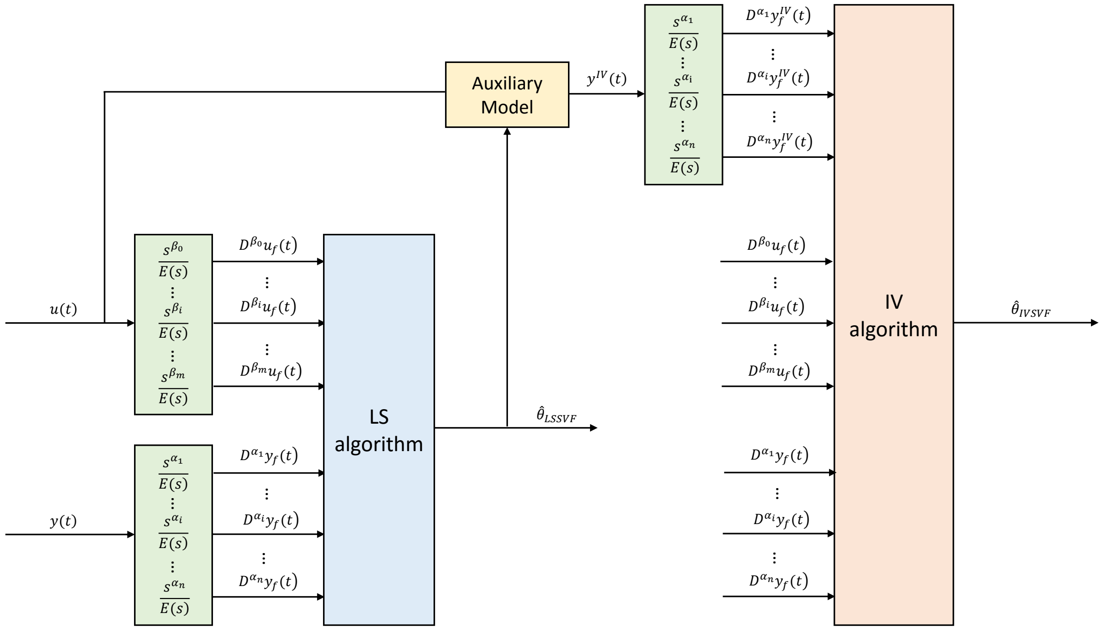

Figure 2.4. Implementation flow of continuous-time instrumental variable-based state-variable filter (CT IVSVF) parameter estimator.

Compared with conventional LS identification methods, IV methods have the advantages of providing consistent parameter estimates when the noise in real applications can not comply with a normal distribution and rational spectral density [56]. As one of the available IV methods, the simplified refined instrumental variable for continuous-time system identification (SRIVC) has been introduced to solve the problem of formulating unbiased parameter estimates. Although the SRIVC method is a powerful IV method for unbiased parameter estimation with proven statistical efficiency properties and exhibits statistically consistent and asymptotically efficient parameter estimates in the presence of white measurement noise [57], the parameter estimation requires detailed modeling of the noise filter to obtain the statistical efficiency [58]. The pre-filters and the highly colored noise present on the (filtered) LIB experimental measurements may require complex noise filters to achieve this statistical efficiency of SRIVC and require additional computations that can be avoided by choosing an instrument that is not optimal in terms of variance properties. Therefore, the above proposed IVSVF identification approach is selected to estimate parameters and compare performance/accuracy with LSSVF estimation method throughout this paper, because of its ability to provide consistent estimate results for non-white noise structure in LIB system experimental data.

2.4 Continuous-time Fractional Differential Model for a Lithium Ion Battery

ECMs have been widely applied in BMS and compared with twelve commonly used ECMs, the first-order RC model (1-RC) is considered to be the best choice for LIB in terms of model complexity, model accuracy, and generalizability to multiple cells [59]. However, simple elements, such as capacitances, resistances, inductances or convective diffusion impedance, are not able to describe the experimental frequency dispersion result of a solid electrode/electrolyte interface [60].

A constant-phase element (CPE) can be generally applied to describe the capacitance dispersion of the frequency dispersion that is normally ascribed to distributed surface reactivity, electrode porosity, surface inhomogeneity, roughness or fractal geometry, current and potential distributions associated with electrode geometry instead of an ideal capacitor. Therefore, CPEs are used extensively in ECMs and the derived FDM structure is shown in Figure 2.5. From the description in Figure 2.5, it is worth mentioning that an ohmic resistor (R_0) can be applied to depict resistive impedance, a parallel circuit composed of a resistor (R_1) and a CPE, is used to represent the diffusion dynamic behavior.

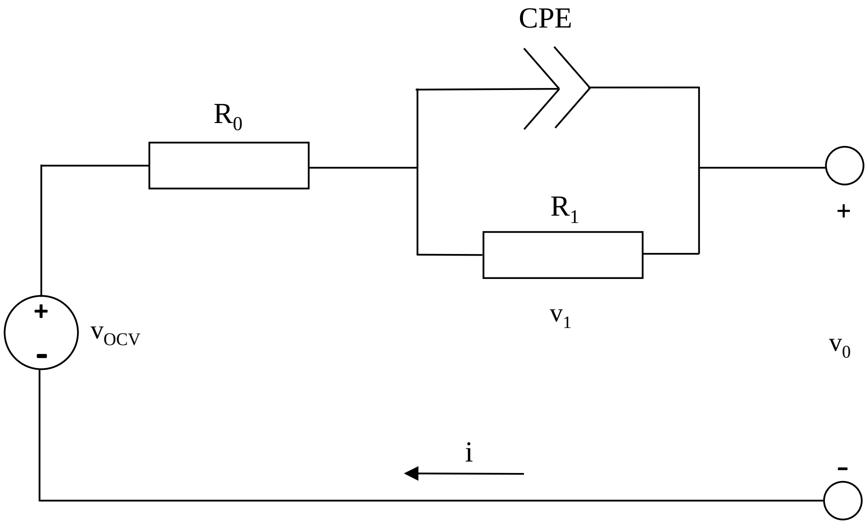

Figure 2.5. Structure of the fractional differential model for Li-ion batteries.

The CPE is an equivalent electrical circuit component that appears currently in modeling the behavior of the imperfect dielectrics (partially capacitive and resistive) [61]. The electrical impedance can be expressed in terms of capacitance-like parameter C_1 and the differentiation order α ($\alpha \in \mathbb{R}^+$, $0 < \alpha < 1$)

$$Z_{CPE}(s) = \frac{1}{Y_{CPE}(s)} = \frac{1}{C_1 S^{\alpha}} \tag{2.35}$$

where the CPE admittance $Y_{CPE}(s)$, C_1 and α are frequency independent. Since constant phase is always -90 °, the CPE as a circuit parameter is exhibiting limited behavior: an ideal capacitor for α=1, and a pure resistor for α=0 [62]. In this case (2.35), although CPE can be used as an extremely flexible fitting parameter to fit EIS data, it is not able to describe the meaning in terms of time constant distribution. The CT transfer function of the first-order FDM depicted in

Figure 2.5 can be derived as

$$H(s) = \frac{V_{OCV}(s) - V_0(s)}{I(s)} = \frac{V(s)}{I(s)} = R_0 + \frac{R_1}{1 + R_1 C_1 s^{\alpha}} \tag{2.36}$$

where $V_{OCV}(s) = \mathscr{L}\{v_{OCV}(t)\}$, $V_0(s) = \mathscr{L}\{v_0(t)\}$, $I(s) = \mathscr{L}\{i(t)\}$, and $\mathscr{L}\{\cdot\}$ is the notation for the Laplace transform.

The following relationship can be obtained from the whole circuit shown in Figure 2.5

$$v_0 = v_{OCV} - v_1 - iR_0 \tag{2.37}$$

where i, v_0 and R_0 are the current, output voltage, and ohmic resistance, v_{OCV} is the open circuit voltage (OCV), v_1 and $\tau = R_1 C_1$ are the voltage and time constant of an RC circuit, respectively. The output function (2.37) consisted of state variable v_1, v_{OCV}, and implicit determining factor input current i.

All coefficients are replaced by the unknown circuit parameters, then the transfer function of first-order FDM (2.36) can be rewritten as

$$H(s) = \frac{V(s)}{I(s)} = \frac{b_0 + b_1 s^{\alpha}}{1 + a_1 s^{\alpha}} \tag{2.38}$$

where the identified parameters are

$$b_0 = R_0 + R_1 \tag{2.39}$$

$$b_1 = R_0 R_1 C_1 \tag{2.40}$$

$$a_1 = R_1 C_1 \tag{2.41}$$

The above transfer function (2.38) can be described in a fractional differential equation form as

$$(1+a_1s^{\alpha})V(s) = (b_0+b_1s^{\alpha})I(s) \tag{2.42}$$

The current input $i(t)$ and voltage output $v(t) = v_{OCV}(t) - v_0(t)$ related with (2.42) can then be expressed as the following regression form

$$v(t) = \varphi_{FDM}(t)^T\theta_{FDM} \tag{2.43}$$

where the revised regression vector $\varphi_{FDM}(t)$ is defined as

$$\varphi_{FDM}(t) = [i(t)\ \mathrm{D}^{\alpha}i(t)\ \ -\mathrm{D}^{\alpha}v(t)]^T \tag{2.44}$$

and the parameters are denoted by the vector

$$\theta_{FDM} = [b_0\ b_1\ a_1]^T \tag{2.45}$$

In most practical situations, the measured terminal battery voltage is usually the noise-free case, and it is actually corrupted by additive noises. Therefore, the complete equation for the battery system, with an equation error $\varepsilon(t)$, can be written in the regression form

$$v(t) = \varphi_{FDM}(t)^T\theta_{FDM} + \varepsilon(t) \tag{2.46}$$

Low-pass first-order SVF $L(s)=\frac{\gamma}{s+\gamma}$, as the most simple form in (2.22), is then applied to smoothen (filter) the time-derivative of current input and voltage output. Then, the filtered equation error can be defined as to estimate parameters

$$\varepsilon_f^*(t) = v_f(t) - \varphi_{FDM}^*(t)^T\theta_{FDM} \tag{2.47}$$

where the filtered regression vector can be given by

$$\varphi_{FDM}^{*}(t) = [i_f(t)\ \mathrm{D}^{\alpha} i_f(t)\ \ -\mathrm{D}^{\alpha} v_f(t)]^T \tag{2.48}$$

Subsequently, in order to validate the accuracy of the estimation, the fitness function $f(t)$ can be defined as follows

$$f(t) = ||v_0(t) - v_{sim}(t)||_2^2 \tag{2.49}$$

where $v_0(t)$ is the tested battery terminal voltage and $v_{sim}(t)$ is the simulated battery voltage.

2.5 Experiment

The battery characterization experiments are conducted in order to estimate parameters and validate our proposed model of a Li-ion polymer battery cell.

2.5.1 Battery Tests

Experiment characterization data of Li-ion polymer battery is continuously measured at room temperature (22-25°C) in the testing workbench. The specific information of the Li-ion polymer battery under test is shown in Table 2.1. As shown in Figure 2.6, a static capacity test, an open circuit voltage (OCV) test, a Hybrid Pulse Power Characterization (HPPC) test, and a Urban Dynamometer Driving Schedule (UDDS) test are consecutively conducted in the characterization tests. It should be noted that the sampling rate is 1 Hz in all characterization experiments.

Table 2.1. Specific information of the Li-ion polymer battery under test.

Characterization	**Lithium-ion polymer**
Charge/discharge capacity	40.83/40.61 Ah
Nominal voltage	3.7 V
Minimum discharge voltage	2.7 V
Maximum charge voltage	4.2 V

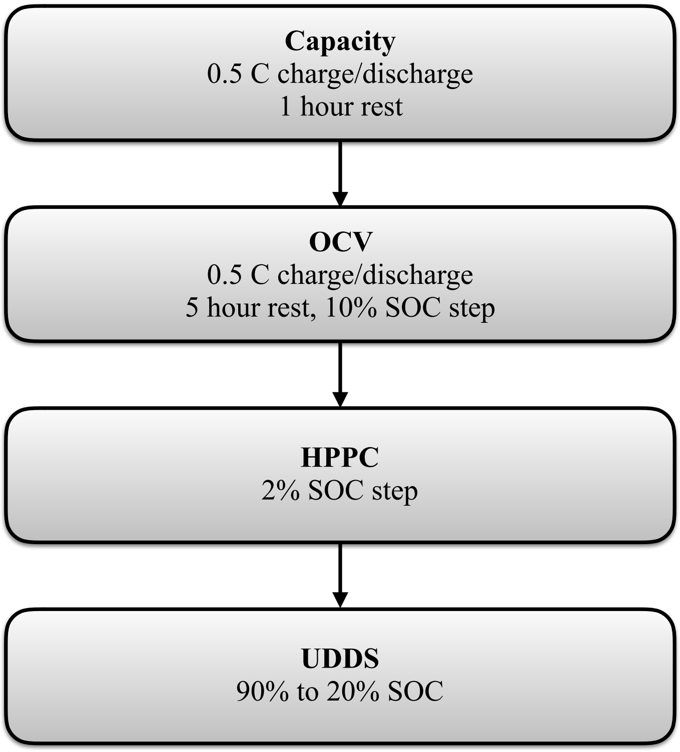

Figure 2.6. Battery characterization procedure.

There are three charge/discharge cycles in the static capacity test. The Li-ion polymer battery is charged at 0.5C (constant current) in each cycle, until the battery terminal voltage can reach the maximum charge voltage (4.2 V). After that, the battery terminal voltage is maintained at the maximum value 4.2 V before the charge rate is below 1/20C. Then, the battery is discharged at a constant rate 0.5C before the battery terminal voltage reaches the minimum discharge voltage (2.7 V). Moreover, 1 hour rest (0C) is then set after each charge/discharge cycle. The average value of all three charge/discharge cycles can be used to calculate the charge/discharge capacity.

As shown in Figure 2.7, the charge/discharge OCV-SOC experimental curves are measured at 10% SOC step with 0.5C charge/discharge rate, and there is a 5 hours rest between two neighboring charge/discharge cycles. As can be seen in Figure 2.7, the discharge OCV curve is slight lower than the charge curve at certain SOC range due to rate-dependent hysteresis. When SOC = 20%, the deviation between charge and discharge OCV curves reaches the maximum value 22.6 mV, as shown in small figure in Figure 2.7. It is worth noting that for the purpose of simplicity in calculation, the average value of the measured charge/discharge OCV-SOC curves is applied in the model identification.

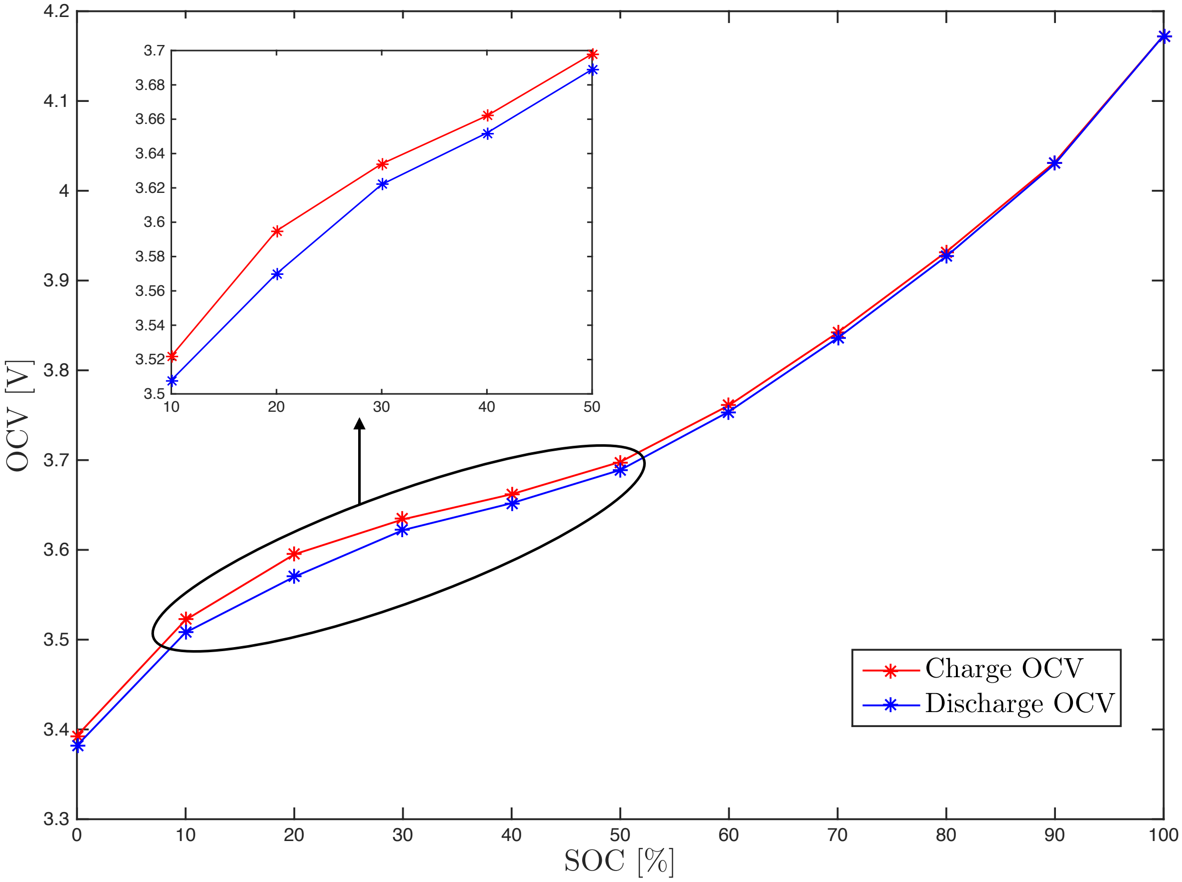

Figure 2.7. Charge/discharge OCV-SOC experimental curves.

Then, a HPPC test profile is intended to determine dynamic power capability in model parameter estimation over the devices usable voltage range using a test profile that incorporates both discharge and charge pulses. The HPPC test begins at 100% fully charged Li-ion battery and terminates after completing the final profile at 0 % SOC with 2% SOC discharge step and 1 hour rest between two consecutive charge/discharge cycles to allow the cell to return to a charge equilibrium condition before applying the next profile. The actual current input of one specific charge/discharge cycle of HPPC profile is shown in Figure. 2.8. The HPPC current characterization profile and voltage response at SOC = 50% is recorded to establish the cells

OCV behavior, which are enlarged in Figure 2.9.

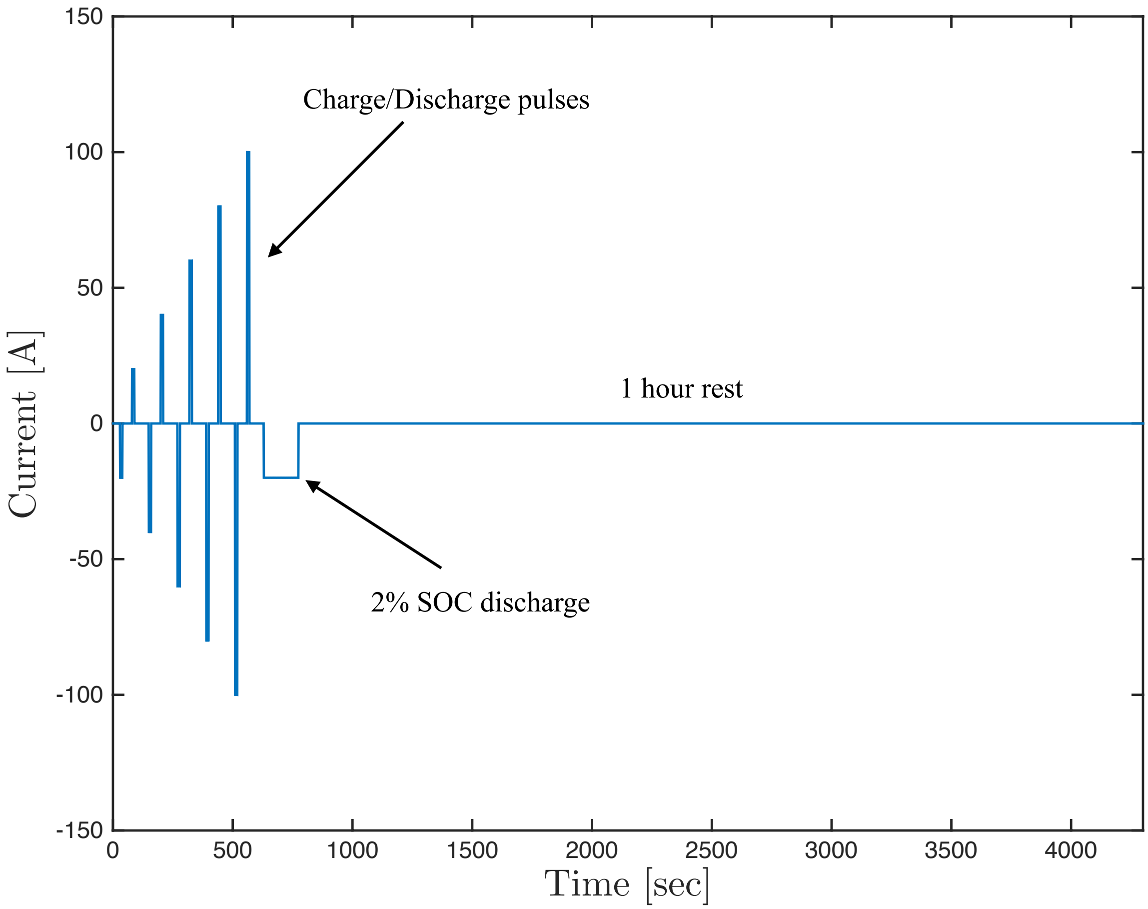

Figure 2.8. HPPC test profile.

UDDS stands for Urban Dynamometer Driving Schedule, mandated dynamometer test on fuel economy that represents city driving conditions which is used for light duty vehicle testing. This manual defines a charge depleting operational mode, which is intended to allow the vehicle to operate in an all-electric mode (propulsion and accessories powered by the electric drive and onboard electric energy storage), with a net decrease in battery SOC. In this dissertation, the specific UDDS datasets that can be used to be able to imitate the battery load of a car to represent city driving conditions at the specific temperatures, and voltage response records are used as model validation datasets in order to assess the simulated models.

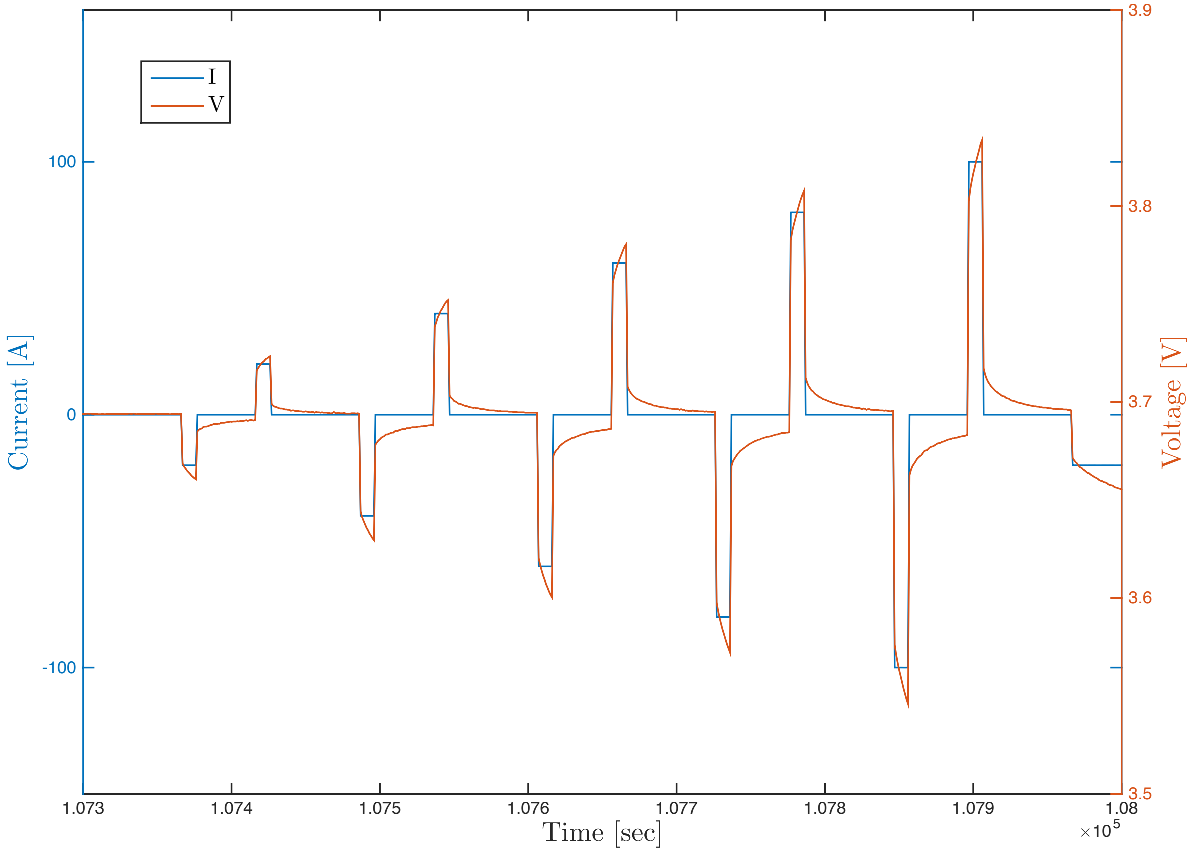

Figure 2.9. HPPC pulses at SOC=50%.

2.5.2 Pre-determination of Non-integer Order

The fitness function $f(t)$ that describes the deviation between the simulated model output and experimental battery terminal voltage, is used to measure the model accuracy and validate the model performance. 1 Hz cut-off frequency for a low-pass filter is selected in order to pre-filter the input/output signals. As a matter of fact, the non-integer order α affects the model accuracy/performance. For this research, the fractional order α is selected from 0.01 to 1.0 with the step length 0.01. The identification process is performed at each α value, and the results are shown in Figure 2.10. As can be seen from Figure 2.10, the fitness function value typically changes when the value of the fractional order varies. It should be mentioned here that when the fractional orders are chosen from 0.01 to 0.35, the values of the fitness function are beyond the range compared with other selected fractional orders. Hence, the range of fractional order shown in Figure 2.10 is chosen from 0.36 to 1 with step size 0.01. The model when the fractional order $\alpha = 0.64$ obtains the smallest value and obtains the best model accuracy/performance under HPPC test cycles. Thus, the optimized fractional order $\alpha = 0.64$ is chosen in the FDM to validate performance throughout this thesis.

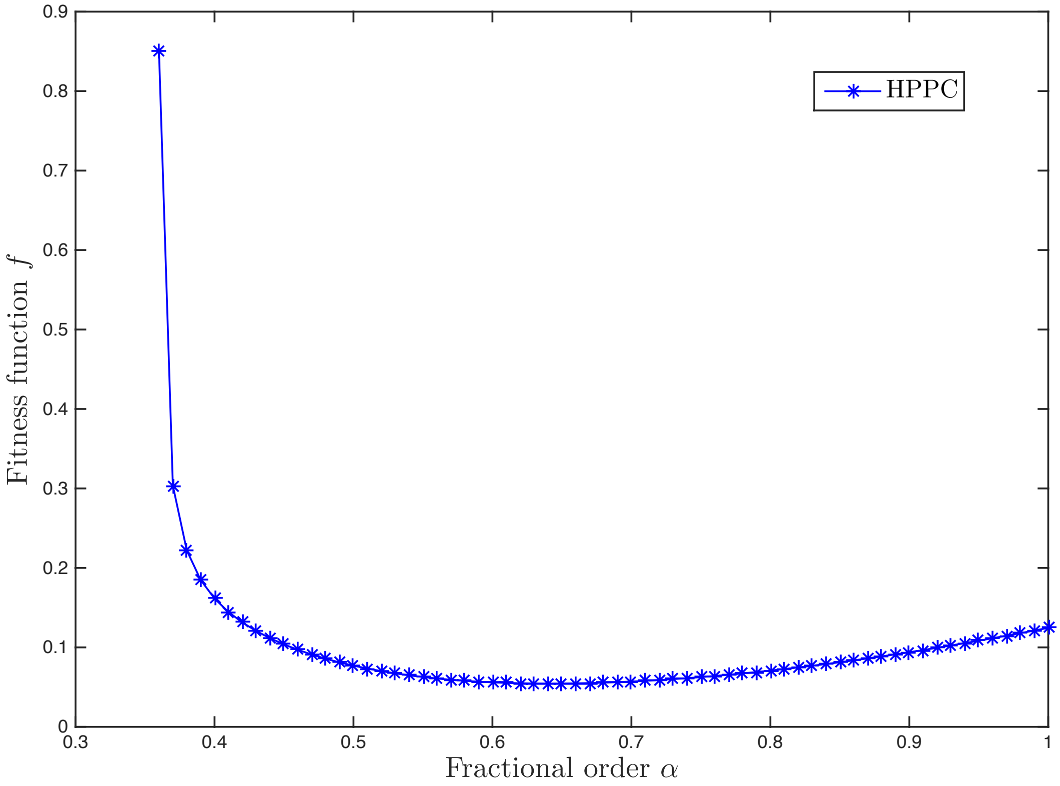

Figure 2.10. Relationship between model accuracy and fraction order.

2.5.3 Validation Results

In order to validate the model accuracy/performance of the aforementioned FDM, the optimized FDM (when $\alpha = 0.64$) is used to compare with same structure first-order integer model (IM) in (2.38) (when $\alpha = 1$) in both CT LSSVF and CT IVSVF system identification. The 1 Hz cut-off frequency is also selected as pre-fliter SVF through the validation process. The validation result for UDDS test is shown in Figure 2.11. The simulated and experimental battery voltage outputs, and voltage errors between the simulated models and experiment data are plotted in Figure 2.11. And the zoom-in range results between 0 s and 2000 s are shown in Figure 2.12. The results show that (1) the IM estimated by LSSVF method has the largest overall error compared with other estimated models; (2) the FDMs offers substantially better performance then IMs in both LSSVF and IVSVF methods; (3) the IVSVF identification method has better performance over LSSVF method in both FDM and IM, because the recent presented IV method is less correlated (more independent) to the equation error; (4) FDM applied by IVSVF identification method appears the best performance compared with other estimated models under UDDS profile, which mainly consists of high frequency contents and is closer to the actual working conditions.

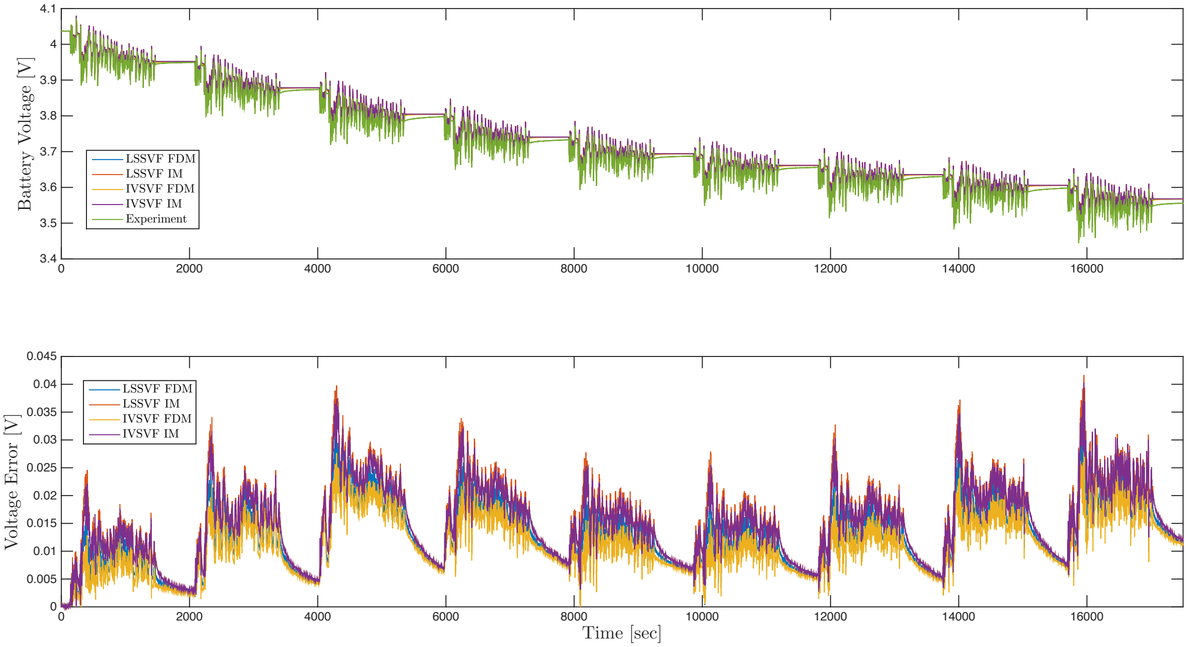

Figure 2.11. Voltage values and errors across all UDDS tests.

The root-mean-square error (RMSE), mean absolute error (MAE) and median absolute deviation (MAD) of above mentioned estimators over the full experimental period are chosen to list in Table 2.2. It validates that the proposed FDMs exhibit better overall performance and the explicitly RMSE, MAE and MAD of the FDM applied IVSVF system identification method is substantially smaller than other estimated models. It can be concluded from the above analysis

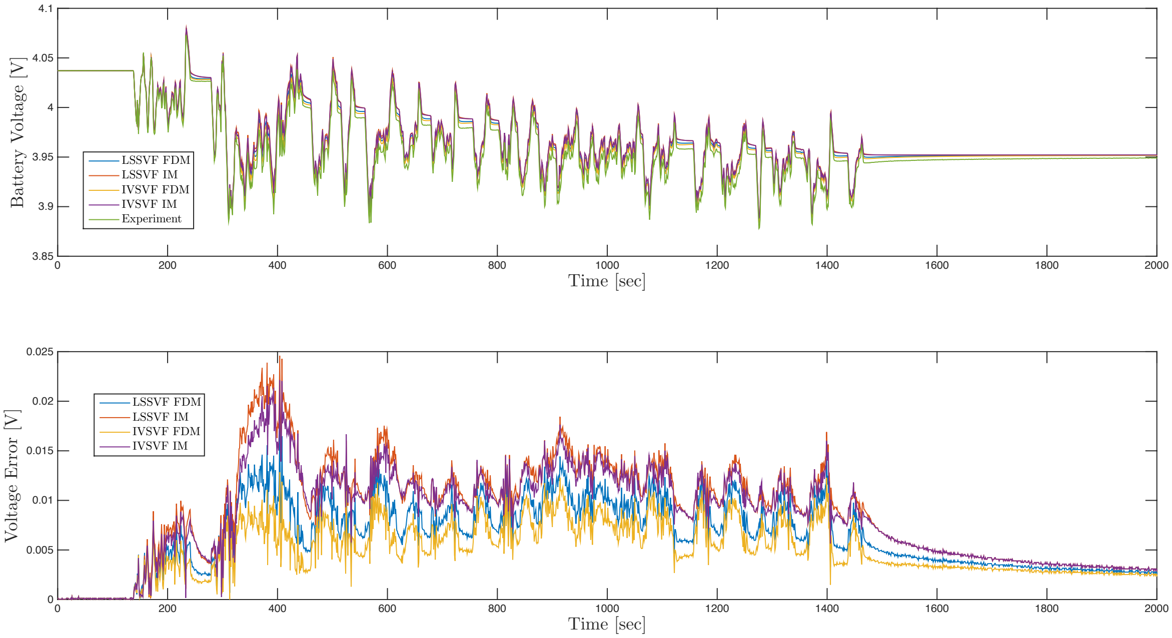

Figure 2.12. Detailed voltage values and errors between 0 s and 2000 s.

that the proposed FDM applied IVSVF method characterizes the Li-ion battery more accurately and shows better performance than other models.

Table 2.2. RMSE, MAE and MAD of model voltage estimation in whole UDDS validation.

	LSSVF IM	LSSVF FDM	IVSVF IM	IVSVF FDM
RMSE [mV]	16.87	12.88	16.30	9.15
MAE [mV]	15.39	11.70	14.92	8.20
MAD [mV]	0.57	0.48	0.49	0.37

2.6 Summary

Based on the premise of using the advantage of CT identification for the estimation of model parameters, the main purposes of this chapter is to show the following contributions: (1) a fractional differential model (FDM) that has fewer estimation parameters than a physics-based electrochemical model, can be applied to accurately mimic complex input/output dynamic behavior of an electrochemistry-based system inside a Li-ion battery; (2) a continuous-time (CT) system identification approach can be used to estimate model parameters of a FDM in a Li-ion battery (LIB); (3) the use of a state-variable filter (SVF) to formulate a parameter estimation problem that is less susceptible to noise on the fractional derivatives of the input/output signals of the model; (4) the use of a standard least squares (LS) based state-variable filter (LSSVF) method for the estimation of FDM parameters; (5) the further improvement of the LS parameter estimates via an instrumental variable (IV) method to estimate parameters of the FDM.

2.7 Acknowledge

Chapter 2, in full, is a reprint of the material as it appears in the following publications.The dissertation/thesis author was the primary investigator and author of these papers.

Yunfeng Jiang, Bing Xia, Xin Zhao, Truong Nguyen, Chris Mi, Raymond A. de Callafon, "Data-based fractional differential models for non-linear dynamic modeling of a Lithium-ion battery", *Energy*, vol. 135, pp. 171-181, 2017.

Yunfeng Jiang, Bing Xia, Xin Zhao, Truong Nguyen, Chris Mi, Raymond A. de Callafon, "Identification of fractional differential models for lithium-ion polymer battery dynamics", *in the 20th World Congress of the International Federation of Automatic Control (IFAC)*, Toulouse, France, July 9-14, 2017.

Chapter 3

Power Prediction of Battery System

3.1 Introduction

Alternative battery dynamic models with low computational requirements for the BMS are highly desired to focus on dynamics of the electrochemical process of LIB. It is also very important to use a simplified dynamic model to capture battery dynamics formulated on the basis of observations from a power charge/discharge demand signal to the voltage and current signals [3]. From this point of view, a viable alternative method to model the battery system is to model the dynamic of power storage and delivery of a LIB, as indicated in Figure 3.1. In this chapter, the power storage and delivery dynamics of a battery system with an input of charge and discharge demand is modeled from control system perspective, which is different from the conventional ECM or electrochemical models. As indicated in Figure 3.1, the proposed method to predict power storage and delivery capability of a battery system is done by modeling individual dynamics from a power charge/discharge demand signal to the voltage and current signals, respectively. In particular, such a dynamic model for power storage and delivery is based on fractional derivative model, used to capture the possible infinite dimensional behavior of battery power dynamics. The proposed model approach aims to not only model how fast a battery can store and deliver energy as a function of time, but also provide the potential of controlling a battery system as BESS.

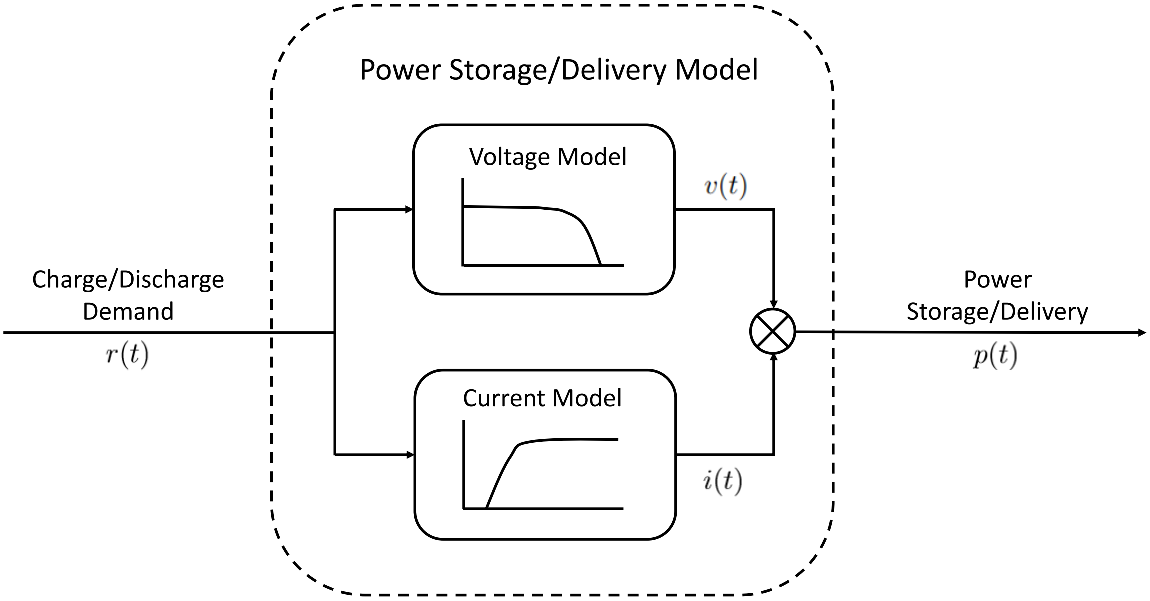

Figure 3.1. Model approach for dynamic power storage and delivery, see also [3].

3.2 Power-Based Battery Modeling

3.2.1 Experiment Setup

As shown in Figure 3.2, an experimental setup is built to test a battery as a power storage/delivery system. The charge/discharge demand signal can be applied as the input when measuring current and voltage signals of the batteries are recorded in real-time. There are three parts of the experimental setup: main circuitry, control and measurement circuitry, and computer.

In the main circuity, metal-oxide-semiconductor field-effect transistor (MOSFETs) T_1 and T_2 are used to allow the control of the power supply to LIBs. When T_1 is on and T_2 is off, the LIB is connected to the power supply. The power is transferred to charge the battery. When T_1 is off and T_2 is on, the battery is disconnected with the power supply. The power flow from the supply is switched off, thus the battery is connected to the ground and discharged. The main use of the pulse-width modulation (PWM) technique of T_1 and T_2 is to allow for modulating charge and discharge demand signals. The electric load is comprised of a parallel connection of load resistors. Such an electric load behaves to limit the current when the battery is charged, and

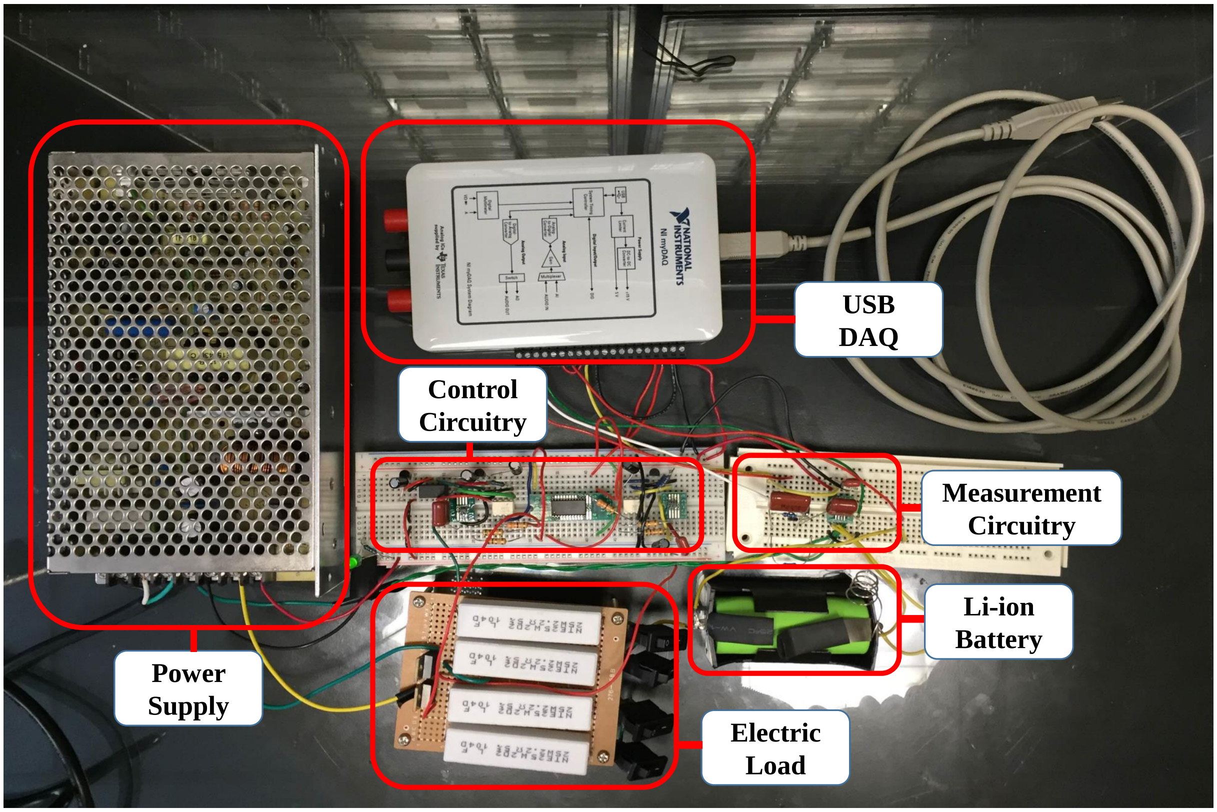

Figure 3.2. Model approach for dynamic power storage and delivery, see also [3].

performs as the load when the battery is discharged.

In the control and measurement circuitry, a National Instruments (NI) USB data acquisition (DAQ) device is used to delivery corresponding control signals to switch MOSFETs. The DAQ device is also applied to receive the measured signals and can communicate with the computer via a USB cable in real-time. A MOSFET drive is developed to boost the level of the digital output signal generated by the DAQ device. Low-order Butterworth low-pass filtering circuitry is used to reduce aliasing effects on the measured switching signals. a NI LabVIEW program was developed to automatically load cycle signals from existing files and can also save measured signals from the DAQ device. The experimental battery test can be repeated by applying the same sequence of charge/discharge demand signals.

A photograph of the experimental battery tester is shown in Figure 3.2. A 2.3 Ah-3.3 V $LiFePO_4$ battery cell ANR26650 manufactured by A123 Systems (Michigan, USA) is utilized in the experimental test. Pulse discharge at 10 s can reach 120 A and maximum continuous discharge is 70 A. Low drain-to-source on-resistance MOSFET IRLZ34 is applied to adapt in a high current flow. A bidirectional ± 20 A Hall effect sensor ACS714 is utilized to measure the current, and an analog-to-digital (A/D) conversion is used to measure the voltage over the battery.

3.2.2 Experiment Results

For experimental verification of the parameter estimation of the battery FDM, the battery is charged and discharged by a sequence of charge/discharge demand signal composed of 6th order pseudo random binary sequence (PRBS) [3]. Specifically, each PRBS is the 6th order with different scaling factors of 1, 2, and 3, respectively. As a result, different C-rates are implemented in the experiment. Each PRBS is connected with a period of zero-state, which indicated the idle status of the charge/discharge system, as shown in Figure 3.3. The measured signals of voltage and current are also shown in Figure 3.3. The experimental time is T = 90 min, and the sample rate is 10 Hz, which contains 54,000 samples.

3.2.3 Continuous-time Fractional Differential Model Identification

In order to establish a dynamic model of a Li-ion battery as a power storage/delivery system, the power charge/discharge demand signal $r(t)$ is considered as an input signal. The voltage signal $v(t)$ and current signal $i(t)$ of the battery are considered as observable output signals. As shown in Figure 3.1, the multiplication of voltage signal $v(t)$ and current signal $i(t)$ is equal to the power storage/delivery signal $p(t)$. The experimental results included below illustrate that the parameters of the two separate FDMs between $r(t)$ as input signals and $v(t)$ and $i(t)$ as output signals can be estimated very well with the LSSVF method. More details on conventional LSSVF method can be referred to last chapter, and the overall filtering and LS estimation in the LSSVF algorithm are summarized in Figure 3.4.

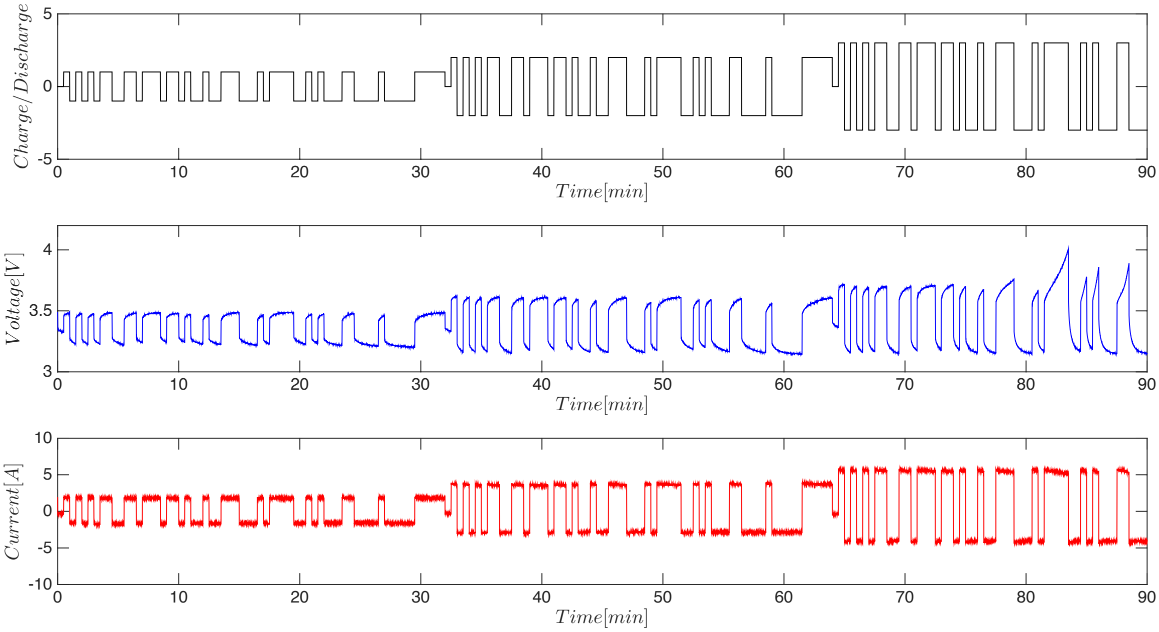

Figure 3.3. Charge/discharge cycles, voltage and current experimental results in 90 min.

3.2.4 Voltage Model

A second-order voltage FDM, with input $r(t)$ and output $v(t)$, has much better prediction performance as shown in Figure 3.5, and the simplest form to capture the voltage dynamics is estimated by the LSSVF method in the form

$$v(t) = v_n(t) + v_0 = \frac{b_2 s^{2\alpha} + b_1 s^{\alpha} + b_0}{a_2 s^{2\alpha} + a_1 s^{\alpha} + 1} r(t) + v_0 \tag{3.1}$$

where v_0 and $v_n(t)$ are offset voltage and new output voltage signals, separately. First order SVF $L(s) = \frac{1}{s+\lambda}$ is then applied to get the filtered charge/discharge demand signal $r_f(t)$ and the filtered new output voltage signal $v_{nf}(t)$. In order to estimate the parameters, the filtered prediction error of voltage model can be defined as

$$\varepsilon_{fv}(t, \theta_1) = v_{nf}(t) - \varphi_{1f}^{*}(t)^T \theta_1 \tag{3.2}$$

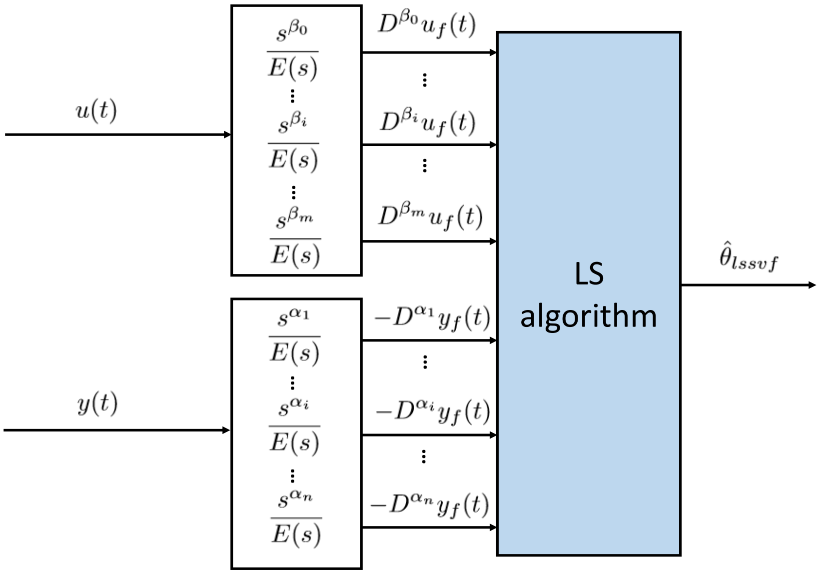

Figure 3.4. The least squares-based state-variable filter (LSSVF) estimator.

where the regression vector is given by

$$\varphi_{1f}^{*}(t)^{T} = [s^{2\alpha} r_f(t) \;\; s^{\alpha} r_f(t) \;\; r_f(t) \;\; -s^{2\alpha} v_{nf}(t) \;\; -s^{\alpha} v_{nf}(t)] \tag{3.3}$$

and the parameter vector

$$\theta_1^T = [b_2 \;\; b_1 \;\; b_0 \;\; a_2 \;\; a_1] \tag{3.4}$$

combines the unknown parameters. Subsequently, the predicted voltage

$$\hat{v}(t,\theta_1) = \hat{v}_n(t,\theta_1) + v_0 = \varphi_{1f}^{*}(t)^{T}\theta_1 + v_0 \tag{3.5}$$

is applied to estimate the performance of the model, where $\hat{v}_n(t,\theta_1)$ is the predicted new voltage. The filtered squared prediction error of voltage model given by

$$\varepsilon_{fv}^{2}(t,\theta_1) = ||v_{nf}(t) - \hat{v}_n(t,\theta_1)||_2^2 \tag{3.6}$$

is utilized to validate the accuracy of the estimation.

3.2.5 Current Model

Following the same procedure, a first-order current FDM with the input $r(t)$ and the output $i(t)$, can be estimated by the LSSVF method to capture the current dynamics of battery. The first-order current FDM is of the from

$$i(t) = \frac{d_1 s^{\alpha} + d_0}{c_1 s^{\alpha} + 1} r(t) \tag{3.7}$$

and still excellent prediction performance as shown in Figure 3.5.

After applying the same filter $L(s)$, the filtered current signal $i_f(t)$ and filtered charge and discharge demand signal $r_f(t)$ are used to minimize the L_2 norm of $\varepsilon_{fi}(t, \theta_2)$

$$\varepsilon_{fi}(t, \theta_2) = i_f(t) - \varphi_{2f}^{*}(t)^T \theta_2 \tag{3.8}$$

where the regression vector is given by

$$\varphi_{2f}^{*}(t)^T = [s^{\alpha} r_f(t) \;\; r_f(t) \;\; -s^{\alpha} i_f(t)] \tag{3.9}$$

and the parameter vector

$$\theta_2^T = [d_1 \;\; d_0 \;\; c_1] \tag{3.10}$$

combines the unknown coefficients in the first order current FDM. As in the voltage model, the filtered squared prediction error of current model is now built as

$$\varepsilon_{fi}^2(t, \theta_2) = ||i_f(t) - \hat{i}(t, \theta_2)||_2^2 \tag{3.11}$$

to verify the accuracy of the model, where $\hat{i}(t, \theta_2)$ as the predicted current output.

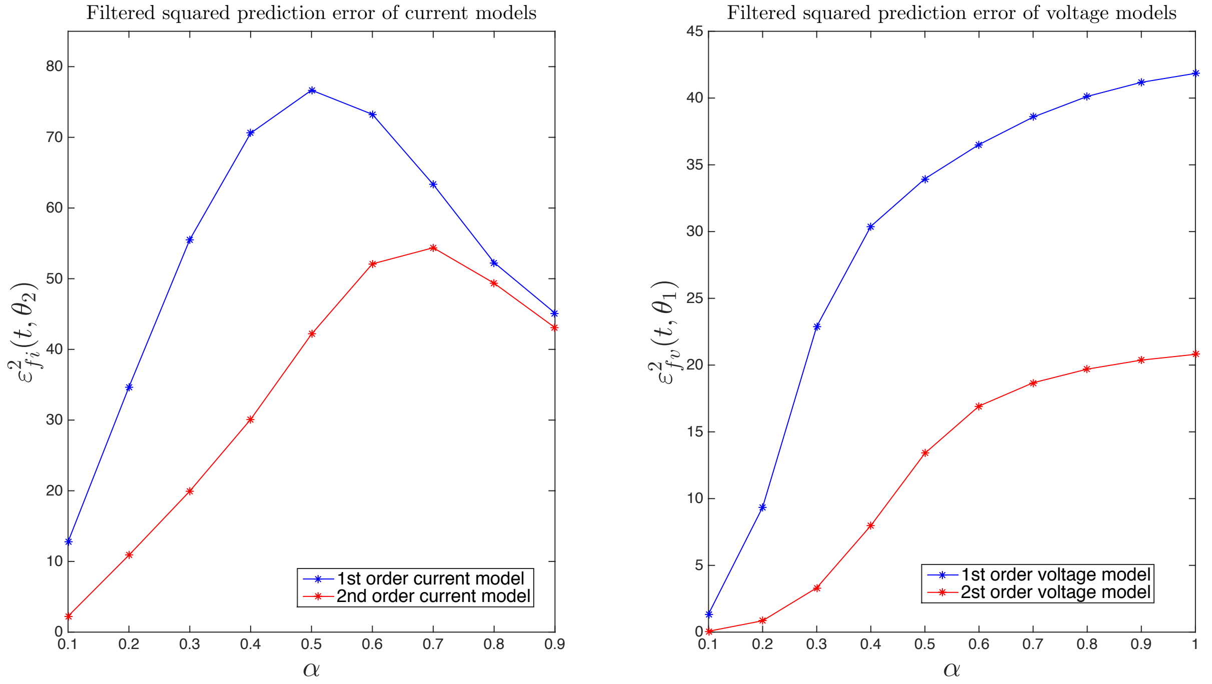

Figure 3.5. Squared prediction error of voltage model $\varepsilon^2_{fv}(t,\theta_1)$ and current model $\varepsilon^2_{fi}(t,\theta_2)$ as a function of fractional differential order α.

3.2.6 Experimental Data-Based Modeling

For identification and model validation purposes, the first 30 min of measured data and 5 Hz cut-off frequency SVF are applied to estimate the parameters and validate the models. The filtered squared prediction error of the first order and the second order voltage model ε^2_{fv}, and the current model ε^2_{fi} as a function of fractional differential order α are shown in Figure 3.5. The dependency on the fractional differential order α is used to characterize the accuracy of the models for different values of α, where a lower value along the y-axis indicates a more accurate estimation.

As can be seen in Figure 3.5, the results show that the filtered squared prediction error of a second-order voltage FDM is significantly smaller than a first-order model. This explains that the selected second-order model indeed has much better prediction performance, while still preserving the requirement of a model of the smallest complexity to capture the voltage dynamic. For the current FDM it is observed that a first order FDM suffices. Although the second-order current FDM has a slightly smaller prediction error, the first-order current FDM shows similar performance with the advantage of only having to need a first order model.

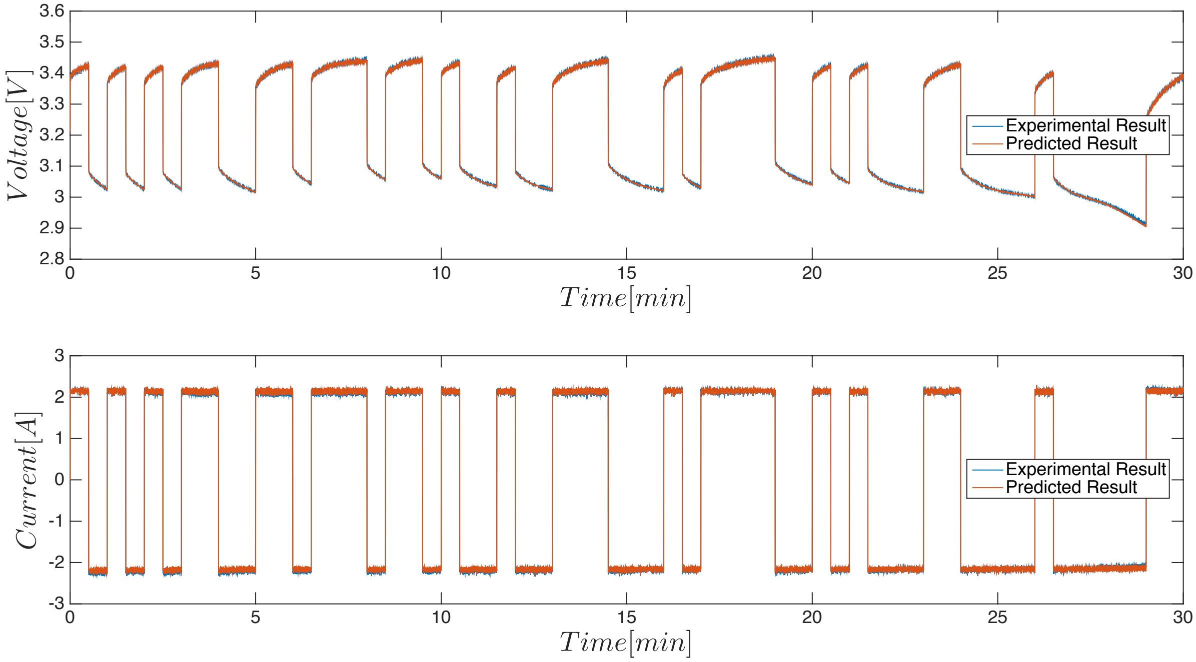

Figure 3.6. Validation results of the dynamic voltage and current models with one-step-ahead voltage and current predictors $\hat{v}(t|t-1)$ and $\hat{i}(t|t-1)$ in the first 30 min.

When the fractional differential order α is chosen as $\alpha = 0.1$ both ε_{fv}^2 and ε_{fi}^2 have the smallest value, which leads to the most accurate estimation. Therefore, the fractional differential order $\alpha = 0.1$ is chosen in the system identification via the LSSVS method for both the voltage and current FDM in Equations (3.1) and (3.7). Fixing the fractional differential order, the batch-wise estimation leads to the following voltage model and the current model, respectively given by

- Voltage Model

$$v(t) = \frac{0.2420s^{0.2} - 0.3766s^{0.1} + 0.1105}{1.7607s^{0.2} - 2.9055s^{0.1} + 1} r(t) + 3.2141 \tag{3.12}$$

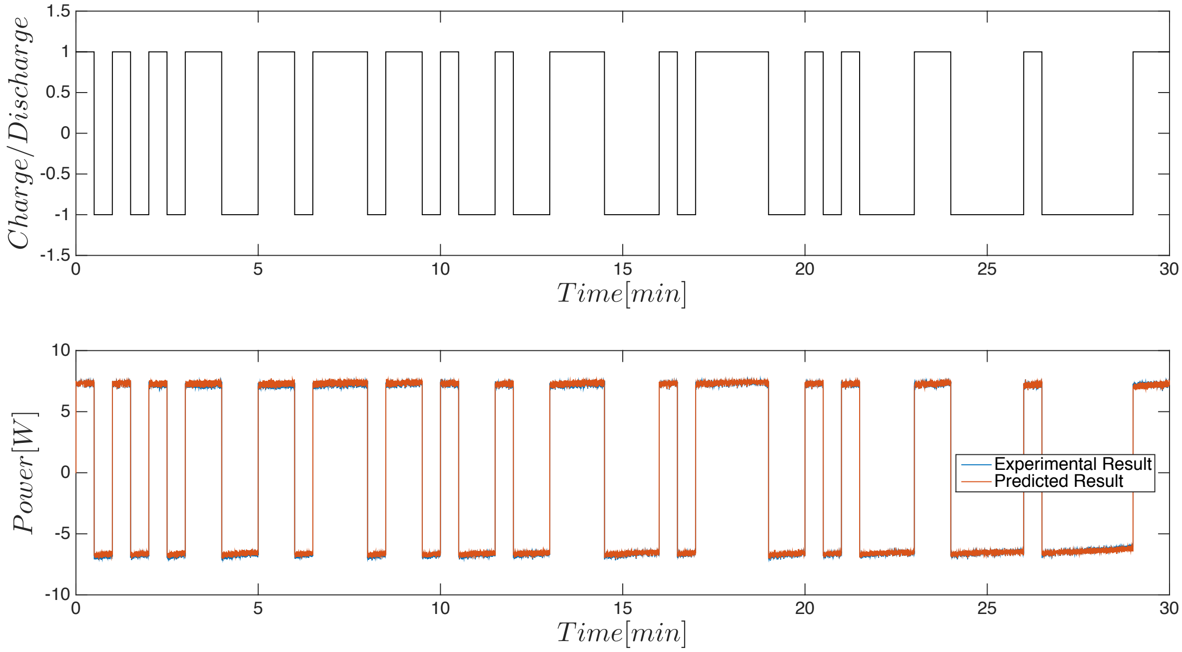

Figure 3.7. Validation results of dynamic power storage/delivery models with the one-step-ahead power predictor $\hat{p}(t|t-1)$ in the first 30 min.

- Current Model

$$i(t) = \frac{-1.7381s^{0.1} + 2.1883}{-0.7840s^{0.1} + 1} r(t) \tag{3.13}$$

The estimated voltage FDM in Equation (3.12) and the current FDM in Equation (3.13) are used to predict the voltage, current outputs and power output on the basis of measurements of the charge/discharge demand signal $r(t)$ that acts as an input to these models. Prediction of the voltage and current signals is done with the parameters of the voltage and current FDMs in Equations (3.12) and (3.13) that have been optimized for 1-step-ahead prediction. The resulting 1-step-ahead predictions are given by

$$\hat{v}(t|t-1) = \varphi_1^*(t)^T \theta_1 + v_0 \tag{3.14}$$

and

$$\hat{i}(t|t-1) = \varphi_2^*(t)^T \theta_2 \tag{3.15}$$

using the regessor vectors

$$\varphi_1^*(t)^T = [s^{0.2}r(t) \;\; s^{0.1}r(t) \;\; r(t) \;\; -s^{0.2}v_n(t) \;\; -s^{0.1}v_n(t)] \tag{3.16}$$

and

$$\varphi_2^*(t)^T = [s^{0.1}r(t) \;\; r(t) \;\; -s^{0.1}i(t)] \tag{3.17}$$

creating the 1-step-ahead power predictor by

$$\hat{p}(t|t-1) = \hat{v}(t|t-1) \cdot \hat{i}(t|t-1) \tag{3.18}$$

as a multiplication of the 1-step-ahead prediction of voltage and current.

It should be noted that the models given in Equations (3.12) and (3.13) may not be suitable for simulation, as parameters are optimized for prediction. Instead, the predictors in Equations (3.14) and (3.15) should be used for 1-step-ahead power delivery/storage prediction of the battery. As shown in Figure 3.6, the comparison of the predicted and measured results indicates that the estimated voltage and current FDMs obtained via the LSSVF method can both capture the dynamics of the voltage and current signals of the battery system. Furthermore, the proposed method is evaluated to estimate the performance of FDM identification for power storage/delivery model, which is achieved by multiplying the outputs of the individual fractional differential models. As shown in Figure 3.7, the estimation results indicate that the power storage/delivery model is able to capture the dynamics of the battery as the power storage/delivery systems.

It should be also noted that the one-step-ahead predictors using fractional differential models yield better prediction than using the same order integer models. The voltage and current prediction errors comparison between the optimized fractional models ($\alpha = 0.1$) given in Equations (3.12) and (3.13) and the integer models ($\alpha = 1$) given in Equations (3.1) and (3.7) are shown in Figure 3.8. The comparison result obtained indicates that very low relative voltage prediction errors and slight low current prediction errors of fractional models offer substantially better accuracy of prediction ability than integer models.

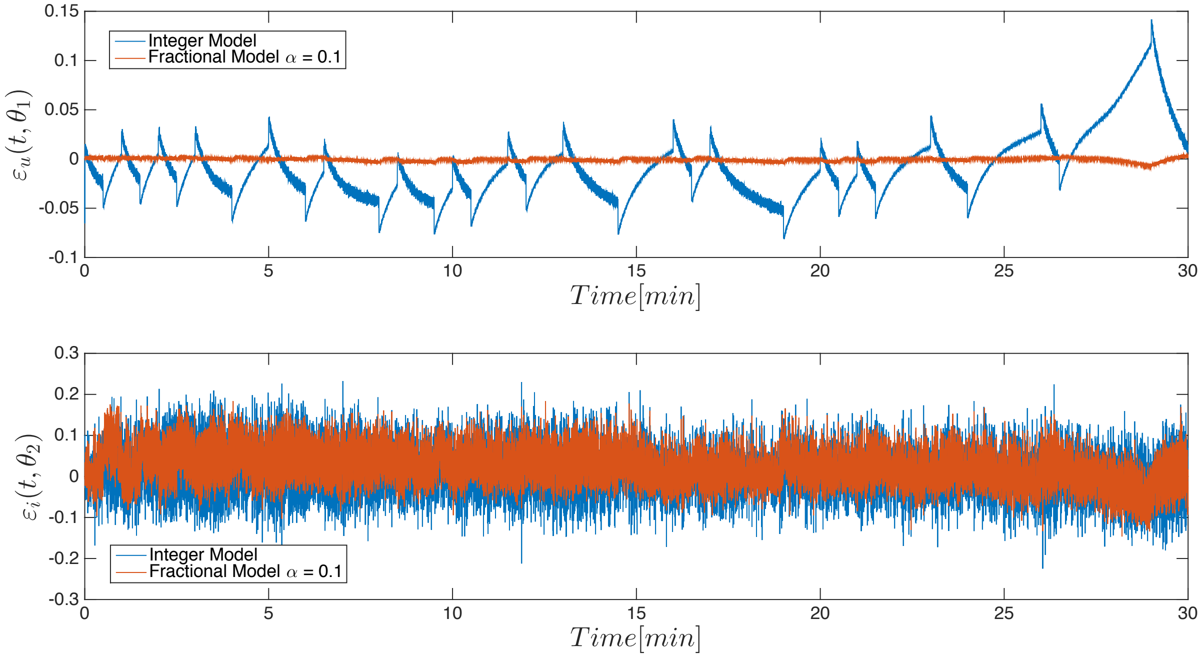

Figure 3.8. Voltage and current prediction errors $\varepsilon_v(t,\theta_1)$ and $\varepsilon_i(t,\theta_2)$ of optimized fractional models ($\alpha = 0.1$) and integer models ($\alpha = 1$) in the first 30 min.

As a final comparison of the FDM quality, a model fit ratio

$$\gamma_{x,x\in\{v,i,p\}} = (1 - \frac{\| \hat{x}(t|t-1) - x \|}{\| x - \bar{x} \|}) \tag{3.19}$$

is introduced to validate the accuracy of the model, where x, $\bar{x}$ and $\hat{x}(t|t-1)$ are output, mean value of output and one-step-ahead output predictor, respectively. Also shown in Table 3.1, the model fit ratios comparison illustrates that our proposed fractional models via the LSSVF method obtain more accurate estimation for all of the voltage models, the current model and the power storage/delivery model, assuming that fractional models are more believable than integer models.

Furthermore, the last 60 min data set is used to validate the estimated voltage model and the current model in Equations (3.1) and (3.7), respectively. The comparison of the predicted and measured results is shown in Figure 3.9. The comparison results indicate that the estimated models can also capture the dynamics of the objective system in the last 60 min and predict

Table 3.1. Model fit ratios comparison between fractional models ($\alpha = 0.1$) and integer models.

Model Fit Ratio	Fractional Model	Integer Model
Voltage Model γ_v	98.9893%	81.7168%
Current Model γ_i	97.5721%	97.1509%
Power Storage/Delivery Model γ_p	97.9440%	91.0754%

well with various C-rate charging and discharging and the wider range of SOC. As indicated in Figure 3.10, the predicted power output, which is combined by the product of the predicted voltage and current, is compared with measured power. The results validate that our proposed dynamic model can accurately predict the dynamics from the demand signal to the power storage/delivery signal of the battery for various operating situations of the battery.

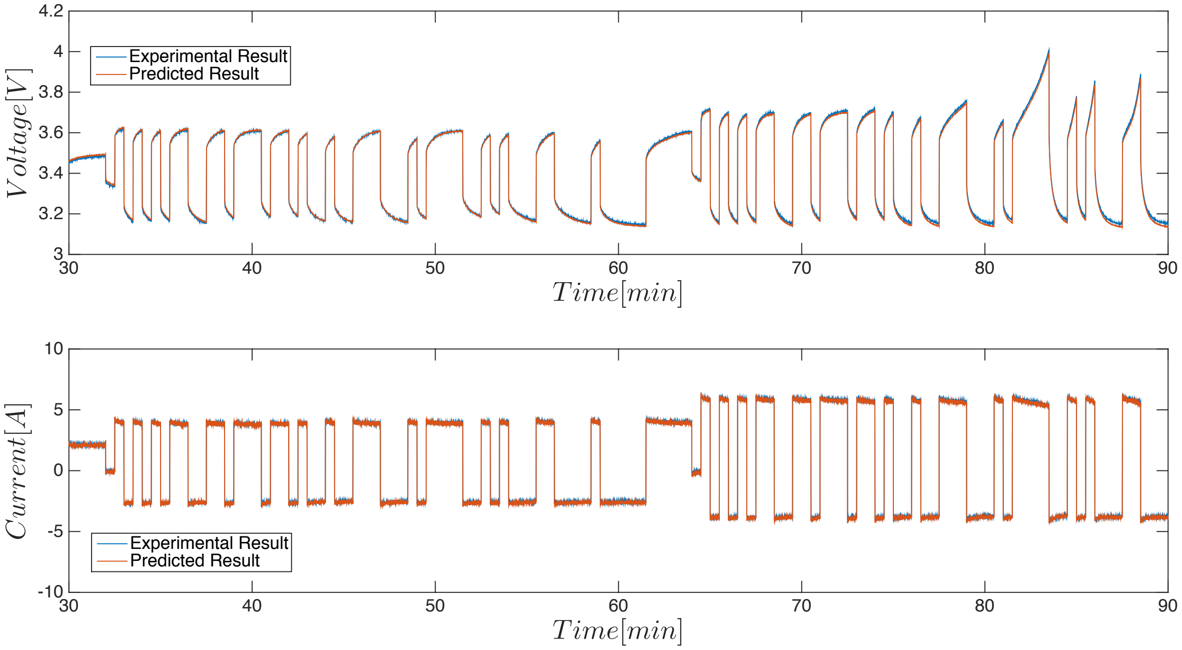

Figure 3.9. Validation results of dynamic voltage and current models with one-step-ahead voltage and current predictors $\hat{v}(t|t-1)$ and $\hat{i}(t|t-1)$ in the last 60 min.

3.3 Summary

System identification of a proposed FDM of a battery via the LSSVF method is described in this chapter. This method allows for a consistent estimation of the battery output dynamics

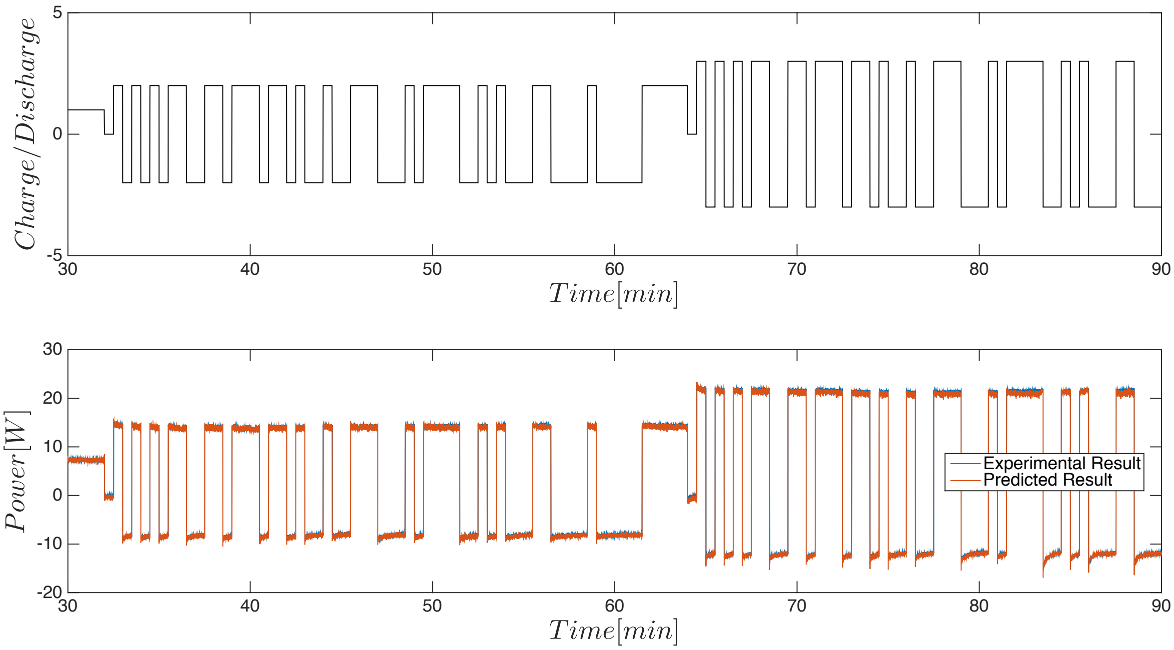

Figure 3.10. Validation results of dynamic power storage/delivery model with one-step-ahead power predictor $\hat{p}(t|t-1)$ in the last 60 min.

by fixing the value of the fractional differential order and then computing smooth fractional derivative signals of voltage and current signals to perform parameter estimation through standard LS minimization. Furthermore, an additional line search over the fractional differential order is utilized to minimize the estimation error and find the best fractional differential order. The proposed method is applied to model the dynamics from a power demand signal to the actual power storage/delivery of a $LiFePO_4$ battery cell. This is done by estimating two separate FDMs from the power demand signal to the voltage and current signals measured at the battery in real-time. Based on the experimental data set obtained from the $LiFePO_4$ battery system, comparison of predicted and measured results validates that the FDM estimated via the LSSVF method can capture the power storage/delivery dynamics over a large operation range of the battery and reveal better prediction performance than standard linear differential equation models with integer derivatives. It is anticipated that the proposed estimation method is easily implemented in a BMS to determine and predict the power delivery dynamics of a battery.

3.4 Acknowledge

Chapter 3, in part, has been submitted for publication of the material as it may appear in following published journal. The dissertation/thesis author was the primary investigator and author of this paper.

Yunfeng Jiang, Xin Zhao, Amir Valibeygi and Raymond A. de Callafon, “Dynamic prediction of power storage and delivery by data-based fractional differential models of a lithium iron phosphate battery”, *Energies*, vol.9 (8), pp. 590, 2016.

Chapter 4

Current Scheduling for a Parallel Connection of Battery Energy Storage System

4.1 Introduction

The battery pack of a BESS is built up from multiple battery cells where series connections are used to provide the BESS terminal voltage and parallel connections are used to increase storage capacity and maximum power output of the BESS. Most BESS use LIB cells connected in series, parallel or a mixture of both configuration to provide high voltage with a desired energy capacity, long life span, low self-discharge rate and fast charging capabilities [63, 64]. For the discussion and analysis presented in this dissertation, a battery module is considered to be formed by connecting a fixed number of (LIB-based) cells placed in parallel and series to satisfy a desired OCV of the individual battery module [65]. In addition, each battery module will be equipped with a current sensor and a buck regulator to allow for modulation of the terminal voltage of the battery module. The buck regulator serves as a DC-to-DC power converter controlled by pulse-width modulation (PWM) of a metal-oxide-semiconductor field-effect transistor (MOSFET) to efficiently step down terminal voltage of a battery module [66]. Finally, a full battery pack is formed by connecting multiple battery modules in parallel to a common DC-bus to increase the storage capacity and power rating of the full battery pack as a whole. The common DC-bus may be used to serve a (unknown) load such as an DC/AC inverter for grid supporting function or driving an motor in an EV application. Next to the full battery pack, a

BMS is used to monitor the SOC, module temperature, LIB cell voltages and aims to protect the BESS from operating outside its safe operating area [67].

With a BESS built from multiple parallel placed battery modules, the BESS can also be used to keep track of battery (module) parameters and perform module balancing, where the current from each module is rated according to its SOC parameter [40, 26]. Especially in a BESS with parallel placed modules where the terminal voltage of the modules can be adjusted with a buck regulator, the BMS features can be used for balancing the battery modules [68]. Balancing the battery modules will maximize the battery pack life cycle, especially when the battery pack ages and the number of total cycle increases [25]. As shown in Figure 4.1, such configuration shows the advantage of tremendously increasing feasibility, flexibility and efficiency of a swappable battery pack for EV applications, because partly empty or failing battery modules in the battery pack can be easily swapped for fast updates.

For accurate balancing of the modules, knowledge of the OCV of each module and its impedance is needed to adjust the buck regulator and ensure the current out of each module is as desired. Unfortunately, battery heterogeneity due to the manufacturing process and operating conditions is inevitable to negatively have an impact on the performance of extracting and storing the electrical energy capacity and lifespan of a battery pack. In light of heterogeneous battery pack degradation, it is necessary to develop a control and scheduling algorithm for a BMS to mitigate the impact of the possible differences between battery modules for a high power battery pack. One approach would be to operate batteries with lower internal resistances over a wider SOC range, which allows battery pack lifespan to be defined by the average battery capacity instead of the worst battery capacity [22]. An alternative approach is to assign lower SOC to smaller battery capacity, which can significantly improve capacity homogeneity and eventually extend battery pack lifespan [69]. Furthermore, a multiple objective (homogenize internal resistances, fault detection) optimization with multi-level converters (MLCs) is regarded as a suitable control approach for balancing both charge and temperature within battery packs [70, 71]. Although these algorithms are able to deal with difference in SOC and battery parameters between modules,

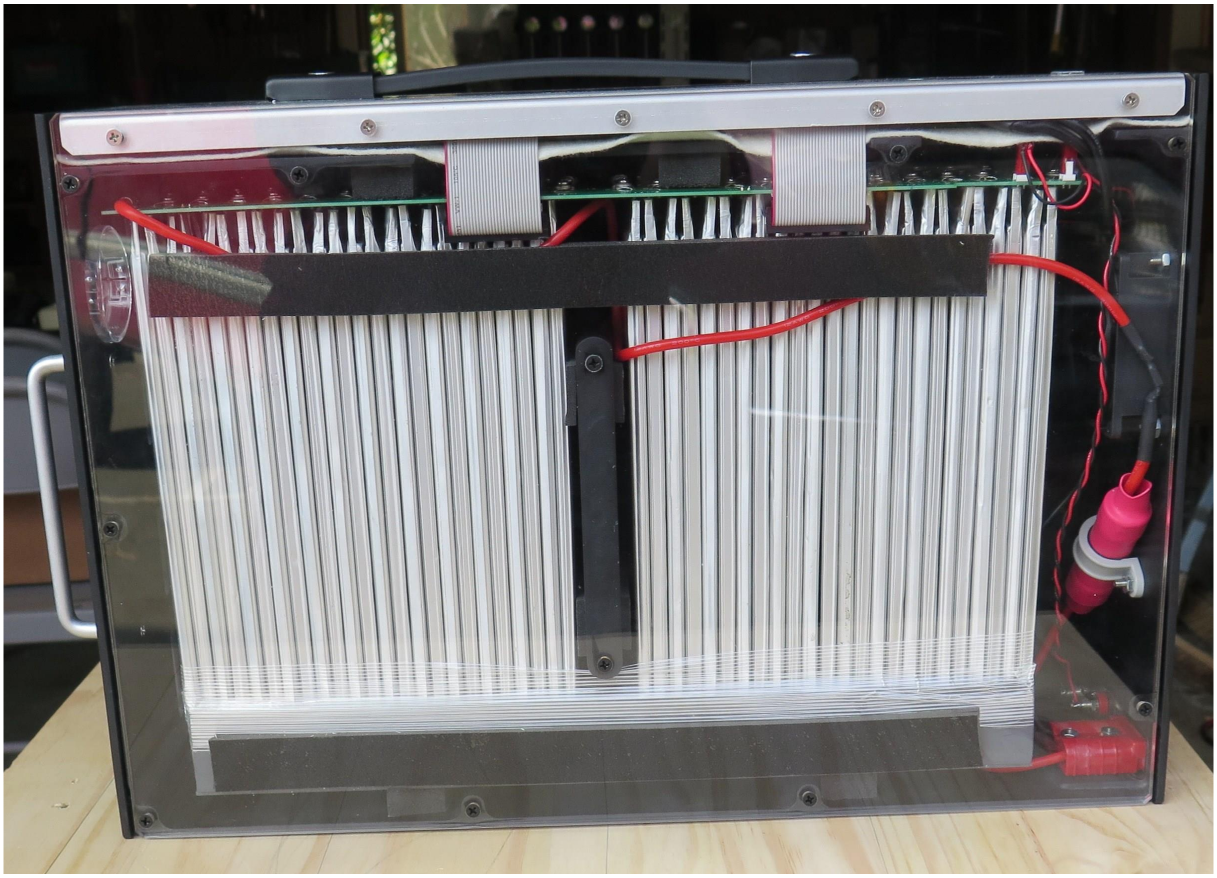

Figure 4.1. Exchangeable battery module with a series connection of LIBs in a suitcase size format. Multiple of these battery modules are connected in parallel to increase power and energy storage capabilities.

they tend to be computationally complex and require reliable high speed communication between battery modules to provide optimal scheduling.

The scheduling of multiple battery modules in a heterogeneous battery pack is solved in this chapter by finding the optimal terminal voltage of each individual module. The optimal terminal voltage is based on the requirement of balanced currents provided by the modules, whereas voltage regulation is achieved via PWM of the buck regulator in each battery module. Using centralized algorithm in open-loop system [64] as a basis, a scheduling algorithm with a decentralized architecture is developed to compute the PWM in each module. The decentralized architecture ensures that no high-speed communication is required between battery modules. Local current control in each battery module is achieved via a proportional-integral-derivative

(PID) feedback controller with a recursive scheduling algorithm. The recursive scheduling algorithm ensures that at least one of the battery modules will operate at a full or close to 100% PWM, without the explicit knowledge of the electrical module parameters such as OCV or internal impedance and despite a time-varying load connected to the battery pack. The proposed closed-loop current scheduling control technique is applied to the actual operation of experimental tester to validate the feasibility and performance in different load scenarios of a real-life battery system.

4.2 Parallel Buck Regulated Battery Modules

4.2.1 Module Formulation and Assumptions

In this chapter, current optimal scheduling of parallel placed battery modules is executed by buck regulators, which are composed of a PWM-driven MOSFET, a flyback diode and an inductor, as shown in Figure 4.2. A battery pack is formed by a set of any number of parallel-connected battery modules with buck regulated and series-connected battery cells and ultimately connect the unit to the electric load.. In each module, the battery is represented by a series connection of battery cells to create the desired OCV, while a BMS with MOSFET microcontroller controlled switch with a fly-by diode and inductor are used for regulation of the battery voltage on the parallel bus. It should be noted that module number n is arbitrary, because a battery pack can be fully or partially arranged with battery modules to deliver the desired voltage, capacity, or power density so as to significantly enhance the flexibility of the battery systems.

For the derivation of the current optimal scheduling algorithm, the battery system of parallel placed buck regulated battery modules can be simply approximated as a group of adjustable power supplies in parallel, as shown in Figure 4.3. Specifically, we assume that each battery module k with a serial of multiple cells is characterized by a modulated ideal voltage supply V_k in series with an internal impedance Z_k. For each battery module k, we presume the

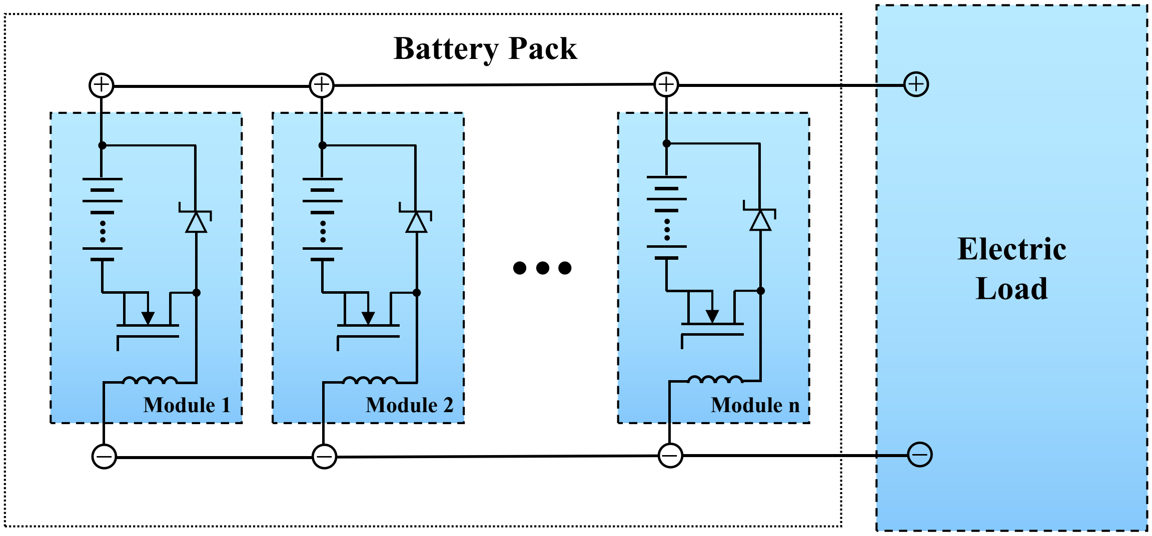

Figure 4.2. System diagram of parallel buck regulated battery modules.

following knowledge:

- The ideal voltage supply can be given by $V_k = \alpha_k V_k^{OCV}$, where OCV V_k^{OCV} is the terminal voltage of a battery module in case of no external load connected and voltage modulation coefficient $\alpha_k \in [0,1]$ represents the PWM duty cycle of MOSFET applied by a buck regulator.

- The slowly time-varying internal impedance of a battery module is given by a constant and known value Z_k in comparison with the time-varying natural of the external load impedance Z_l.

Applying Kirchoff's circuit laws now yields to the following relationships for above mentioned battery system shown in Figure 4.3:

- The algebraic sum of current I_k of each battery module is equal to bus current

$$I_{bus} = \sum_{k=1}^{n} I_k \tag{4.1}$$

due to Kirchhoff's current law (KCL).

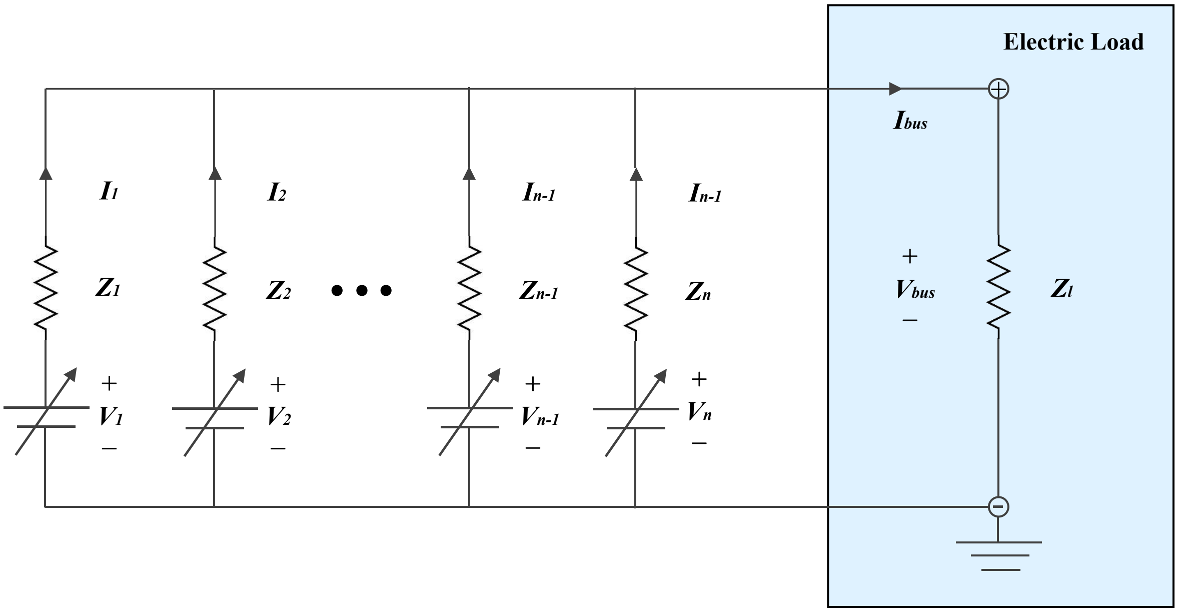

Figure 4.3. Model for current scheduling.

- Similar to KCL, the bus voltage V_{bus} can be satisfied

$$V_{bus} = V_k - Z_k I_k \tag{4.2}$$

for each battery module k due to Kirchhoff's voltage law (KVL).

4.2.2 The Formulation of Module Voltages and Module Currents

The above fundamental equalities Eq. (4.1) and Eq. (4.2) of the battery system can be combined to compute bus current I_{bus} and bus voltage V_{bus} when a load with impedance value Z_l is applied to connect battery back with parallel placed battery modules. With the knowledge of a given set of values for modulated voltages $V_k,\ k = 1,2,\ldots,n$, individual module current I_k can be determined by

$$I_k = \frac{V_k - V_{bus}}{Z_k} \tag{4.3}$$

Recalling that the bus current I_{bus} can be derived from individual module current I_k from relationship Eq. (4.1), we can solve bus voltage V_{bus} via

$$V_{bus} = Z_L I_{bus} = Z_L \sum_{k=1}^{n} I_k = Z_L \sum_{k=1}^{n} \frac{V_k - V_{bus}}{Z_k}$$

This allows us to recreate V_{bus}

$$V_{bus} = Z_L \sum_{k=1}^{n} \frac{V_k}{Z_k} - V_{bus} Z_L \sum_{k=1}^{n} \frac{1}{Z_k}$$

which is equivalent to

$$V_{bus} = \frac{\displaystyle\sum_{k=1}^{n} \frac{V_k}{Z_k}}{\displaystyle\frac{1}{Z_l} + \sum_{k=1}^{n} \frac{1}{Z_k}}$$

From last expression, the bus voltage V_{bus} can be computed by the linear combination

$$\begin{aligned} V_{bus} &= g_1 V_1 + g_2 V_2 + \ldots g_n V_n \quad \text{where} \\ g_j &= \frac{\displaystyle\frac{1}{Z_j}}{\displaystyle\frac{1}{Z_l} + \sum_{k=1}^{n} \frac{1}{Z_k}}, \quad j = 1, 2, \ldots, n \end{aligned} \tag{4.4}$$

where the "gain factors" $g_k,\ k = 1, 2, \ldots, n$ are given by a combination of impedances Z_k and Z_l from parallel placed battery modules.

4.2.3 Currents Matrix

With the individual module currents I_k given in Eq. (4.3) and bus voltage V_{bus} given in Eq. (4.4), we can then obtain I_k as a typical linear combination of all modulated module voltages V_k:

$$I_k = \frac{1}{Z_k} \left(V_k - \frac{\displaystyle\sum_{m=1}^{n} \frac{V_m}{Z_m}}{\displaystyle\frac{1}{Z_l} + \sum_{m=1}^{n} \frac{1}{Z_m}} \right) = \frac{1}{Z_k} \left(\frac{\displaystyle\frac{V_k}{Z_l} + \sum_{m=1}^{n} \frac{V_k}{Z_m} - \sum_{m=1}^{n} \frac{V_m}{Z_m}}{\displaystyle\frac{1}{Z_l} + \sum_{m=1}^{n} \frac{1}{Z_m}} \right)$$

where the summation index has been changed to m in order to avoid confusion with the specific module current I_k indexed with k. The above expression for I_k can be simplified as an insightful linear combination expression

$$\begin{aligned} I_k &= d_{k,1}V_1 + d_{k,2}V_2 + \ldots + d_{k,n}V_n, \quad \text{where} \\ d_{k,j} &= \begin{cases} -\dfrac{1}{Z_k} \cdot \dfrac{\dfrac{1}{Z_j}}{\dfrac{1}{Z_l} + \displaystyle\sum_{m=1}^{n} \dfrac{1}{Z_m}} & \text{for } j \neq k \\ \dfrac{1}{Z_k} \cdot \dfrac{\dfrac{1}{Z_l} + \displaystyle\sum_{m=1}^{n} \dfrac{1}{Z_m} - \dfrac{1}{Z_k}}{\dfrac{1}{Z_l} + \displaystyle\sum_{m=1}^{n} \dfrac{1}{Z_m}} & \text{for } j = k \end{cases} \end{aligned} \tag{4.5}$$

The coefficients $d_{k,j}$, $k = 1,2,\ldots,n$ and $j = 1,2,\ldots,n$ can build up a $n \times n$ impedance matrix $D = [d_{k,j}]$, which relates module currents I_k to module voltage V_k given by

$$\begin{bmatrix} I_1 \\ I_2 \\ \vdots \\ I_n \end{bmatrix} = \begin{bmatrix} d_{1,1} & d_{1,2} & \cdots & d_{1,n} \\ d_{2,1} & d_{2,2} & \cdots & d_{2,n} \\ \vdots & \vdots & \cdots & \vdots \\ d_{n,1} & d_{n,2} & \cdots & d_{n,n} \end{bmatrix} \begin{bmatrix} V_1 \\ V_2 \\ \vdots \\ V_n \end{bmatrix}, \quad \text{with } d_{k,j} \text{ given in (4.5)} \tag{4.6}$$

The impedance matrix $D = [d_{k,j}]$ will be very useful for the explicit computation of module currents I_k as a function of the module voltages V_k and visa versa. It can be easily observed from the definition of the impedance matrix $D = [d_{k,j}]$ that with all impedance values positive, D is also positive definite and symmetric, making D nonsingular. With D invertible, module voltages V_k can be computed as a function of desired module currents I_k for the parallel placed battery modules.

4.3 Open-loop Optimal Current Scheduling

4.3.1 Relative Scaling of Module Currents

Given the knowledge of impedance matrix $D = [d_{k,j}]$ with internal impedances Z_k and a fixed (but unknown) load impedance Z_l, optimal current scheduling problem can be formulated as to compute the buck regulated module voltages $V_k \leq V_k^{OCV}$, such that module currents I_k can be scaled to satisfy

$$I = \begin{bmatrix} I_1 \\ I_2 \\ \vdots \\ I_n \end{bmatrix} = \beta \begin{bmatrix} \beta_1 \\ \beta_2 \\ \vdots \\ \beta_n \end{bmatrix}, \ 0 \leq \beta_k \leq 1, \ k = 1, 2, \ldots, n \tag{4.7}$$

where the coefficients β is used for absolute scaling and $0 \leq \beta_k \leq 1$ specifies the relative scaling of the module current I_k. It should be noted that the β value represents $\beta > 0$ for battery module discharging, whereas $\beta < 0$ for battery charging. A recursive solution will be formulated to accomplish module current scheduling despite the lack of knowledge on the internal module impedance Z_k and the external load impedance Z_l (fixed and time-varying). The relative scaling β_k of the module currents I is determined by charging/discharging current I_k in/out of module k based on individual SOC of each battery module, defined as

$$\beta_k = \frac{\min_{k=1,2,\ldots,n} SOC_k}{SOC_k} \leq 1 \ \ \text{(charging status)}$$

and

$$\beta_k = \frac{SOC_k}{\max_{k=1,2,\ldots,n} SOC_k} \leq 1 \ \ \text{(discharging status)}$$

where SOC_k of module k is satisfied by $0\% \leq SOC_k \leq 100\%$ $(0\% = \text{empty}; 100\% = \text{full})$. The above β_k expressions can guarantee that battery modules with smaller SOC will charge faster with larger current compared to battery modules with a larger SOC, and also battery modules with a smaller SOC will discharge less current compared to battery modules with a larger SOC.

In case where all modules have same storage capacity and same SOC, and can be required to follow the same charging/discharging profile, the relative scaling β_k of the module currents I given by Eq. (4.7) can be satisfied to be identical $\beta_k = 1,\ k = 1, 2, \ldots, n$, making

$$I_1 = I_2 = \cdots = I_n \tag{4.8}$$

and will be denoted by equal SOC current scheduling and specifically verified in this paper.

4.3.2 Module Current Scheduling via Linear Programming

Given the full information of the invertible impedance matrix D with each internal impedance Z_k and external load impedance Z_l in Eq. (4.6), we can explicitly compute the set of optimal modulated module voltages $V = [V_1\ V_2\ \cdots\ V_n]^T$ from a desired set of module currents $I = [I_1\ I_2\ \cdots\ I_n]^T$. Using vector notation

$$V = \begin{bmatrix} V_1 \\ V_2 \\ \vdots \\ V_n \end{bmatrix},\ V^{OCV} = \begin{bmatrix} V_1^{OCV} \\ V_2^{OCV} \\ \vdots \\ V_n^{OCV} \end{bmatrix}$$

for module voltages, vector format I in Eq. (4.7) for module currents, and invertible impedance matrix D in Eq. (4.6), the optimal current scheduling can be written as a typical linear programming (LP) problem that requires to compute the maximum value of the current absolute scaling $\beta \geq 0$ (for discharging) such that $V \leq V^{OCV}$. By rewriting that

$$V = D^{-1} \begin{bmatrix} \beta_1 \\ \beta_2 \\ \vdots \\ \beta_n \end{bmatrix} \beta$$

from Eq. (4.6) and the optimization for absolute scaling β of module currents can be expressed in standard form as

$$\max_{\beta} \beta$$
$$\text{s.t. } D^{-1} \begin{bmatrix} \beta_1 & \beta_2 & \cdots & \beta_n \end{bmatrix}^T \beta \leq V^{OCV}$$

which is equivalent to a LP problem for numerical computation (MATLAB)

$$\begin{gathered} \beta_{opt} = \min_{\beta} f^T \beta, \text{ s.t. } A\beta \leq b, \text{ with} \\ A = D^{-1} \begin{bmatrix} \beta_1 & \beta_2 & \cdots & \beta_n \end{bmatrix}^T, \\ f^T = -1, \text{ and } b = V^{OCV} \end{gathered} \tag{4.9}$$

The LP formulation in Eq. (4.9) provides the numerical tool to compute the optimal solution that can maximize module current I by finding the maximize value β, given the constrains on V_{OCV} for each module. Once the optimal absolute scaling β_{opt} is obtained, both optimal module currents and voltages can be explicitly computed via

$$I_{opt} = \beta_{opt} \begin{bmatrix} \beta_1 & \beta_2 & \cdots & \beta_n \end{bmatrix}^T \tag{4.10}$$

and

$$V_{opt} = \beta_{opt} D \begin{bmatrix} \beta_1 & \beta_2 & \cdots & \beta_n \end{bmatrix}^T \tag{4.11}$$

4.3.3 Centralized Recursive Optimal Current Scheduling

The LP solution given in Eq. (4.9) to compute the optimal value β_{opt} requires full knowledge of the impedance matrix D in Eq. (4.6) with internal module impedances Z_k and external load impedance Z_l. It should be further noted that the internal module impedances Z_k may be monitored by battery management system (BMS) and slowly increase over time, however, the external load Z_l may be not known and has the fast time-varying feature due to changing power demands in different scenario profiles. Therefore, the module current optimal scheduling in Eq. (4.6) must be allowed to compute in a recursive way with the knowledge of internal impedance Z_k (fixed value) for each module but without further explicit knowledge of the external load Z_l.

In recursive module current scheduling, we will update the impedance matrix D recursively to allow for the computation of the optimal modulated module voltages V_k, where the value of external load impedance $Z_l = \frac{V_{bus}}{I_{bus}}$ can be estimated by monitoring the bus voltage V_{bus} and the bus current I_{bus} by using Ohm's law. Therefore, based on the fact that the value of Z_l can be estimated and replaced in the impedance matrix D by the ratio of V_{bus} and I_{bus}, a straightforward recursive approach is used to recursively update D in order to determine optimal values of the internal module voltages V_{opt} for optimal scheduling module currents I_{opt}. Starting from an initial choice for the module voltages $V = [V_1\ V_2\ \cdots\ V_n]^T$, the estimated load impedance Z_l obtained from measured bus voltage V_{bus} and bus current I_{bus} can be used to update impedance matrix D and further applied to compute the optimal current scaling β_{opt}. The optimal module voltages V_{opt} can then be obtained from relationship Eq. (4.11) and used to communicate each module in a centralized approach. This centralized recursive optimal current scheduling approach can be implemented recursively in time and summarized as below specific procedure in discrete-time (DT) system.

Centralized current scheduling procedure:

1. Assume fixed internal impedances $Z_k,\ k = 1,2,\ldots,n$ but a time-varying load impedance Z_l.

2. Set initial time index $t = 0$ and communicate the n elements $V_k[0]$ of the initial module voltages $V[0] = [V_1[0]\ V_2[0]\ \cdots\ V_n[0]]^T$ to each of the corresponding modules $k = 1,2,\ldots,n$.

3. At time index t, conduct a measurement of $V_{bus}[t]$ and $I_{bus}[t]$ and compute the external load impedance by
$$Z_l[t] = \frac{V_{bus}[t]}{I_{bus}[t]}$$

and then update the impedance matrix $D[t]$ in (4.6).

4. Before the subsequent time step $t+1$, find $\beta_{opt}[t]$ by the LP problem in (4.9) using the updated impedance matrix $D[t]$ and compute the module voltages $V_{opt}[t+1]$ according to

$$V_{opt}[t+1] = \beta_{opt}[t]D[t]\begin{bmatrix} \beta_1 & \beta_2 & \cdots & \beta_n \end{bmatrix}^T$$

5. At time step $t+1$, communicate each of the modules $k = 1,2,\ldots,n$ and update the module voltage V_k to $V_k = V_k[t+1]$ of the $V_{opt}[t+1] = [V_1[t+1]\ V_2[t+1]\ \cdots\ V_n[t+1]]^T$

6. Increment time index $t = t+1$ and restart from step 1.

It should be noted that the recursive updates of optimal module voltages $V_{opt}[t]$ from above procedure can converge in a single time step in case of fixed value of Z_l at time step t. In order to track fast time-varying of external load Z_l due to power demand change, the above procedure should allow high-frequency measurements and communication of bus voltage V_{bus} and bus current I_{bus}. In addition, the above centralized implementation of recursive module current scheduling can be solved by LP problem in Eq. (4.9), where each module $k = 1,2,\ldots,n$ simply only receives its $V_k[t+1]$ from the centrally computed optimal LP solution $V_{opt}[t+1] = [V_1[t+1]\ V_2[t+1]\ \cdots\ V_n[t+1]]^T$ in step 4 and 5.

4.3.4 Decentralized Recursive Optimal Current Scheduling

Although the LP problem in Eq. (4.9) can be computed with fast computing hardware, measurements and communication of a large bus voltage V_{bus} and a high bus current I_{bus} may require dedicated hardware and optical isolation devices. Furthermore, when the number n of modules becomes large, the communication to update of $V_{opt}[m+1]$ puts additional requirements on the speed and reliability of the communication hardware, and the ability to respond to the information request in a timely manner gets reduced. In this paper, we will propose a solution that replaces the measurements of V_{bus} and I_{bus} and reduce the centralized communication requirements by a decentralized recursive module current scheduling. In order to explain clearly the decentralized recursive module current scheduling, first it should be noted that the measurement of V_{bus} and I_{bus} can be replaced by the measurement of a single module current I_k performed by any module m. From KVL in Eq. (4.2), the measurement of V_{bus} can be replaced by a measurement of a module current I_m and computed by $V_{bus} = V_m - Z_m I_m$. As a matter of fact that the individual module current I_m is much smaller than the bus current I_{bus}, the measurement of the individual module current I_m can be easily realized by implemented BMS of that module m. Second, it should be also noted that once bus voltage V_{bus} is known, all the module currents $I_k,\ k = 1, 2, \ldots, n$ can now be computed as the following expression

$$I_k = \frac{V_k - V_{bus}}{Z_k}, \text{ where } V_{bus} = V_m - Z_m I_m \tag{4.12}$$

allowing to recreate bus current I_{bus} via

$$I_{bus} = \sum_{k=1}^{n} I_k = \sum_{k=1}^{n} \frac{V_k - V_{bus}}{Z_k}, \text{ where } V_{bus} = V_m - Z_m I_m \tag{4.13}$$

With both bus voltage V_{bus} and bus current I_{bus} now obtained from above expression, the same load impedance estimate as centralized scheduling can be rewritten as

$$Z_l = \frac{V_{bus}}{I_{bus}} = \frac{V_{bus}}{\sum_{k=1}^{n} \frac{V_k - V_{bus}}{Z_k}}, \text{ where } V_{bus} = V_m - Z_m I_m \tag{4.14}$$

which allows to update the impedance matrix D the computation of the optimal module voltages V_{opt} via the LP problem of Eq. (4.9).

In view of a decentralized solution as opposed to centralized solution in last section, it can be clearly observed that the measurement of the current I_m of module m and the computation of the bus voltage V_{bus} in (4.14) can be done within any module m without any communication requirements. Furthermore, if each and every module m holds the knowledge on all the initial module voltages $V_k,\ k=1,2,\ldots,n$ and the internal impedances $Z_k,\ k=1,2,\ldots,n$, the bus current I_{bus} in Eq. (4.13) can be computed and the information on all the optimal module voltages $V_k,\ k=1,2,\ldots,n$ can be solved by the same LP problem of Eq. (4.9) and maintained in each and every module m. In this way, each module m computes its own optimal voltage V_m and keeps track of the optimal voltages V_k of the other modules, which eliminates the need for high speed central communication of the individual module voltages $V_k,\ k=1,2,\ldots,n$ to each of the modules. The only communication that would have to take place typically at a much smaller rate is the updates on the possibly slowly changing internal impedances Z_k and SOC_k of each module $k=1,2,\ldots,n$. Similar to the centralized recursive solution, the ideas on the locally decentralized computation of the bus voltage V_{bus} and the bus current I_{bus} by solving the LP problem in Eq. (4.9) can be implemented recursively in time and summarized in the following procedure.

Decentralized current scheduling procedure:

1. Assume fixed internal impedances $Z_k,\ k=1,2,\ldots,n$ but a time-varying load impedance Z_l.

2. Set initial time index $t=0$ and communicate the n elements $V_k[0]$ of the initial module voltages $V[0]=[V_1[0]\ V_2[0]\ \cdots\ V_n[0]]^T$ to each of the corresponding modules $k=1,2,\ldots,n$.

3. At time index t, each individual module m measures the module current $I_m[t]$ and compute the bus voltage

$$V_{bus}[t]=V_m[t]-Z_mI_m[t]$$

the bus current

$$I_{bus}[t]=\sum_{k=1}^{n}\frac{V_k[t]-V_{bus}[t]}{Z_k},\ \ V_{bus}[t]=V_m[t]-Z_mI_m[t]$$

and further update the impedance matrix $D[t]$ in (4.6) with full information of internal impedance Z_k and estimated load impedance $Z_l[t] = \frac{V_{bus}[t]}{I_{bus}[t]}$.

4. Before the subsequent time step $t+1$, each individual module updates the optimal module voltages $V_{opt}[t+1] = [V_1[t+1]\ V_2[t+1]\ \cdots\ V_n[t+1]]^T$ according to

$$V_{opt}[t+1] = \beta_{opt}[t]D[t]\left[\begin{array}{cccc} \beta_1 & \beta_2 & \cdots & \beta_n \end{array}\right]^T$$

where $\beta_{opt}[t]$ is obtained by the LP problem in (4.9) solved in each module.

5. At time step $t+1$, each module m updates the module voltage V_k to $V_k = V_k[t+1]$ of the $V_{opt}[t+1] = [V_1[t+1]\ V_2[t+1]\ \cdots\ V_n[t+1]]^T$

6. Increment time index $t = t+1$ and restart from step 1.

It should be noted that the recursive updates of optimal module voltages $V_{opt}[t]$ explained above again is able to converge in a single time step in case Z_l is fixed at time step t. Due to the decentralized nature of measuring module current and solving the same LP problem within each individual module, additional communication requirement of measurement and optimal computation of module voltage V_k is not necessary, which can allow a large battery pack of multiple modules n to track time-varying load demands with little communication traffic. For robustness and time drift avoiding, only temporary communication of internal impedance Z_k and timing clock for synchronous updates of $V_m = V_m[t+1]$ at time index $t+1$ are required.

4.3.5 Numerical Illustration of Recursive Equal SOC Current Scheduling

To illustrate the recursive updates of the internal module voltages for equal SOC current scheduling, we consider a numerical example of $n = 3$ parallel placed battery modules with full scale module OCVs of

$$V_1^{OCV} = 48V,\ \ V_1^{OCV} = 49V \ \text{ and } \ V_3^{OCV} = 50V \tag{4.15}$$

For illustration of the sensitivity of the open-loop scheduling with respect to knowledge of the internal impedance of the battery modules, two different scenarios are considered. The first scenario assumes an unknown time-varying load, but perfect knowledge of the internal impedance. In the second scenario, the internal impedance of the battery modules is assumed to be incorrect.

Before demonstrating the numerical results, it is worthwhile to show the need for current scheduling of battery modules with different internal impedance values. Assuming internal impedance values

$$Z_1 = 4\Omega,\ \ Z_2 = 3\Omega \ \text{ and } \ Z_3 = 2\Omega \tag{4.16}$$

and a time-varying load, the current of the individual battery modules when the PWM$_k$ for each module k is simply fixed to 100% is illustrated in Figure 4.4. It can be seen that due to the varying load (bottom of figure) that the current I_k produced by each module varies significantly and there may be stray current between modules due to the difference in OCV between the modules.

Unknown, time-varying external load

To illustrate the recursive updates of the internal module voltages for equal SOC current scheduling, we consider the known internal impedance values given in Eq. (4.16) and again subjected to a time-varying external load impedance $Z_l[t]$ over a DT index t, as shown in the bottom figure of Figure 4.5. To adjust module voltages of

$$V = \begin{bmatrix} V_1 \\ V_2 \\ V_3 \end{bmatrix} = \begin{bmatrix} \alpha_1 V_1^{OCV} \\ \alpha_2 V_2^{OCV} \\ \alpha_3 V_3^{OCV} \end{bmatrix} \tag{4.17}$$

with the PWM modulation factor $\alpha_1,\ \alpha_2$ and α_3, the decentralized iteration steps outlined in above section is followed to maintain balanced (equal) module currents. The numerical results for

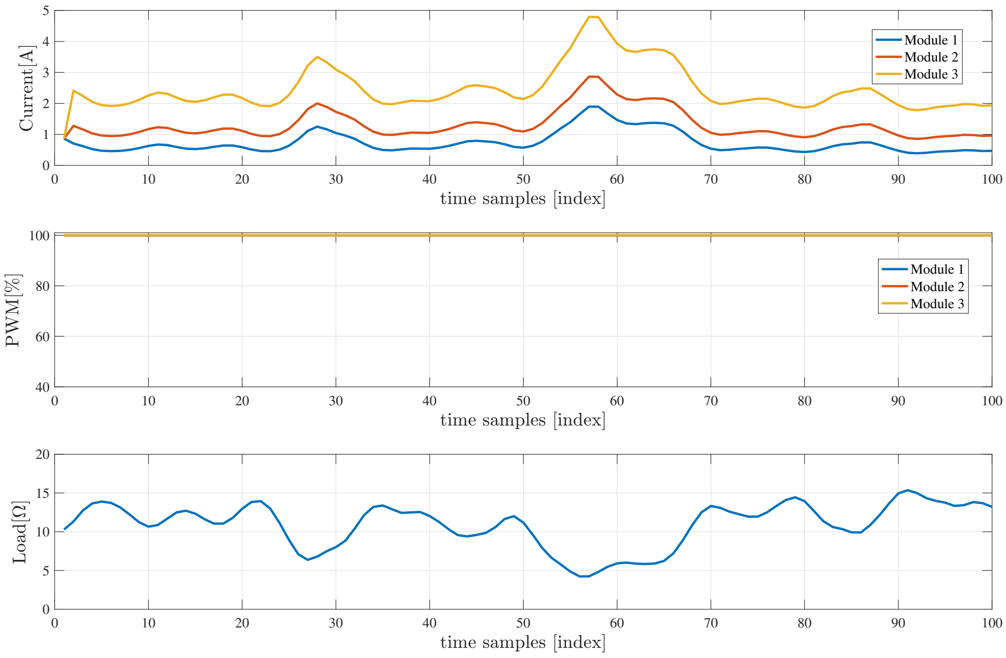

Figure 4.4. Currents in battery modules (top) and PWM modulation (all 100%) of battery voltage (middle) without recursive SOC balanced module scheduling of 3 parallel placed battery modules with accurate estimated internal impedance, subjected to a time-varying external load (bottom).

recursive time-varying balanced (equal) current scheduling is summarized in Figure 4.5, where it can be seen in top figure that the individual module currents stay relatively close (balanced), despite the presence of a time-varying external load. This is clearly an improvement over the results in Figure. 4.4 when no current balancing is used under same time-varying load scenario.

It should be noted that we initialized the internal module voltages $V_{opt}[0] = V_{opt}$ based on the assumption of external load impedance $Z_l[1] = 10\Omega$ at the initial time step $t = 0$. The balanced (equal) module currents are caused by the time-varying updates of the module voltages $V_k[t]$ via PWM modulation factor $\alpha_k[t]$, $k = 1,2,3$ in a proportional relationship. The time-varying nature of the modulation factor $\alpha_k[t]$, $k = 1,2,3$ of 3 modules is plotted in middle figure of Figure 4.5, where module 1 is always set at a full modulation of 100% motivated intuitively by its highest internal impedance $Z_3 = 4\Omega$ and its lowest OCV $V_3^{OCV} = 48V$ compared with other

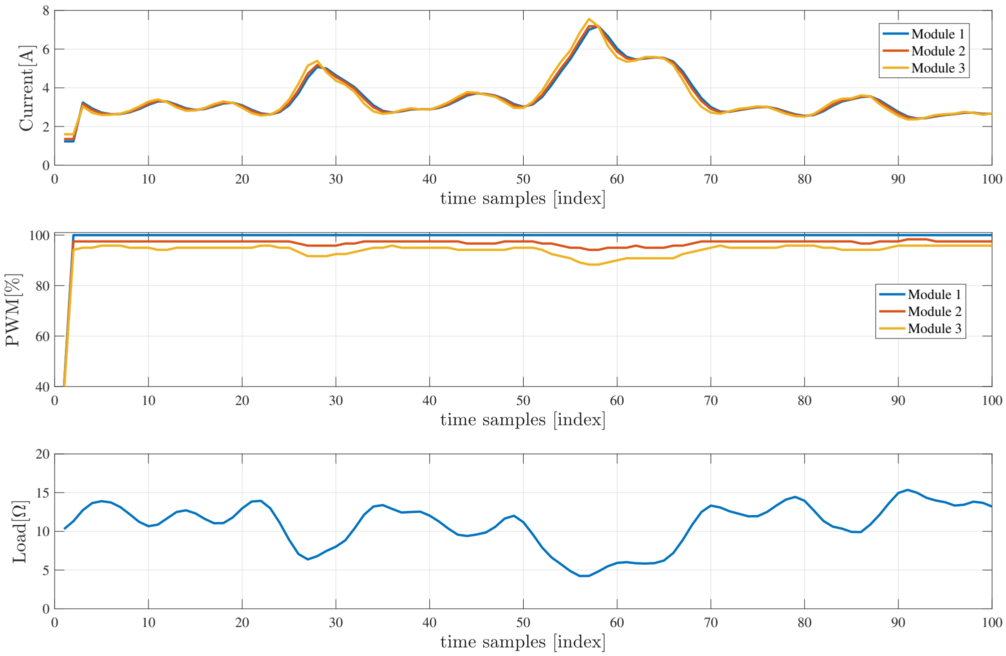

Figure 4.5. Currents in battery modules (top) and PWM modulation of battery voltage (middle) for recursive SOC balanced module scheduling of 3 parallel placed battery modules with accurate estimated internal impedance, subjected to a time-varying external load (bottom).

modules, which allows to modulate down (less than 100%) the other modules currents I_k to be balanced (equal).

Effects of inaccurate internal impedance

The above numerical example illustrates the recursive equal SOC current scheduling for $n = 3$ parallel placed battery modules with accurate estimated and fixed internal impedance $Z_k,\ k = 1,2,3$, subjected to a time-varying external load impedance $Z_l[t]$. In fact, the estimated internal impedance Z_k can be quite uncertain and the measurement from BMS may not be accurate because cable and parasitic resistance values should be also considered as part of internal resistance value. Therefore, the computation precision of the optimal value β_{opt} will be heavily impacted due to recursive updates of impedance matrix D without accurate estimated internal impedance value Z_k, which finally makes extremely difficult to find precisely optimal modulated voltages V_k and PWM modulation factor β_k for each module to realize current scheduling purpose.

For illustrative purposes, we revisit the previous numerical example of $n = 3$ parallel placed battery modules with the OCV values given in Eq. (4.15), the internal impedance values in Eq. (4.16) used for LP program computation but slightly different true values

$$Z_1^{real} = 4.2\Omega,\ \ Z_2^{real} = 2.8\Omega \ \text{ and } \ Z_3^{real} = 2.2\Omega \tag{4.18}$$

subjected to the same time-varying external load impedance $Z_l[t]$ shown in bottom figure of Figure 4.5. Before showing the results, it should be noted that the internal impedance values in Eq. (4.16) are used to recursively update impedance matrix D and further to compute optimal modulated module voltages V_k, however, the simulated measurement results of module currents are based on the assumption that internal impedances with true value given in Eq. (4.18) are connected to the time-varying external load. The results are summarized in Figure 4.6 and it is clear that in top figure, module currents keep separated and current balancing is severely compromised, in the presence of the same time-varying external load in Figure 4.5. A plot of time-varying nature of modulation $\alpha_k[t]$ is given in the middle figure of Figure 4.6 and it can be seen that module 1 is still set at 100%, which allows the other modules to be modulated down with different profile from Figure 4.5. Therefore, internal impedance Z_k estimation should be considered as a part of the current scheduling and an alternative approach would be to run an iterative loop (e.g. closed-loop control system) to balance the currents and then deduct the internal impedance from there.

4.4 Closed-loop Current Scheduling

4.4.1 Proportional-integral-derivative Control

In order to fix internal impedance Z_k estimation problem discussed in above section to balance module currents, a control model for buck regulated battery system uses distributed

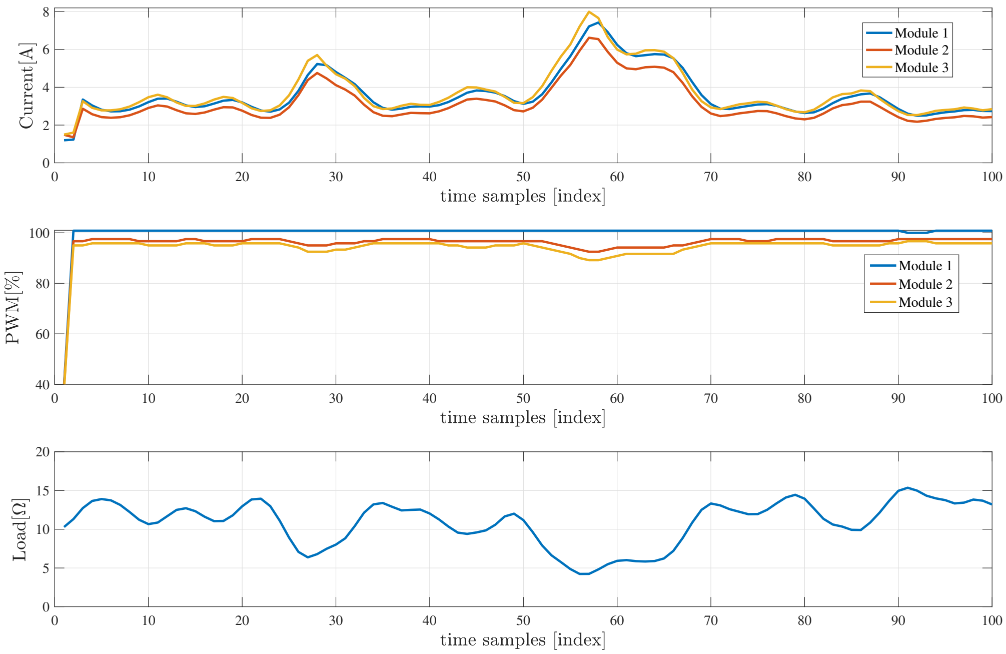

Figure 4.6. Currents in battery modules (top) and PWM modulation of battery voltage (middle) for recursive SOC balanced module scheduling of 3 parallel placed battery modules with inaccurate (small error) estimated internal impedance, subjected to a time-varying external load (bottom).

feedback control in each battery module. To do this, a proportional-integral-derivative (PID) controller with requisite corrective behavior in closed-loop is used in every individual battery module shown in Figure 4.7. This PID controller monitors the controlled module current I_k, and compares it with the reference current I_{ref} of each individual battery module. The current difference ε between actual and desired module current value, called current error signal, is applied as feedback to generate a controller output to maintain the module currents at the desired values by changing PWM duty cycle to modulate up and down module voltages V_k. The overall PID control function can be expressed mathematically in discrete-time (DT) digital system as

$$\begin{aligned} \mathrm{PWM}_k(t) &= K_p\varepsilon_k(t) + K_i\textstyle\sum_{n=1}^{t}\varepsilon_k(t) + K_d[\varepsilon_k(t) - \varepsilon_k(t-1)], \\ \varepsilon_k(t) &= I_{ref,k}(t) - I_k(t) \end{aligned} \tag{4.19}$$

where $I_k(t)$ is the measurement and $I_{ref,k}(t)$ is the reference of the current of the kth battery module. The resulting $\mathrm{PWM}_k(t)$ denotes the PWM dispatched to the buck regulator of the kth battery module at time instance t. The parameters K_p, K_i and K_d and are all non-negative and denote the coefficients for the proportional, integral, and derivative terms, respectively. It shows a PID controller, which continuously calculates an error value $\varepsilon_k(t)$ as the difference between a desired reference current $I_{ref,k}(t)$ and measured process module current $I_k(t)$, and applies a correction based on proportional, integral, and derivative terms in order to minimize the error over time by adjustment of a control variable PWM modulation $\mathrm{PWM}_k(t)$ by MOSFET buck regulated circuit. As indicated by Eq. (4.19), the PID control takes place using local information of the battery module only. As such, the PID control algorithm of Eq. (4.19) is distributed on each and every buck regulated battery module and typically runs at a sampling rate of 100Hz. To avoid integrator windup, limiters on the PWM duty cycle are put in place so that the controller output never reaches the modulation limits, as illustrated in Figure 4.7. Tuning a control loop is the adjustment of the gains of the proportional K_p, integral K_i and derivative K_d terms to the optimum values for the desired control response. Using the optimal control parameters can guarantee optimal control of the system or its control stability and reduce overshoot and the degree of any system oscillation. Applying PID controller with optimal three control terms in Eq. (4.19) into each individual module allows to bring the module current I_k to the same value as reference current I_{ref} in order to satisfy module currents I in Eq. (4.7) based on individual SOC.

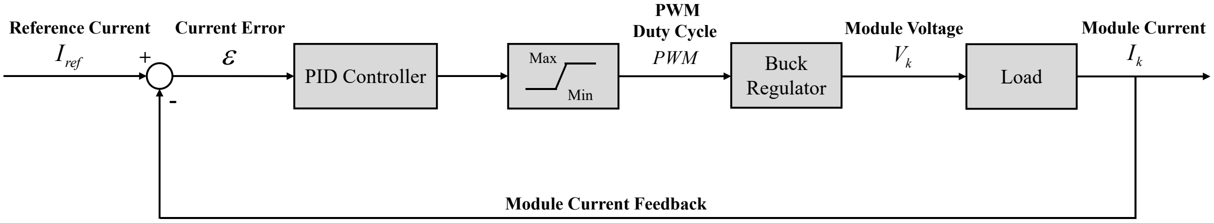

Figure 4.7. PID current loop control in buck regulated PWM circuit.

Coordination between the battery modules is accomplished via the reference signal I_{ref}

send to the battery modules and will be done at much lower rate, typically with an update rate of 1Hz. In case of equal recursive SOC current scheduling discussed above, every individual module current reference $I_{ref,k}$ should be adjusted to be same value of I_{ref}, mathematically expressed as

$$I_{ref,1} = I_{ref,2} = \cdots = I_{ref,n} = I_{ref} \tag{4.20}$$

However, the actual value of the common current reference I_{ref} is not known and depends on the load conditions and the battery parameters (OCV and impedance) of each battery module. Therefore it is necessary to adapt the common current reference I_{ref} to its maximum value where at least one of the battery modules reaches a dispatch signal PWM_k equal to or close to 100%.

4.4.2 Autonomous Closed-loop Control for Load-tracking

Using the PID controller discussed above can guarantee each individual current I_k to the same value of desired reference current I_{ref} without specific knowledge of internal impedance Z_k and external load impedance Z_l. In fact, the external load Z_l may be time-varying relatively fast due to fluctuating power demands and the reference current I_{ref} should be recursively updated to find optimal output currents to satisfy current scheduling objective. In this paper, we propose a novel autonomous closed-loop control method to automatically balance (equal) and find the optimal individual battery currents I_{opt} in Eq. (4.10) and Figure 4.8 gives the flowchart of the autonomous closed-loop control algorithm workflow when the external load is changed. This proposed autonomous closed-loop control approach can be achieved by continuously monitoring PWM duty cycle PWM_k and measuring module currents I_k of every individual module $k = 1, 2, \ldots, n$, as shown in Figure 4.8 and summarized in the following procedure.

Autonomous closed-loop control procedure:

1. Set initial time index $t = 0$ and communicate the n elements I_{ref} of the initial reference currents to each of the corresponding modules $k = 1, 2, \ldots, n$.

2. At time index t, perform a monitor of PWM duty cycle PWM_k and a measurement of

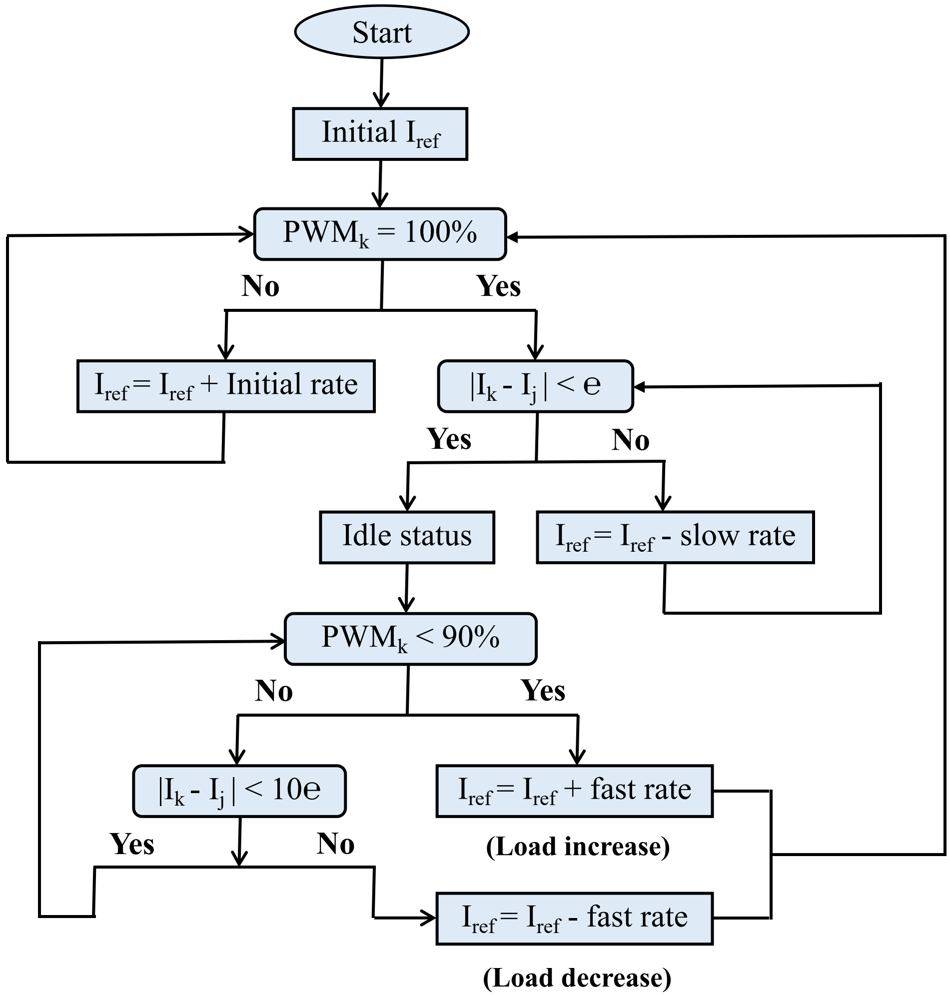

Figure 4.8. Flowchart of the autonomous closed-loop control algorithm workflow.

module current I_k of every individual module k. If any module gets to 100% (full) duty cycle, go to step 3, otherwise update the reference current $I_{ref} = I_{ref} +$ Initial rate with a fast ramp-up rate noted by "initial rate" to increase module current I_k.

3. If any module gets to 100% (full) duty cycle and the absolute current difference between different modules $|I_k - I_j|$ is less than the current difference threshold e, optimal module currents I_{opt} are found and set to be the same value as the reference current I_{ref} sending the system into an idle status. If not, decrease reference current I_{ref} to $I_{ref} = I_{ref} -$ slow rate with a small ramp-down rate and repeat step 3 until go to idle status.

4. After getting into idle status, if PWM duty cycle of every module suddenly drops lower than threshold PWM value 90%, the reference current I_{ref} needs to be increased to $I_{ref} = I_{ref} +$ fast rate with relatively large ramp-up rate and repeat from step 2, in order to satisfy larger optimal balanced module currents I_{opt} due to load increase (load impedance Z_l decrease) demand. If PWM keeps larger than and equal to threshold PWM value 90%, go to step 5.
5. In case that PWM duty cycle of every module suddenly still keeps larger than and equal to threshold PWM value 90% but absolute current difference between different modules $|I_k - I_j|$ becomes larger than bigger threshold $10e$, it is necessary to decrease reference current I_{ref} to $I_{ref} = I_{ref} -$ fast rate with same ramp-up rate in step 4 in order to find optimal balanced current I_{opt} due to load decrease (load impedance Z_l increase) demand. Restart from step 2.

It should be noted that the nature of the algorithm tries to make at least 1 module run at full modulation 100% and balance all module currents to be equal in above proposed equal SOC current scheduling given in (4.8). As a matter of fact that PWM duty cycle is between 0% (fully off) and 100% (fully on), limited resolution of current sensor and MOSFET may result overmodulation (eg.110%) to keep module currents equal of optimal value. In such case, the optimal reference current I_{ref} value to each module needs to be decreased slightly so as to satisfy PWM duty cycle in reasonable range, therefore, at least 1 module may not run at 100% PWM all the time, but very close to it. In addition, this closed-loop control algorithm provides a current scheduling solution that keeps tracking PWM duty cycle of all modules without given any knowledge of OCV, internal impedance, and load impedance, and such feedback control can converge in a short time. The measurement of the module current and the controller output current can be done within any module in relative fast rate without any communication requirements, and the updates on changing reference current I_{ref} would take place at a much slower rate in the central communication to each of the modules.

4.5 Experimental Verification

4.5.1 Experimental Setup

An experimental setup used for the validation of the proposed optimal current scheduling consists of 3 parallel connected buck regulated battery modules, where the modulation demand signal can be applied and recorded and the current of each battery module can be measured simultaneously. The schematic diagram of the experimental battery tester illustrated in Figure 4.9 is referred to explicitly explain the experimental setup. The parallel connection of 3 buck regulated battery modules is connected to an electrical load with a parallel connection of load resistors by common DC bus. Specifically, each parallel connected buck regulated battery module consists of an adjustable power supply in series with a potentiometer and a buck regulator placed on module board. The buck regulator is composed of a PWM driven MOSFET, a fly-by diode and an inductor, and controlled by an Arduino Uno board.

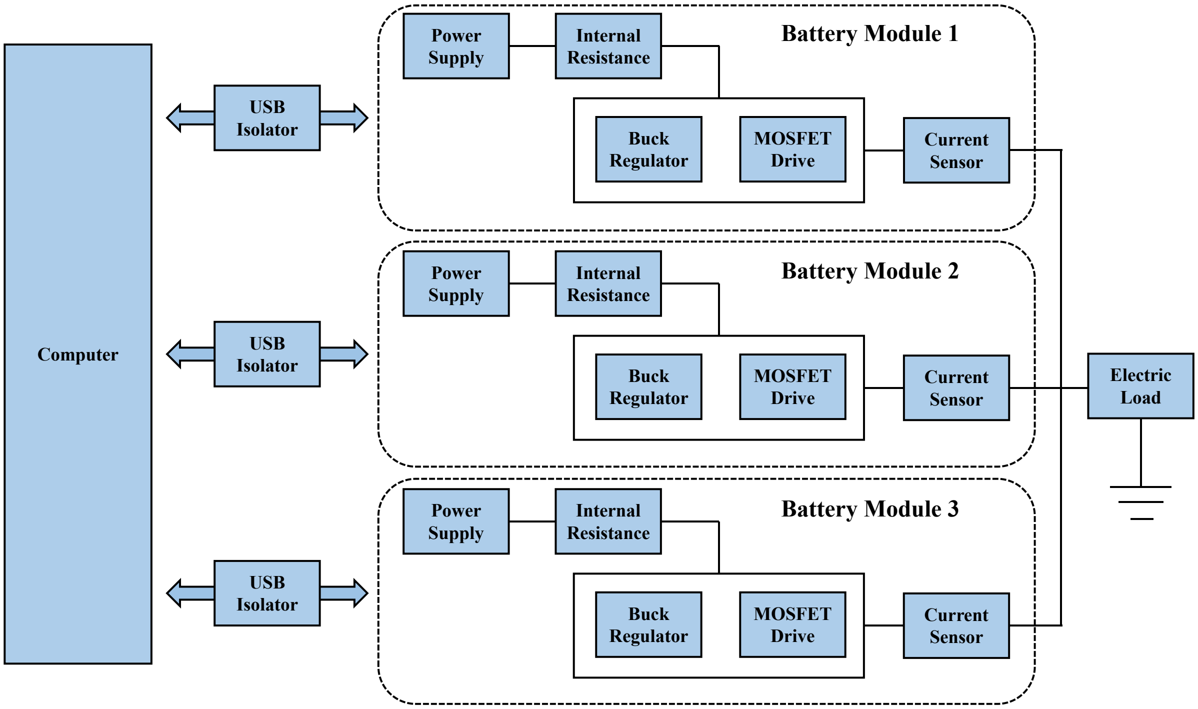

Figure 4.9. Schematic of the experimental battery tester.

A photograph is used to explicitly summarize and describe the experimental battery tester shown in Figure 4.10. The Tekpower TP5003T Variable Digital DC Power Supply with maximum output voltage of up to 50 V and current up to 3 A is used in the experiment. The MOSFET's gate placed on the buck regulator is connected to a PWM pin on Arduino Uno board, where the average value of voltage (and current) fed to the load can be controlled by tuning the switch between supply and load on and off at a ultrafast rate. The Arduino Uno board can be also employed to measure module current real-time signals by its analog input pins, and simultaneously communicate with the computer through USB isolator cable. The USB isolator is used to protect experiment equipment from electrical overvoltage and transient voltage spikes, by eliminating ground loop currents flowing between the computer and Arudino board which can cause damage and inaccurate measurements. The current sensor on module board is around 27 mA/bit and the bandwidth is approximate 1 KHz single pole on the sensor. In the computer, MATLAB provides the numerical computing environment automatically implement current scheduling algorithms and save measured real-time data as well. In addition, PWM switching frequency applied in MOSFETs is set to be 62.5 kHz driven by Arduino PWM pins in the experiment. The MOSFETs are with low drain-to-source on-resistance that is suitable for high current of battery modules. All tests are executed at a controlled ambient temperature of 25 $°C$.

4.5.2 Voltage versus PWM Duty Cycle Linearity Test

The buck regulated PWM control circuit is used in efficient voltage regulators by switching voltage to the load with the appropriate duty cycle and the smooth output current is obtained with a RC filter. MOSFET on buck regulator is driven by PWM switching frequency 62.5 kHz on the Arduino Uno pin 9 and the experiment output voltages of 3 buck regulated PWM control circuit are measured by varying PWM duty cycle from 0 to 100% with a 5% step, as summarized in Figure 4.11. The relationship between these two can be approximately considered as linearity and the 3 fitting lines have relatively close coefficients but totally different, which shows the influence of the parasitic resistances of the circuit on the performances. Voltage linearity becomes

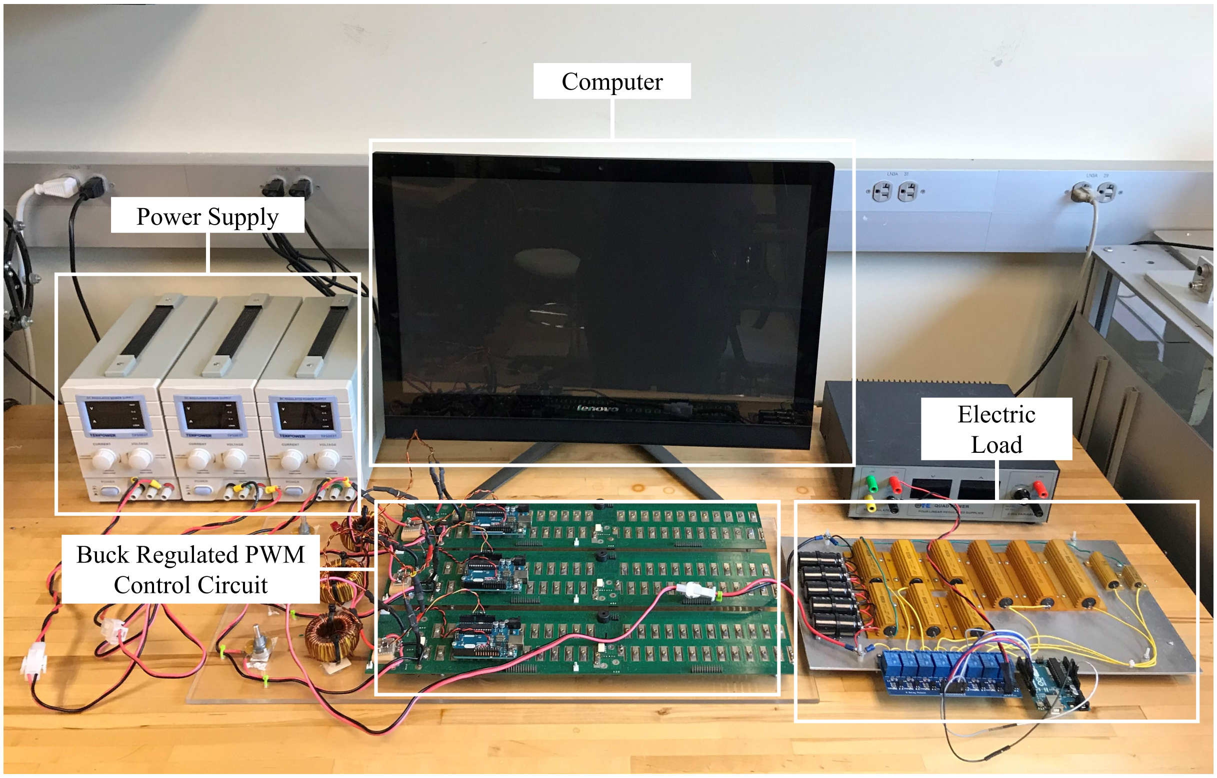

Figure 4.10. Photograph of the experimental battery tester.

degraded for low PWM duty cycle for all 3 modules in the discontinuous mode when the amount of energy required by the load is too small. The inductor kickback pulse can not stay high for very long time and the diode comes out of conduction sometimes during the off portion, which causes the coil voltage collapse and even overshoots due to the resonance with the field-effect transistor (FET) capacitance and coil self capacitance. So then the FET starts conducting due to the overshoot across the body diode during a portion of the ”off ” period and the linearity between voltage output and PWM duty cycle no longer applies. Therefore, running autonomous closed-loop control for load-tracking requires to stay in linear areas of high PWM duty cycle in the experimental tests.

4.5.3 Experimental Results with Varying Load Conditions

In order to verify the applicability of the decentralized closed-loop control algorithms with autonomous load-tracking, the experimental setup is used to emulate 3 parallel placed

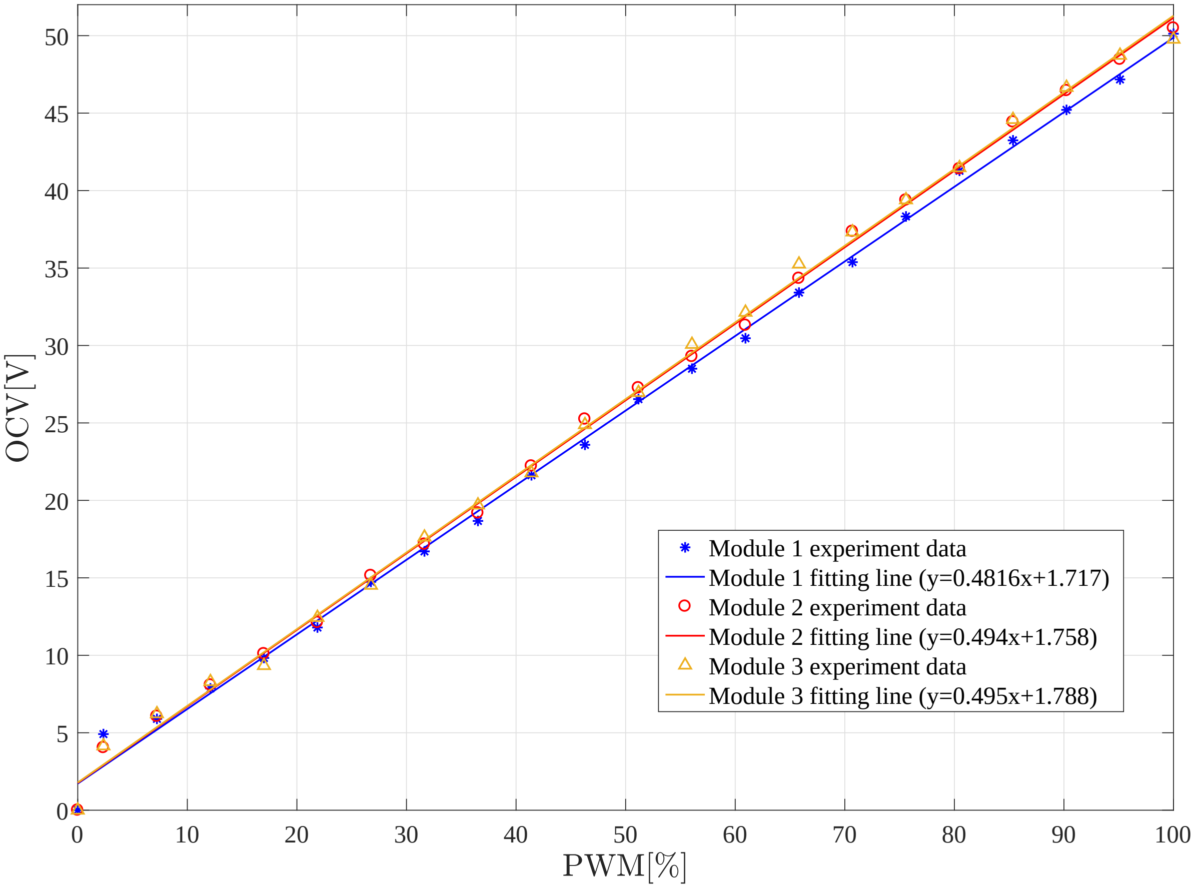

Figure 4.11. Output voltage experiment data and fitting line of 3 battery modules as a function of PWM modulation duty cycle.

battery modules with full scale open-circuit voltages (OCVs) of $V_1^{OCV} = 48$ V, $V_2^{OCV} = 49$ V, $V_3^{OCV} = 50$ V and internal impedance values $Z_1 = 4\Omega$, $Z_2 = 3\Omega$, and $Z_3 = 2\Omega$. Furthermore, cable and module board resistance is not accounted into the internal impedance, hence the true module impedance values may be different from the assigned impedance values created by the variable resistors. The discrepancy between OCVs and impedances is used to emulate mixed battery modules. The decentralized PID controller of Eq. (4.19) for each module is the same and tuned to have the control parameters $K_p = 1$, $K_i = 0.3$, $K_d = 0.5$ and operating at a sampling rate of 100Hz.

For the experimental results with varying load conditions included in this paper, it is first assumed based on that each module has the same SOC $SOC_1 = SOC_2 = SOC_3$ and capacity

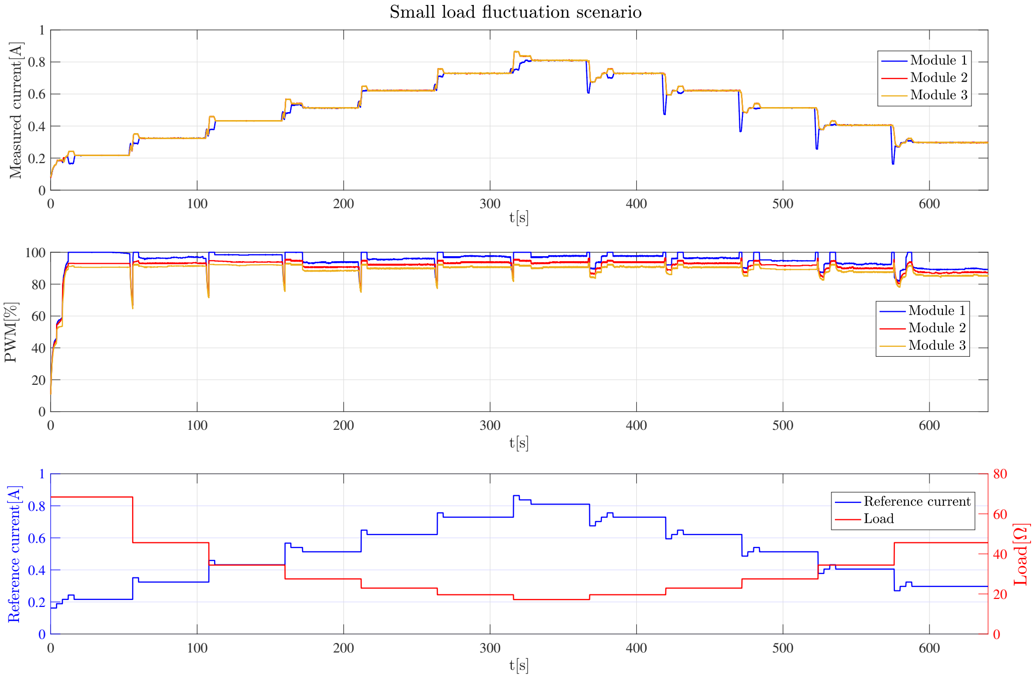

Figure 4.12. Currents (top) and modulation of battery voltages (middle) in battery modules for autonomous module current scheduling of 3 parallel placed battery modules, reference current and time-varying external load impedance (bottom) under small load fluctuation scenario.

storage $C_1 = C_2 = C_3$ to focus on the requirement of equal current scheduling $I_1 = I_2 = I_3$. Two test were performed: both a small step-wise changing external load scenario shown in (the bottom plot of) Fig. 4.12 and a large step-wise changing external load scenario shown in (the bottom plot of) Fig. 4.13 are used to validate the decentralized closed-loop control algorithms with autonomous load-tracking. It should be pointed out that internal impedance information Z_k and the timing and size of the step in the load Z_l are unknown to the decentralized closed-loop control algorithms.

In both scenarios, the requirement of equal current scheduling $I_1 = I_2 = I_3$ is used to evaluate the to validate the decentralized closed-loop control algorithms with autonomous load-tracking. From the top plots of Fig. 4.12 and Fig. 4.13 it can be observed that the decentralized control algorithm enables the 3 module currents to stay relatively closed at steady-state levels equal to each other without any knowledge of internal impedance Z_k and variations in the load

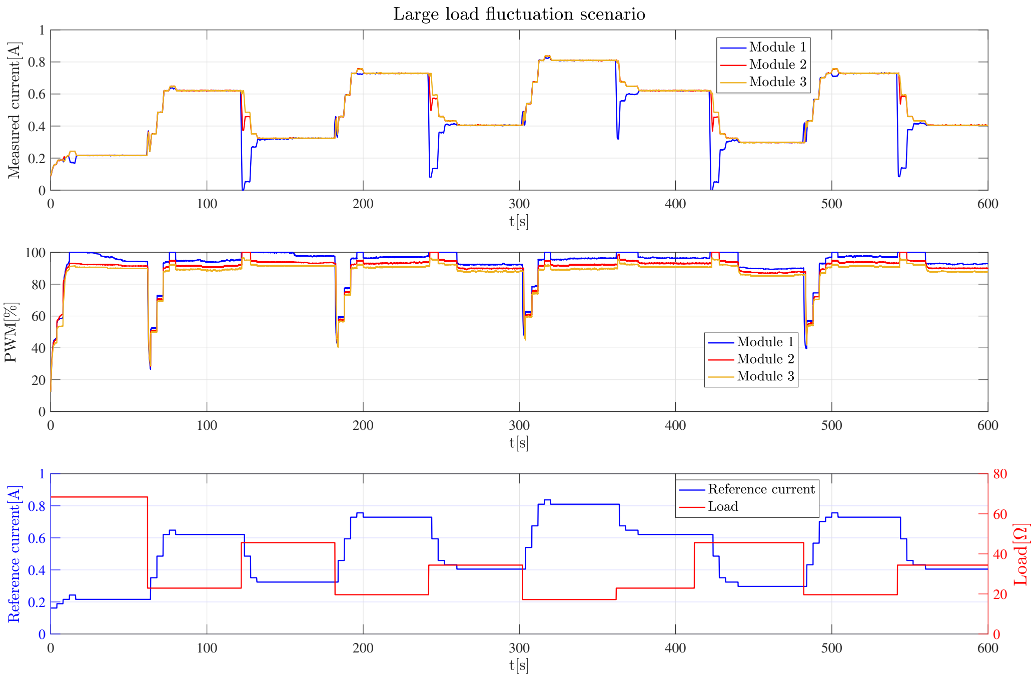

Figure 4.13. Currents (top) and modulation of battery voltages (middle) in battery modules for autonomous module current scheduling of 3 parallel placed battery modules, reference current and time-varying external load impedance (bottom) under large load fluctuation scenario.

Z_l.

From the middle plots of Fig. 4.12 and Fig. 4.13 it can be observed that one of that at least one of modules has a PWM α_k close to 100%, indicating that the autonomous load-tracking maximizes the power output of the battery pack. In addition, increasing PWM requires certain ramp-up period but decreasing PWM can happen instantaneously in order to protect the battery modules. The reference current signals are updated every 4 seconds and recorded in the bottom plot of Fig. 4.12 and Fig. 4.13, which also included the load variation Z_l.

In the third test with varying load conditions included in this paper, it is assumed based on that modules have the same SOC the same SOC $SOC_1 = SOC_2 = SOC_3$, but have a variation in the capacity storage captured by the relationship $C_1 = C_2 = 0.8C_3$. To ensure the SOC of each module progresses simultaneously, the reference current in (4.20) needs to be altered to $I_{ref,1} = I_{ref,2} = 0.8I_{ref,3}$.

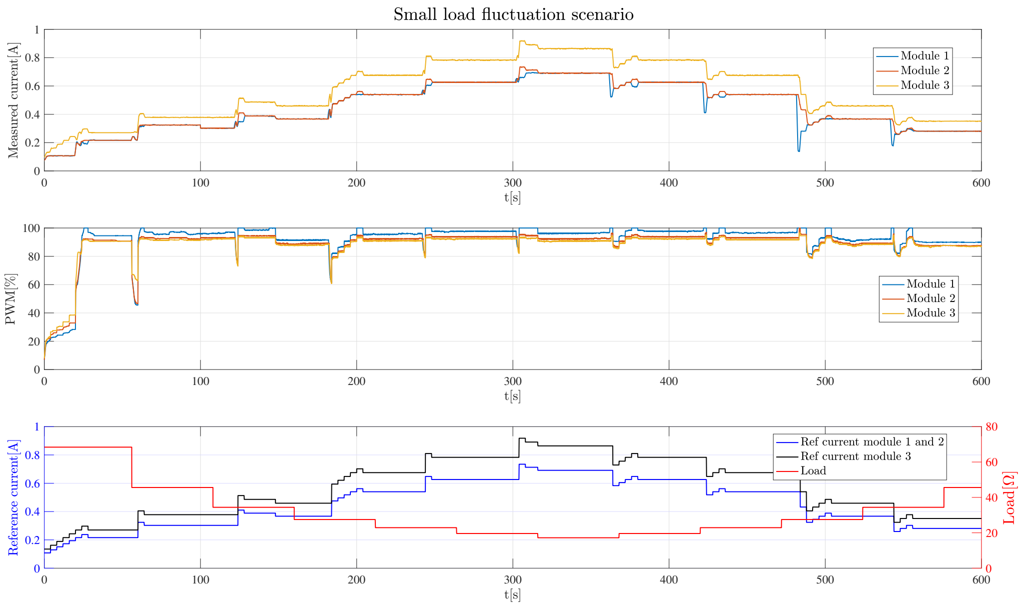

Figure 4.14. Currents (top) and modulation of battery voltages (middle) in battery modules for autonomous module current scheduling of 3 parallel placed battery modules, reference current and time-varying external load impedance (bottom) under small load fluctuation scenario.

The small step-wise changing external load scenario shown in (the bottom plot of) Fig. 4.14 is used to evaluate the current scheduling using autonomous demand tracking. From the top plot of Fig. 4.14, it can be observed that the decentralized control algorithm schedules the 3 module currents proportional to the assumed capacity of the modules. The experiment result shows that currents out of module 1 and module 2 remain the same and slightly lower (around 80%) than module 3 because their capacity degrades to 80% in order to accommodate their limited capacity of 80% compared to module 3. In addition, from the middle plot of Fig. 4.14, it can be seen that in Module 1 always stays at or is close to 100% due to its highest impedance and capacity, and lowest OCV.

4.6 Summary

Modular battery systems that consist of parallel placed battery modules are essential in range extension of electric vehicles and re-purposing of batteries for integration as energy storage in grid applications. The performance of such modular battery system can be significantly improved if combining or mixing of modules is robust to open-circuit voltage (OCV), state of charge (SOC) and internal impedance of each module.

This paper provides a solution to eliminate module-to-module differences by using buck regulators on each battery module along with distributed closed-loop control with autonomous load-tracking to allow current scheduling of parallel placed battery modules. The distributed closed-loop control is based on standard digital PID control that monitors module current and adjust pulse width modulation (PWM) to the buck regulators to maximize total battery power output. Maximum battery output is accomplished by maximizing the PWM cycle of all modules by ensuring that at least 1 module runs at full PWM of 100% and module currents are balanced. This is accomplished without the explicit knowledge of the module OCV, module internal impedance and total load impedance.

Experimental results verify the feasibility, effectiveness and accuracy of proposed autonomous demand-side current scheduling of parallel buck regulated battery modules for balancing current out of each individual battery module. Implementation results indicate that balancing individual battery module can be done within each module with fast rate decentralized control, while reference current for real-time load tracking can be updated at slower update rates in order to efficiently reduce the centralized communication requirements. The future work of this study is to apply this proposed autonomous closed-loop control technique into battery management system (BMS) of modular battery systems to improve battery pack performance and extend battery pack lifespan.

4.7 Acknowledge

Chapter 4, in part is currently submitted under review or published in the following papers. The dissertation/thesis author was the primary investigator and author of these material. **Yunfeng Jiang**, Louis, J. Shrinkle, Raymond A. de Callafon, “Autonomous demand-side current

scheduling of parallel buck regulated battery modules", *Energy* (submitted).

Yunfeng Jiang, Abdulelah H. Habib, Xin Zhao, Louis J. Shrinkle, Raymond A. de Callafon, "Centralized recursive optimal scheduling of parallel buck regulated battery modules", *in the 56th IEEE Conference on Decision and Control (CDC)*, Melbourne, Australia, December 12-15, 2017.

Chapter 5

Conclusion and Future Work

In order to meet emerging requirements for significantly improving safety and better utilization of battery energy storage system (BESS) in the electrified vehicles and electric grids, systematic research on applying system identification methods, advanced modeling and control technologies is highly required, In this dissertation, three main problems are thoroughly studied: a) battery modeling; b) power prediction; c)current scheduling. The summary for completed and future work is as follows.

- **Battery State of Charge Modeling:** This dissertation presents a battery model with non-integer order derivatives to describe Lithium-ion battery (LIB) behavior over relatively large operating range, which is a combination of conventional 1-resistor-capacitor (1-RC) electrical circuit model (ECM) and electrochemical impedance spectroscopy (EIS) experimental result. The proposed non-integer or fractional differential model (FDM) includes a constant phase element term to approximate the non-linear dynamical behavior of the battery. The standard least squares-based state-variable filter (LSSVF) identification method used for continuous-time (CT) system identification is used to estimate the model parameters and the fractional derivative coefficients of the proposed FDM. For application of modeling fractional differential order battery dynamics, the CT LSSVF parameter estimation approach is extended to an instrumental variable (IV) method to be robust to (non-white) noise perturbed output measurement. The model accuracy and model performance are validated on experimental data obtained from a LIB and confirm that the proposed FDM is able to accurately capture the battery dynamics over broad operating range. In comparison, the FDM also shows significant improvement on data prediction accuracy compared to a conventional integer model, making the FDM more suitable for monitoring battery dynamical behavior in a battery management system (BMS).

Future Work: The proposed modeling approach is expected to be first implemented and validated on experimental data from a larger-scale battery system, such as a battery energy storage system (BESS) in electrical vehicle (EV) and static energy storage system in renewable energy industry.

- **Battery Power prediction:**A fractional derivative battery modeling approach is proposed to predict power storage and delivery dynamic behavior of a battery system, given charge and discharge demand as input, where fractional derivatives are applied to approximate non-linear dynamic behavior of a battery system not only in normal operating range, but also in some extreme situation, such as over-charging and over-discharging. The proposed modeling approach is actually from control perspective, which is significantly different from the conventional ECMs and electrochemical models. In particular, the battery power prediction model is composed of voltage and current models, separately. The LSSVF method commonly used in the identification of CT models is extended to allow the estimation of fractional derivative coefficients and parameters of the battery models by monitoring a charge/discharge demand signal and a power storage/delivery signal. Based on experimental data, it is illustrated how the FDM can be utilized to predict the dynamics of the energy storage and delivery of a lithium iron phosphate battery ($LiFePO_4$) in real-time. The results indicate that a FDM can accurately capture the dynamics of the energy storage and delivery of a LIB over a large operating range, even in over-charging and over-discharging cases. It is also shown that the FDM exhibits improvements on prediction performance compared to standard integer derivative model, which in beneficial for a BMS.

Future Work: The proposed power prediction model method needs to be improved in parameterization and estimation of the components, especially in the fractional derivative optimization in the formulated model framework. The feasibility and performance of such novel model method is also expected to be applied and validated in larger-scale battery applications, such as battery pack system in automotive industry and BESS connected to the electric grid in the renewable industry.

- **State of Charge Balancing:** This dissertation proposes the algorithms, hardware overview and testing results for controlling discharge currents from mixed battery modules configured in a parallel connection. The battery modules are considered to be mixed as they may have discrepancies and time-dependent variations in open circuit voltage (OCV) and impedance characteristics. Parallel placed battery modules are used to increase power and energy storage capacity in mobile, electric vehicle (EV) and static energy storage application. Mixing of battery modules is typically seen in second-life, repurposed or exchangeable battery systems. When battery modules with different age or charge characteristics are combined to generate a larger storage capacity, battery heterogeneity is widely known to negatively impact the performance, lifespan and safety of the total battery pack. This dissertation addresses such battery heterogeneity by taking advantage of buck regulators on each battery module and formulating a scheduling algorithm for dispatching the buck regulators to balance the current out of each battery module. In this way, heterogeneous battery modules can be mixed and coordinated to provide a desired power flow from the battery pack. The scheduling algorithms presented in this dissertation are formulated in both an open-loop and a closed-loop implementation. In the open-loop algorithm, optimal dispatch commands are computed based on knowledge of the OCV and impedance of each battery module, while monitoring the load impedance. In the closed-loop algorithm, optimal dispatch commands are computed autonomously by a recursive control algorithm that monitors both load impedance and battery module currents. It is shown that especially the closed-loop algorithm, guarantees robust operation without violating battery module operating constraint, even when the battery module characteristic parameters change as the battery pack ages. This novel scheduling method is validated through an experimental representation of a battery pack with 3 parallel placed buck regulated battery modules with heterogeneity in internal impedance and OCV. The experimental results show how battery current can be kept balanced within operating limits and illustrate the feasibility and effectiveness of proposed current scheduling method in a real battery application.

Future Work: The proposed current scheduling technique is expected to apply in more battery modules and larger-scale parallel-connected battery pack system into EV and electric grid applications. The current communication hardware can be improved by up-to-date wireless communication platforms in order to avoid communication problems. For future research, instead of only current scheduling, power scheduling needs to be further addressed to optimize battery power output and energy transformation.

Bibliography

[1] M. Eckert, L. Kölsch, S. Hohmann, Fractional algebraic identification of the distribution of relaxation times of battery cells, in: Decision and Control (CDC), 2015 IEEE 54th Annual Conference on, IEEE, 2015, pp. 2101–2108.

[2] N. A. Chaturvedi, R. Klein, J. Christensen, J. Ahmed, A. Kojic, Algorithms for advanced battery-management systems, IEEE Control Systems 30 (3) (2010) 49–68.

[3] X. Zhao, R. A. de Callafon, Data-based modeling of a lithium iron phosphate battery as an energy storage and delivery system, in: American Control Conference (ACC), 2013, IEEE, 2013, pp. 1908–1913.

[4] L. H. Saw, H. M. Poon, H. San Thiam, Z. Cai, W. T. Chong, N. A. Pambudi, Y. J. King, Novel thermal management system using mist cooling for lithium-ion battery packs, Applied Energy 223 (2018) 146–158.

[5] I. H. Shah, C. Hiles, B. Morley, How do oil prices, macroeconomic factors and policies affect the market for renewable energy?, Applied Energy 215 (2018) 87–97.

[6] M. Armand, J.-M. Tarascon, Building better batteries, nature 451 (7179) (2008) 652.

[7] H. Kanchev, D. Lu, F. Colas, V. Lazarov, B. Francois, Energy management and operational planning of a microgrid with a pv-based active generator for smart grid applications, IEEE transactions on industrial electronics 58 (10) (2011) 4583–4592.

[8] Z. Deng, L. Yang, Y. Cai, H. Deng, L. Sun, Online available capacity prediction and state of charge estimation based on advanced data-driven algorithms for lithium iron phosphate battery, Energy 112 (2016) 469–480.

[9] C. Zhang, Y. Jiang, J. Jiang, G. Cheng, W. Diao, W. Zhang, Study on battery pack consistency evolutions and equilibrium diagnosis for serial-connected lithium-ion batteries, Applied Energy 207 (2017) 510–519.

[10] P. T. Coman, E. C. Darcy, C. T. Veje, R. E. White, Numerical analysis of heat propagation in a battery pack using a novel technology for triggering thermal runaway, Applied Energy 203 (2017) 189–200.

[11] Y. Wang, W. Shi, B. Wang, C.-C. Chu, R. Gadh, Optimal operation of stationary and mobile batteries in distribution grids, Applied Energy 190 (2017) 1289–1301.

[12] S. J. Tong, A. Same, M. A. Kootstra, J. W. Park, Off-grid photovoltaic vehicle charge using second life lithium batteries: An experimental and numerical investigation, Applied Energy 104 (2013) 740–750.

[13] Y. Deng, J. Li, T. Li, J. Zhang, F. Yang, C. Yuan, Life cycle assessment of high capacity molybdenum disulfide lithium-ion battery for electric vehicles, Energy 123 (2017) 77–88.

[14] M. F. Felgenhauer, M. A. Pellow, S. M. Benson, T. Hamacher, Evaluating co-benefits of battery and fuel cell vehicles in a community in california, Energy 114 (2016) 360–368.

[15] Y. Xing, E. W. Ma, K. L. Tsui, M. Pecht, Battery management systems in electric and hybrid vehicles, Energies 4 (11) (2011) 1840–1857.

[16] B. Xia, C. Mi, A fault-tolerant voltage measurement method for series connected battery packs, Journal of Power Sources 308 (2016) 83–96.

[17] A. T. Elsayed, C. R. Lashway, O. A. Mohammed, Advanced battery management and diagnostic system for smart grid infrastructure, IEEE Transactions on Smart Grid 7 (2) (2016) 897–905.

[18] A. Jossen, Fundamentals of battery dynamics, Journal of power sources 154 (2) (2006) 530–538.

[19] J. Vetter, P. Novák, M. Wagner, C. Veit, K.-C. Möller, J. Besenhard, M. Winter, M. Wohlfahrt-Mehrens, C. Vogler, A. Hammouche, Ageing mechanisms in lithium-ion batteries, Journal of power sources 147 (1-2) (2005) 269–281.

[20] W. Diao, N. Xue, V. Bhattacharjee, J. Jiang, O. Karabasoglu, M. Pecht, Active battery cell equalization based on residual available energy maximization, Applied Energy 210 (2018) 690–698.

[21] F. Altaf, L. Johannesson, B. Egardt, Simultaneous thermal and state-of-charge balancing of batteries: A review, in: Vehicle Power and Propulsion Conference (VPPC), 2014 IEEE, IEEE, 2014, pp. 1–7.

[22] M. M. U. Rehman, M. Evzelman, K. Hathaway, R. Zane, G. L. Plett, K. Smith, E. Wood, D. Maksimovic, Modular approach for continuous cell-level balancing to improve performance of large battery packs, in: Energy Conversion Congress and Exposition (ECCE), 2014 IEEE, IEEE, 2014, pp. 4327–4334.

[23] R. Gogoana, M. B. Pinson, M. Z. Bazant, S. E. Sarma, Internal resistance matching for parallel-connected lithium-ion cells and impacts on battery pack cycle life, Journal of Power Sources 252 (2014) 8–13.

[24] Y. Zheng, M. Ouyang, L. Lu, J. Li, Understanding aging mechanisms in lithium-ion battery packs: From cell capacity loss to pack capacity evolution, Journal of Power Sources 278 (2015) 287–295.

[25] K.-C. Chiu, C.-H. Lin, S.-F. Yeh, Y.-H. Lin, C.-S. Huang, K.-C. Chen, Cycle life analysis of series connected lithium-ion batteries with temperature difference, Journal of Power Sources 263 (2014) 75–84.

[26] Y. Jiang, B. Xia, X. Zhao, T. Nguyen, C. Mi, R. A. de Callafon, Data-based fractional differential models for non-linear dynamic modeling of a lithium-ion battery, Energy 135 (2017) 171–181.

[27] S. Santhanagopalan, Q. Guo, P. Ramadass, R. E. White, Review of models for predicting the cycling performance of lithium ion batteries, Journal of Power Sources 156 (2) (2006) 620–628.

[28] M. Mastali, E. Samadani, S. Farhad, R. Fraser, M. Fowler, Three-dimensional multi-particle electrochemical model of lifepo4 cells based on a resistor network methodology, Electrochimica Acta 190 (2016) 574–587.

[29] D. Zhang, B. N. Popov, R. E. White, Modeling lithium intercalation of a single spinel particle under potentiodynamic control, Journal of The Electrochemical Society 147 (3) (2000) 831–838.

[30] R. Xiong, F. Sun, Z. Chen, H. He, A data-driven multi-scale extended kalman filtering based parameter and state estimation approach of lithium-ion olymer battery in electric vehicles, Applied Energy 113 (2014) 463–476.

[31] H. He, R. Xiong, J. Fan, Evaluation of lithium-ion battery equivalent circuit models for state of charge estimation by an experimental approach, Energies 4 (4) (2011) 582–598.

[32] J. Xu, C. C. Mi, B. Cao, J. Cao, A new method to estimate the state of charge of lithium-ion batteries based on the battery impedance model, Journal of power sources 233 (2013) 277–284.

[33] A. Oustaloup, F. Levron, B. Mathieu, F. M. Nanot, Frequency-band complex noninteger differentiator: characterization and synthesis, IEEE Transactions on Circuits and Systems I: Fundamental Theory and Applications 47 (1) (2000) 25–39.

[34] I. Petráš, Fractional-order nonlinear systems: modeling, analysis and simulation, Springer Science & Business Media, 2011.

[35] C. A. Monje, Y. Chen, B. M. Vinagre, D. Xue, V. Feliu-Batlle, Fractional-order systems and controls: fundamentals and applications, Springer Science & Business Media, 2010.

[36] Y. Jiang, X. Zhao, A. Valibeygi, R. A. de Callafon, Dynamic prediction of power storage and delivery by data-based fractional differential models of a lithium iron phosphate battery, Energies 9 (8) (2016) 590.

[37] T. Kaczorek, K. Rogowski, Fractional linear systems and electrical circuits, Springer, 2015.

[38] L. Kexue, P. Jigen, Laplace transform and fractional differential equations, Applied Mathematics Letters 24 (12) (2011) 2019–2023.

[39] A. Tepljakov, Fomcon: Fractional-order modeling and control toolbox, in: Fractional-order Modeling and Control of Dynamic Systems, Springer, 2017, pp. 107–129.

[40] Y. Jiang, B. Xia, X. Zhao, T. Nguyen, C. Mi, R. A. de Callafon, Identification of fractional differential models for lithium-ion polymer battery dynamics, IFAC-PapersOnLine 50 (1) (2017) 405–410.

[41] Y. Hu, S. Yurkovich, Linear parameter varying battery model identification using subspace methods, Journal of Power Sources 196 (5) (2011) 2913–2923.

[42] S. Lee, J. Kim, J. Lee, B. H. Cho, State-of-charge and capacity estimation of lithium-ion battery using a new open-circuit voltage versus state-of-charge, Journal of power sources 185 (2) (2008) 1367–1373.

[43] G. Rao, H. Unbehauen, Identification of continuous-time systems, IEE Proceedings-Control theory and applications 153 (2) (2006) 185–220.

[44] B. Xia, X. Zhao, R. De Callafon, H. Garnier, T. Nguyen, C. Mi, Accurate lithium-ion battery parameter estimation with continuous-time system identification methods, Applied energy 179 (2016) 426–436.

[45] H. Garnier, M. Mensler, A. Richard, Continuous-time model identification from sampled data: implementation issues and performance evaluation, International journal of Control 76 (13) (2003) 1337–1357.

[46] J. Remmlinger, M. Buchholz, M. Meiler, P. Bernreuter, K. Dietmayer, State-of-health monitoring of lithium-ion batteries in electric vehicles by on-board internal resistance estimation, Journal of Power Sources 196 (12) (2011) 5357–5363.

[47] H. Garnier, P. C. Young, The advantages of directly identifying continuous-time transfer function models in practical applications, International Journal of Control 87 (7) (2014) 1319–1338.

[48] H. Wu, S. Yuan, X. Zhang, C. Yin, X. Ma, Model parameter estimation approach based on incremental analysis for lithium-ion batteries without using open circuit voltage, Journal of Power Sources 287 (2015) 108–118.

[49] S. Yuan, H. Wu, X. Ma, C. Yin, Stability analysis for li-ion battery model parameters and state of charge estimation by measurement uncertainty consideration, Energies 8 (8) (2015) 7729–7751.

[50] H. Garnier, Direct continuous-time approaches to system identification. overview and benefits for practical applications, European Journal of control 24 (2015) 50–62.

[51] H. Garnier, R. R. Bitmead, R. A. de Callafon, Direct continuous-time model identification of high-powered light-emitting diodes from rapidly sampled thermal step response data, IFAC Proceedings Volumes 47 (3) (2014) 6430–6435.

[52] L. Ljung, System identification: theory for the user, Prentice-hall, 1987.

[53] K. Diethelm, The analysis of fractional differential equations: An application-oriented exposition using differential operators of Caputo type, Springer Science & Business Media, 2010.

[54] H. Garnier, M. Gilson, T. Bastogne, M. Mensler, The contsid toolbox: A software support for data-based continuous-time modelling, in: Identification of continuous-time models from sampled data, Springer, 2008, pp. 249–290.

[55] R. Malti, S. Victor, A. Oustaloup, H. Garnier, An optimal instrumental variable method for continuous-time fractional model identification, in: 17th IFAC World Congress, 2008, p. XX.

[56] P. C. Young, H. Garnier, M. Gilson, Refined instrumental variable identification of continuous-time hybrid box-jenkins models, in: Identification of continuous-time models from sampled data, Springer, 2008, pp. 91–131.

[57] J. Schorsch, H. Garnier, M. Gilson, P. C. Young, Instrumental variable methods for identifying partial differential equation models, International Journal of Control 86 (12) (2013) 2325–2335.

[58] P. Young, H. Garnier, M. Gilson, An optimal instrumental variable approach for identifying hybrid continuous-time box-jenkins models, in: 14th IFAC Symposium on System Identification, SYSID'2006, Elsevier, 2006, pp. 225–230.

[59] X. Hu, S. Li, H. Peng, A comparative study of equivalent circuit models for li-ion batteries, Journal of Power Sources 198 (2012) 359–367.

[60] J.-B. Jorcin, M. E. Orazem, N. Pébère, B. Tribollet, Cpe analysis by local electrochemical impedance spectroscopy, Electrochimica Acta 51 (8-9) (2006) 1473–1479.

[61] C. L. Alexander, B. Tribollet, M. E. Orazem, Contribution of surface distributions to constant-phase-element (cpe) behavior: 1. influence of roughness, Electrochimica Acta 173 (2015) 416–424.

[62] P. Zoltowski, On the electrical capacitance of interfaces exhibiting constant phase element behaviour, Journal of Electroanalytical Chemistry 443 (1) (1998) 149–154.

[63] Y. Cai, M. Ouyang, F. Yang, Impact of power split configurations on fuel consumption and battery degradation in plug-in hybrid electric city buses, Applied Energy 188 (2017) 257–269.

[64] Y. Jiang, A. H. Habib, X. Zhao, L. J. Shrinkle, R. A. de Callafon, Centralized recursive optimal scheduling of parallel buck regulated battery modules, in: Decision and Control (CDC), 2017 IEEE 56th Annual Conference on, IEEE, 2017, pp. 2029–2034.

[65] R. Finesso, E. Spessa, M. Venditti, Cost-optimized design of a dual-mode diesel parallel hybrid electric vehicle for several driving missions and market scenarios, Applied energy 177 (2016) 366–383.

[66] M. Siu, P. K. Mok, K. N. Leung, Y.-H. Lam, W.-H. Ki, A voltage-mode pwm buck regulator with end-point prediction, IEEE Transactions on Circuits and Systems II: Express Briefs 53 (4) (2006) 294–298.

[67] J. Sturm, H. Ennifar, S. Erhard, A. Rheinfeld, S. Kosch, A. Jossen, State estimation of lithium-ion cells using a physicochemical model based extended kalman filter, Applied Energy 223 (2018) 103–123.

[68] X. Zhao, R. A. de Callafon, L. Shrinkle, Current scheduling for parallel buck regulated battery modules, IFAC Proceedings Volumes 47 (3) (2014) 2112–2117.

[69] M. M. U. Rehman, F. Zhang, M. Evzelman, R. Zane, K. Smith, D. Maksimovic, Advanced cell-level control for extending electric vehicle battery pack lifetime, in: Energy Conversion Congress and Exposition (ECCE), 2016 IEEE, IEEE, 2016, pp. 1–8.

[70] F. Altaf, L. Johannesson, B. Egardt, Evaluating the potential for cell balancing using a cascaded multi-level converter using convex optimization, IFAC Proceedings Volumes 45 (30) (2012) 100–107.

[71] F. Altaf, B. Egardt, Comparative analysis of unipolar and bipolar control of modular battery for thermal and state-of-charge balancing, IEEE Transactions on Vehicular Technology 66 (4) (2017) 2927–2941.